Space for Shore

ESA EOEP-5

Coastal Erosion

Deliverable

Product Validation Report

DOCUMENT HISTORY			
VERSION	AUTHORS	DATE	NOTE
0.0	MANON BESSET, I-SEA	08/25/2020	FIRST DRAFT
1.0	MANON BESSET, I-SEA, SILVÈRE LAMY, I-SEA, SANDRA FERNANDEZ, UNIV. OF AVEIRO, KONSTANTINA BANTOUVAKI, UNIV. OF HAROKOPIO, GEORGIANA ANGHELIN, TERRA SIGNA, SORIN CONSTANTIN, TERRA SIGNA, KERSTIN STELZER, BROCKMANN CONSULT, AHMED BELAIDI, HARRIS, IMANOL ECHAVE, HARRIS, EVANGELOS FRYGANIOTIS, TERRASPATIUM, GEORGIA KALOUSI, TERRASPATIUM, PROSPER EVADZI, BROCKMANN CONSULT	04/12/2020	FIRST RELEASE
2.0			SECOND RELEASE
3.0			THIRD RELEASE INCLUDING CLARIFICATIONS ASKED BY ESA

Summary

1 Introduction 8

1.1 Scope of the document 8

2 Validation of indicator 'waterline' 9

2.1 Algorithm 2AI – Waterline detection using band ratios 9

2.1.1 Data and study areas 9

2.1.2 Method of validation 11

2.1.3 Results 11

2.1.4 Discussion 23

2.2 Algorithm 2AII – Waterline detection using NDWI 25

2.2.1 Data and study areas 26

2.2.2 Method of validation 26

2.2.3 Results 26

2.2.4 Discussion 27

2.3 Algorithm 2AIII – Waterline detection using AWEI 28

2.3.1 Data and study areas 28

2.3.2 Method of validation 28

2.3.3 Results 28

2.3.4 Discussion 29

2.4 Algorithm 2AIV – Waterline detection using NDWI2 30

2.4.1 Data and study areas 30

2.4.2 Method of validation 33

2.4.3 Results and Discussion 33

2.5 Algorithm 2G – Waterline detection using binary products from SAR amplitude data (Phase 1) 33

2.5.1 Data and study areas 33

2.5.2 Method of validation 35

2.5.3 Results 36

2.5.4 Discussion 37

3 Validation of indicator 'Upper swash limit' 37

3.1 Algorithm 2A2F – Upper swash limit using combined NDWI-derived waterlines 37

3.1.1 Data and study areas 37

3.1.2 Discussion 38

3.1.3 Method & Data of validation 38

3.1.4 Results 38

4 Validation of indicator 'dune foot' 39

4.1 Algorithm 3H – Dune foot extraction using supervised classification 39

4.1.1 Data and study areas 39

4.1.2 Method of validation 40

4.1.3 Results 41

4.1.4 Discussion 42

5 Validation of indicator 'cliff lines' 43

5.1 Algorithm 3I – Cliff extraction using supervised classification 43

5.1.1 Data and study areas 43

5.1.2 Method of validation 46

5.1.3 Results 47

5.1.4 Discussion 50

5.2 Algorithm 3c – Cliff extraction using the cross-shore variation of the beach/cliff slope 51

5.2.1 Data and study areas 51

5.2.2 Method of validation 52

5.2.3 Results 52

5.2.4 Discussion 54

6 Validation of indicator 'top of the cliff movement' 54

6.1 Algorithm 3J – Top of the cliff movement monitoring using PS 54

6.1.1 Data and study areas 55

6.1.2 Method of validation 55

6.1.3 Results 55

6.1.4 Discussion 58

7 Validation of indicator 'Bathymetry' 59

7.1 Algorithm 4B – Quasi-analytical model to retrieve bathymetry from HR/VHR optical data 59

7.1.1 Data and study areas 59

7.1.2 Method and results of validation 63

7.1.3 Discussion 65

7.2 Algorithm 4C – Bathymetry swell inversion 65

7.2.1 Data and study areas 66

7.2.2 Method of validation 66

7.2.3 Results....67

7.2.4 Discussion....68

8 Validation of indicator 'Submerged sandbar position'....68

8.1 Algorithm 6A – Submerged sand banks....68

8.1.1 Data and study areas....68

8.1.2 Method of validation....70

8.1.3 Results....70

8.1.4 Discussion....71

8.2 Algorithm 6B – Mapping change of submerged sandbars/sand ridges....71

8.2.1 Data and study areas....72

8.2.2 Method of validation....72

8.2.3 Results....73

8.2.4 Discussion....80

9 Validation of indicator 'creek edge'....83

9.1 Algorithm 2J – Decision tree classification based on band ratios and LSU....83

9.1.1 Data and study areas....83

9.1.2 Method of validation....83

9.1.3 Results....83

9.1.4 Discussion....85

Synthesis of the validation action....87

Changes in algorithm nomenclature since the Validation plan....89

References....90

1 INTRODUCTION

1.1 Scope of the document

This document provides an exhaustive synthesis of the product validation results of current indicators produced by the Space for Shore Consortium as well as the associated methodologies for validation of indicators or algorithms. These results disclose the necessity of future work (*e.g.,* field surveys at some POC sites, new techniques of field data acquisition).

The algorithms are detailed in the dedicated Technical Specifications deliverable, provided, and described for the different coastal indicators. The document provides illustrations and overall quantifications of validation results for each algorithm of each indicator validated. Details of individual products are provided in the Annex. The different sites analyzed are explicitly distinguished, and the validation data are indicated.

An interpretation of the validation results is provided, with a critical conclusion for each algorithm, depending on the morphological indicators, the methods, and the satellite data used, but also the limitations of the validation data itself.

2 VALIDATION OF INDICATOR 'WATERLINE'

Waterline is identified as the border between sea and land interface extracted from SAR (radar) and optical satellite imagery.

2.1 Algorithm 2AI – Waterline detection using band ratios

Algorithm 2ai is an algorithm based on supervised classification that differentiates water pixels from other pixels located in the sub aerial domain. First, representative polygons for the two typologies were digitalized to build the reference database. Then, the Maximum Likelihood classifier algorithm was applied on the spectral bands. The final step consists in extracting the interface between the two typologies from the raster-formatted classification output. This algorithm was tested during the first phase of the project for Sulina - Sfantu Gheorghe site and the validation results will be presented in this report.

For Baltic and North Seas' sites (Germany), the waterline is detected by thresholding a band ratio composed of the NIR and blue bands. The raster data 1 and 0 is converted to a vector shapefile.

2.1.1 Data and study areas

The waterline indicator was extracted along the Sulina – Sfantu Gheorghe coastline (Romania) from 4 Sentinel-2 images, one Landsat 8 scene, three Pleaides 1B image and one SPOT 7 product.

Satellite Name	Product Date	Validated in 2019	Validated in 2020	Not validated	Validated 2x
Landsat 8	2016/09/24		X		
SPOT 7	2015/09/18			X	
Pléiades	2015/08/03		X		
	2015/07/22			X	
	2013/08/05			X	
Sentinel-2	2015/08/02		X		
	2016/02/18		X		
	2016/04/28	X			
	2016/09/05		X		

The waterline indicator was retrieved along the German coast of Baltic and the North Seas from Landsat-7, Landsat-8, and Sentinel-2 data. Four study areas have been selected for retrieving coastline/waterline products: Sylt Odde (North Sea), Kiel Probstei (Baltic Sea), Heiligenhafen

(Baltic Sea) and Fehmarn (Baltic Sea). The following products are processed and validated according to specification.

Area	Satellite name	Product date	Validated in 2019	Validated in 2020	Not validated	Validated 2x
Baltic Sea: Fehmarn and Heiligenhafen	Sentinel 2	08/09/2015		X		
Baltic Sea: Fehmarn and Heiligenhafen		04/06/2016		X		
Baltic Sea: Fehmarn and Heiligenhafen		19/06/2017		X		
Baltic Sea: Fehmarn and Heiligenhafen		06/06/2018			X[1]	
Baltic Sea: Fehmarn and Heiligenhafen		29/06/2019			X[1]	
Baltic Sea: Fehmarn and Heiligenhafen		15/06/2020			X[1]	
Baltic Sea: Kiel Probstei	Landsat-7	15/08/2001			X[1]	
Baltic Sea: Kiel Probstei		06/06/2002			X[1]	
Baltic Sea: Kiel Probstei	Landsat-8	23/07/2013		X		
Baltic Sea: Kiel Probstei	Landsat-8	19/08/2014	X			
Baltic Sea: Kiel Probstei	sentinel-2	22/08/2015	X	X		X
Baltic Sea: Kiel Probstei		05/05/2016		X		
Baltic Sea: Kiel Probstei		02/06/2017			X[1]	
Baltic Sea: Kiel Probstei		20/05/2018			X[1]	
Baltic Sea: Kiel Probstei		24/07/2019			X[1]	
Baltic Sea: Kiel Probstei		23/06/2020			X[1]	
North Sea: Sylt Odde	Landsat-7	05/07/2001			X[1]	
North Sea: Sylt Odde		31/07/2002			X[1]	
North Sea: Sylt Odde	Landsat-8	15/08/2013	X			
North Sea: Sylt Odde		15/06/2014	X			
North Sea: Sylt Odde	Sentinel-2	22/08/2015	X			
North Sea: Sylt Odde		15/09/2016	X			

[1] *relative comparison, but no in-situ data*

North Sea: Sylt Odde		02/06/2017	X			
North Sea: Sylt Odde		27/07/2018	X			
North Sea: Sylt Odde		17/06/2019	X			
North Sea: Sylt Odde		16/06/2020			X[1]	

[1] relative comparison, but no in-situ data

2.1.2 Method of validation

In order to assess the accuracy of the algorithm, the derived shorelines extracted in Romania have been compared with in-situ measurements collected using a GPS. Cross-shore transects were generated every 25 m. For each product, the distance between the baseline and each of the waterline versions was computed. After that, the difference between reference waterline and the automatic satellite estimated waterline was determined.

To evaluate the waterline extracted from satellite images along the Baltic and the North Seas regions (Germany), the coastline position is validated in three ways. The first one is the visual inspection of an overlay of the coastline on airborne images of the same year and on laser scan data if available. A second method compares the different coastlines to each other, where no coastal change is expected (e.g. along dykes). It is expected that the extracted coastlines are remarkably similar in those areas. The third method is the calculation of the distance of the satellite derived line from the digitized line from airborne images. The latter has been provided by the coastal protection agency (LKN) and is the official coastline used for their analyses. In-situ data used within the validation are provided by LKN Schleswig-Holstein. They consist of coastline derived from airborne digital orthophotos (DOP) and airborne laser scan data. Some sections are also mapped in-situ. For Sylt area, the coastline is compared with DOP images.

2.1.3 Results

For algorithm 2ai, based on supervised classification, the global results for Romanian areas show a mean error of 8.28 m for the products derived from Sentinel-2 data, 11.57 m for those extracted from Landsat 8 images and 4.96 m for the product derived from one Pleiades product.

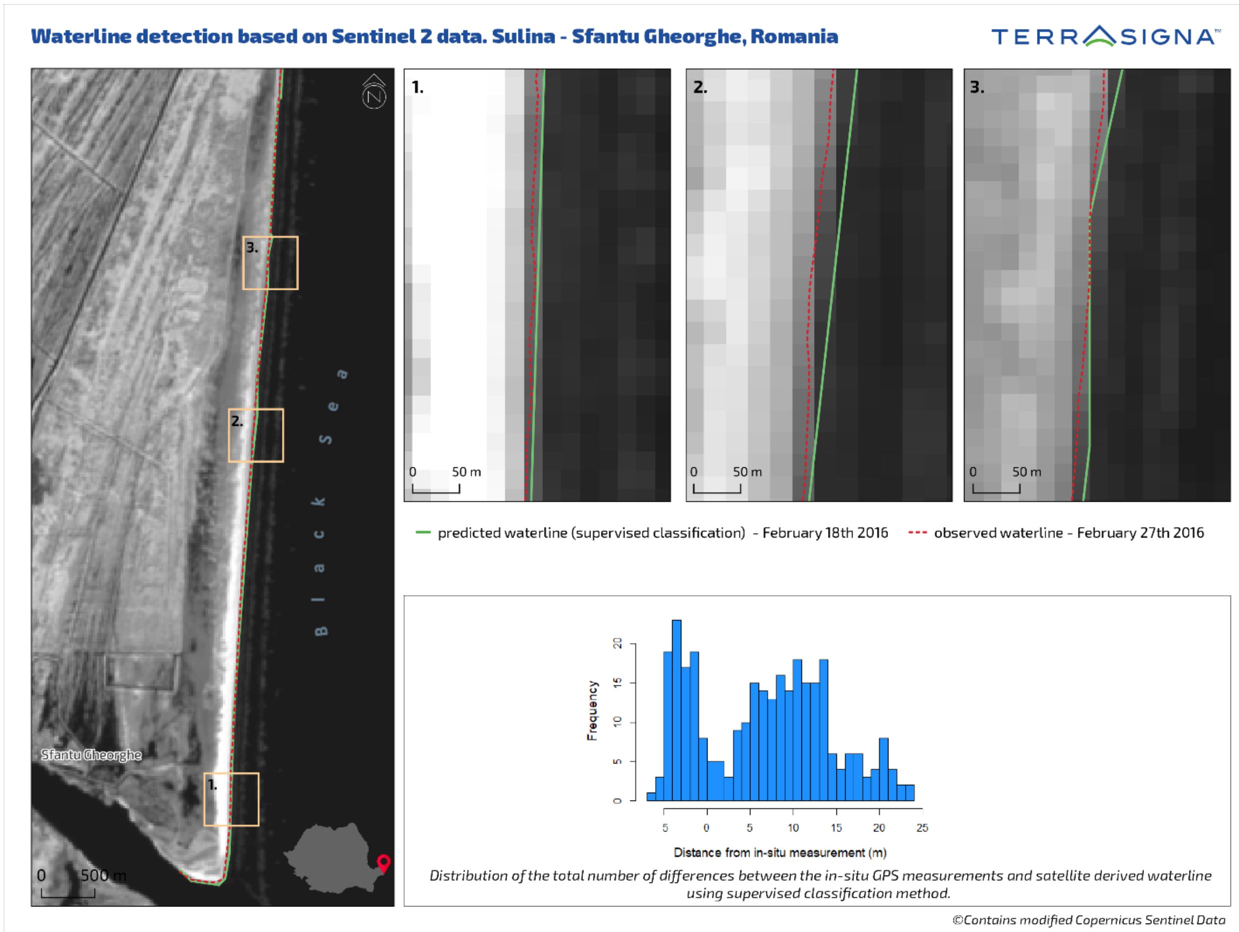

Fig. 1 : Comparison between predicted (supervised classification) and observed waterline for Sulina – Sfantu Gheorghe area.

The validation in Baltic and North Seas has been quantitatively and qualitatively carried out.

- **Visual inspected based on airborne and laser scan images**

The overlays for the visual inspection are shown in Fig. 2 & Fig. 3 maps for Sylt Odde for two different years. The examples are given for 2014 and 2018/2019. Changes in the shape of Sylt Odde are clearly visible. In the example of 2018/2019 shows the changes between both Sentinel-2 acquisitions. The airborne image was acquired in between and shows fits in some parts to the coastline of 2018, in others to 2019. Underpinning the fast changes in the area.

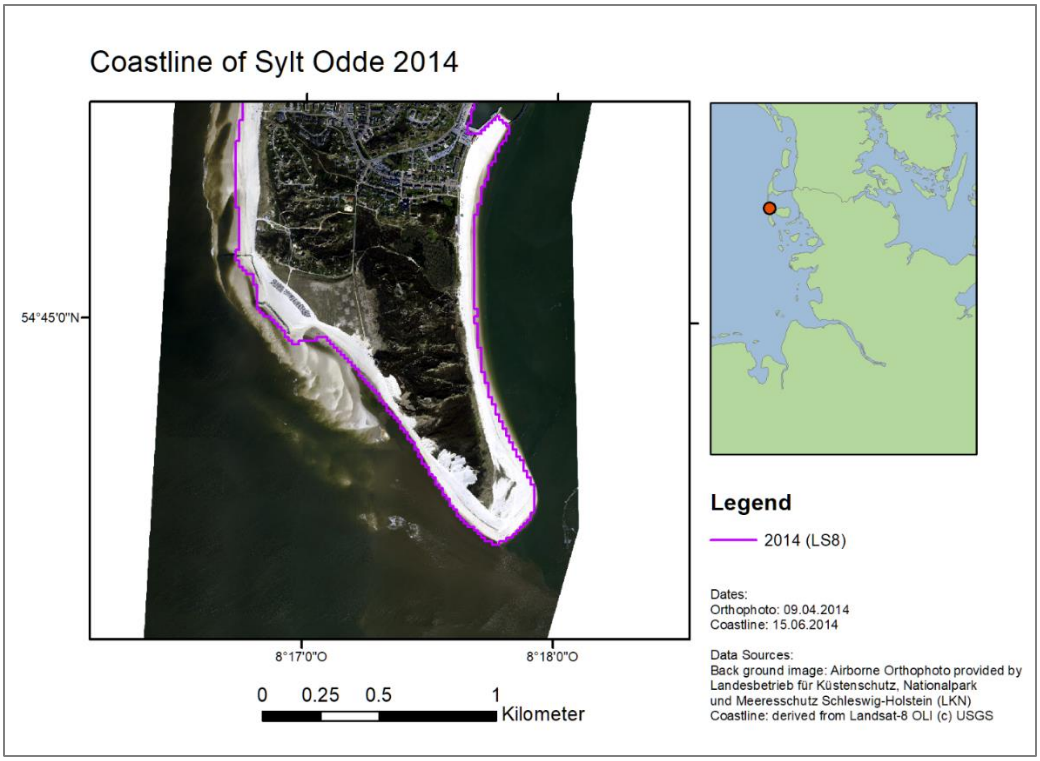

Fig. 2: Map showing the airborne image of Sylt Odde from 09.04.2014 and the waterline derived from Landsat-8 acquired on 06/15/2014.

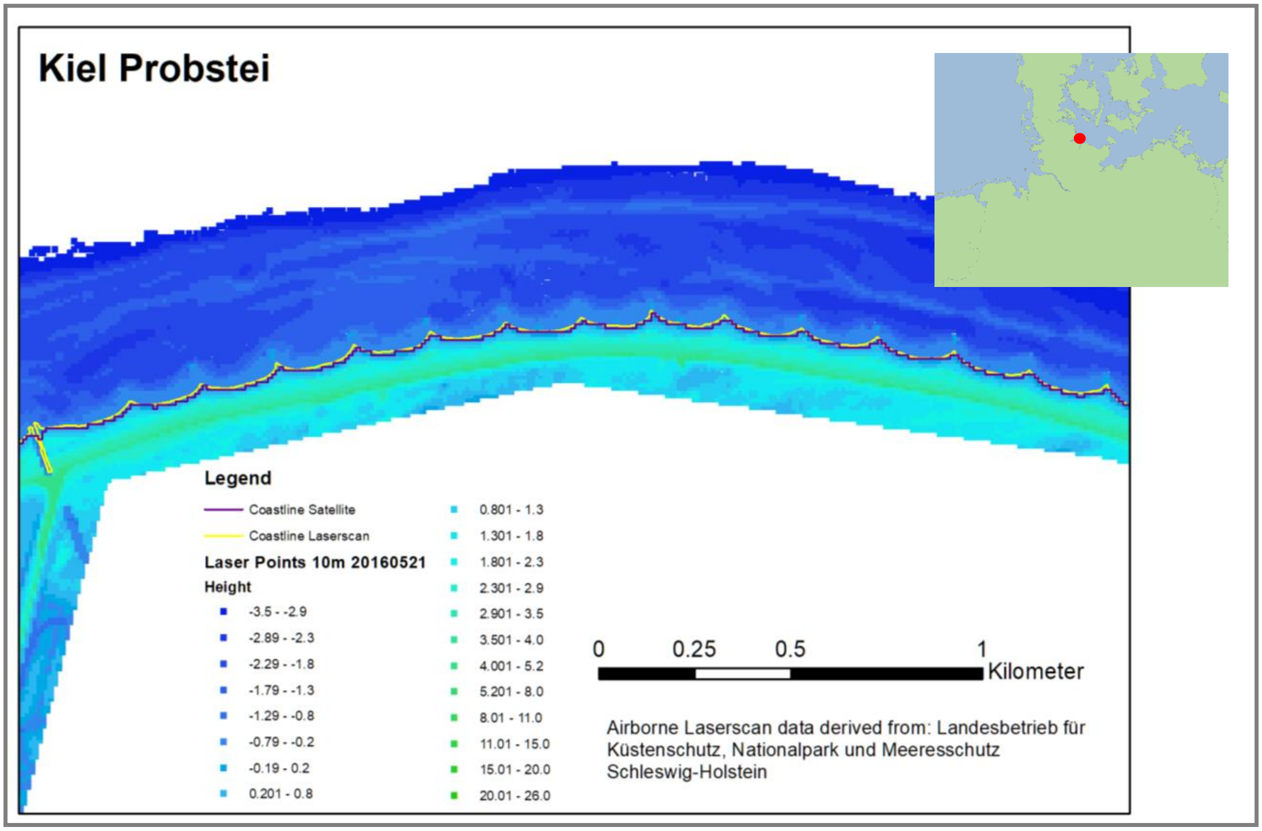

Fig. 3: Subset of Kiel Probstei area showing laser scan data (depths and heights in color) and derived coastline (yellow line) compared to satellite derived coastline (black line) for 2016.

- **Comparison of stable coastlines**

Another relative approach for validating the coastline extractions from satellites is the relative comparison at coastal subsets that do not change due to coastal protection or stable situations. Fig. 4 and Fig. 5 show two examples along the coast of Fehmarn. The first image shows different coastlines derived from airborne images or laser scan data provided by LKN, while the second image shows the different extraction from satellite images. The latter shows different colours for coastlines derived from Landsat (pinkish) and from Sentinel (greenish). It is clearly seen that the spatial resolution of images is influencing the accuracy, but also the inaccuracy in geolocation of Landsat images is an issue. A shift is clearly seen in Fig. 4, while Fig. 5 is not affected by a shift, but it remains the loss of information due to spatial resolution by Landsat type of products.

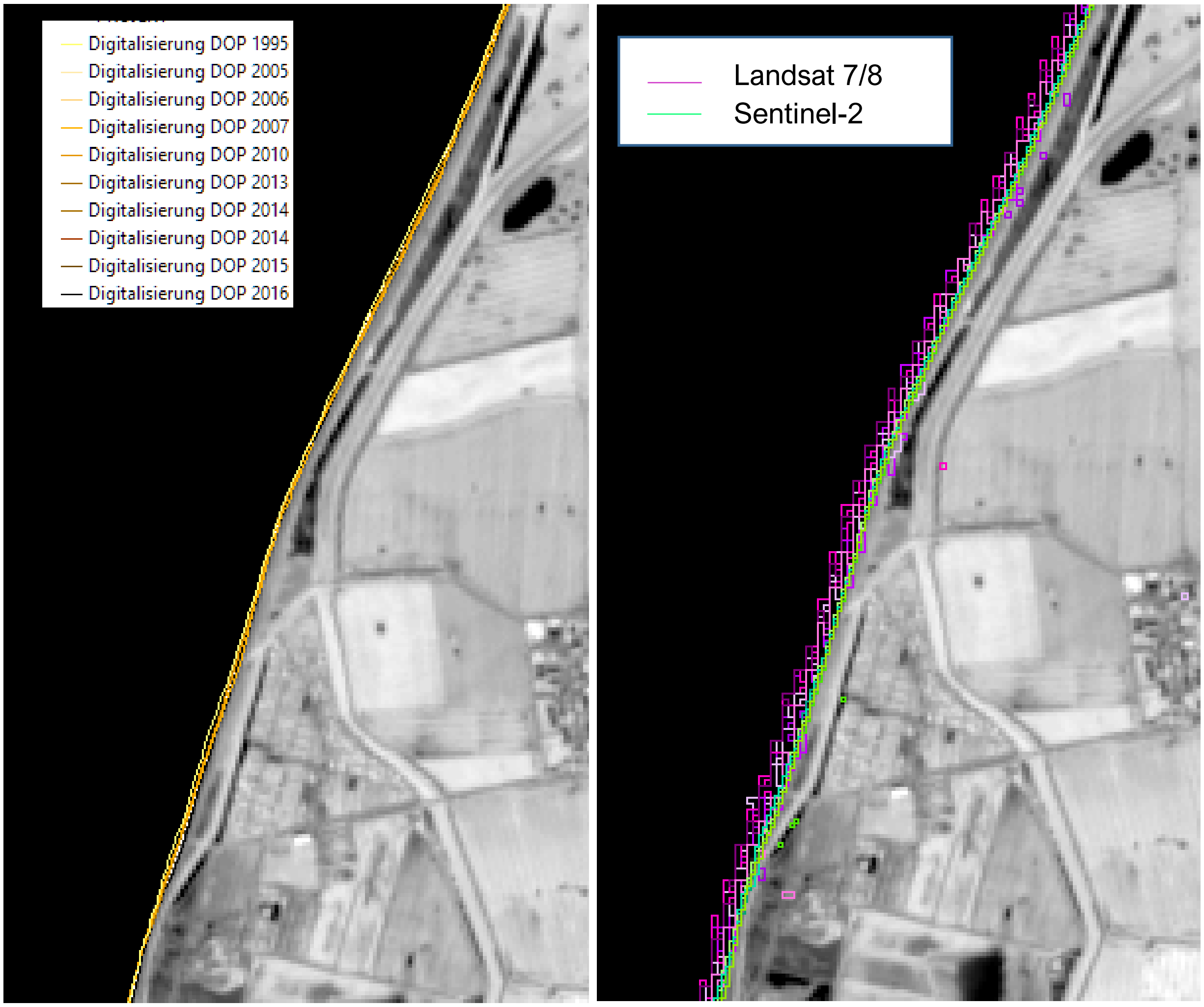

Fig. 4: Coastlines derived from DOP and laser scan (left) and from Satellite (right), Westcoast of Fehmarn.

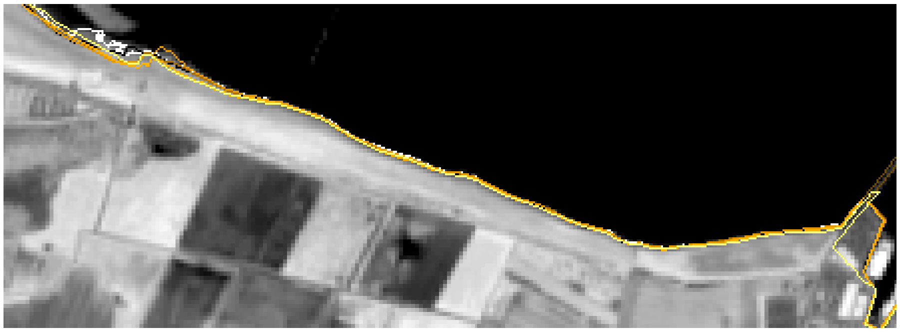

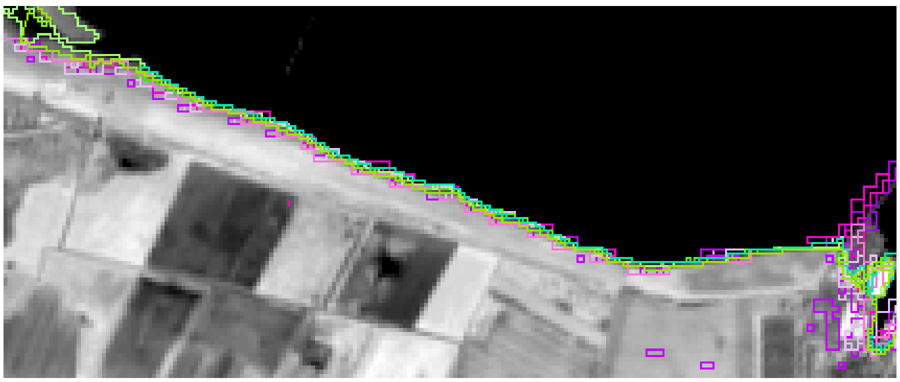

Fig. 5: Coastlines derived from DOP and laser scan (above) and from Satellite (below), Northeast coast of Fehmarn.

- **Distance between satellite-based coastlines and coastlines derived from DOPs**

A data set of lines derived from digital orthophotos, laser scan data and measurements were provided by LKN. The data set holds information up to 2016. This data set was used to compare the data for single years. The most recent years were compared, which are 2015 and 2016. The procedure applied translated the satellite coastline into points with distance of 5m and calculating the distance to the respective coastline derived from DOP. The points are then coloured according to their distance (third image in Fig. 6). As a next step, histograms are derived showing the distribution of distances for the respective coastal regions. This has been performed for data from 2015 and 2016 for Kiel Probstei, Fehmarn, Fehmarn Krummsteert and Heiligenhafen Graswarder

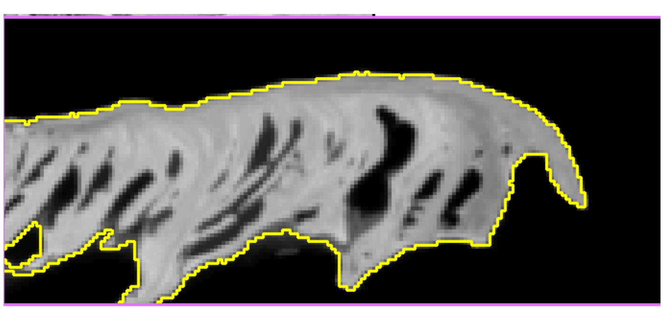

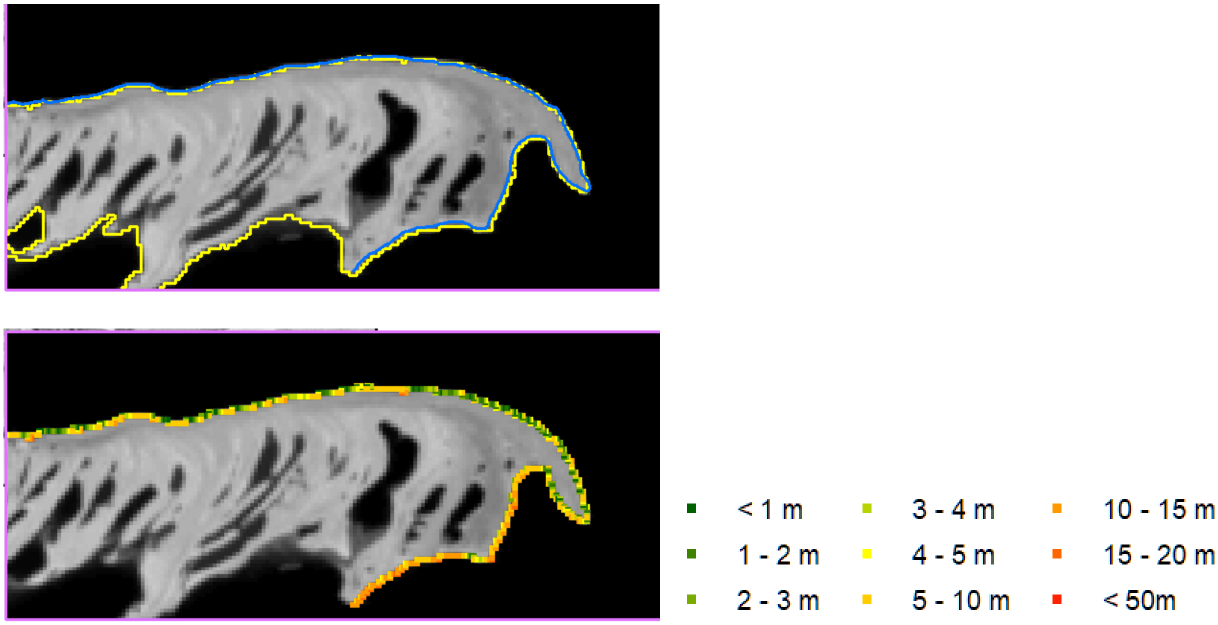

Fig. 6: Heiligenhafen Graswarder. Sentinel-2 with derived coastline (above), overlayed with shoreline from Digital Orthophotos (middle) and finally the distances between both lines expressed in colors (below).

The results for the calculation of the distance between coastline satellite and in-situ/airborne derived coastline is given in the following map and following histogram plots. The distance is available in concrete steps in meters.

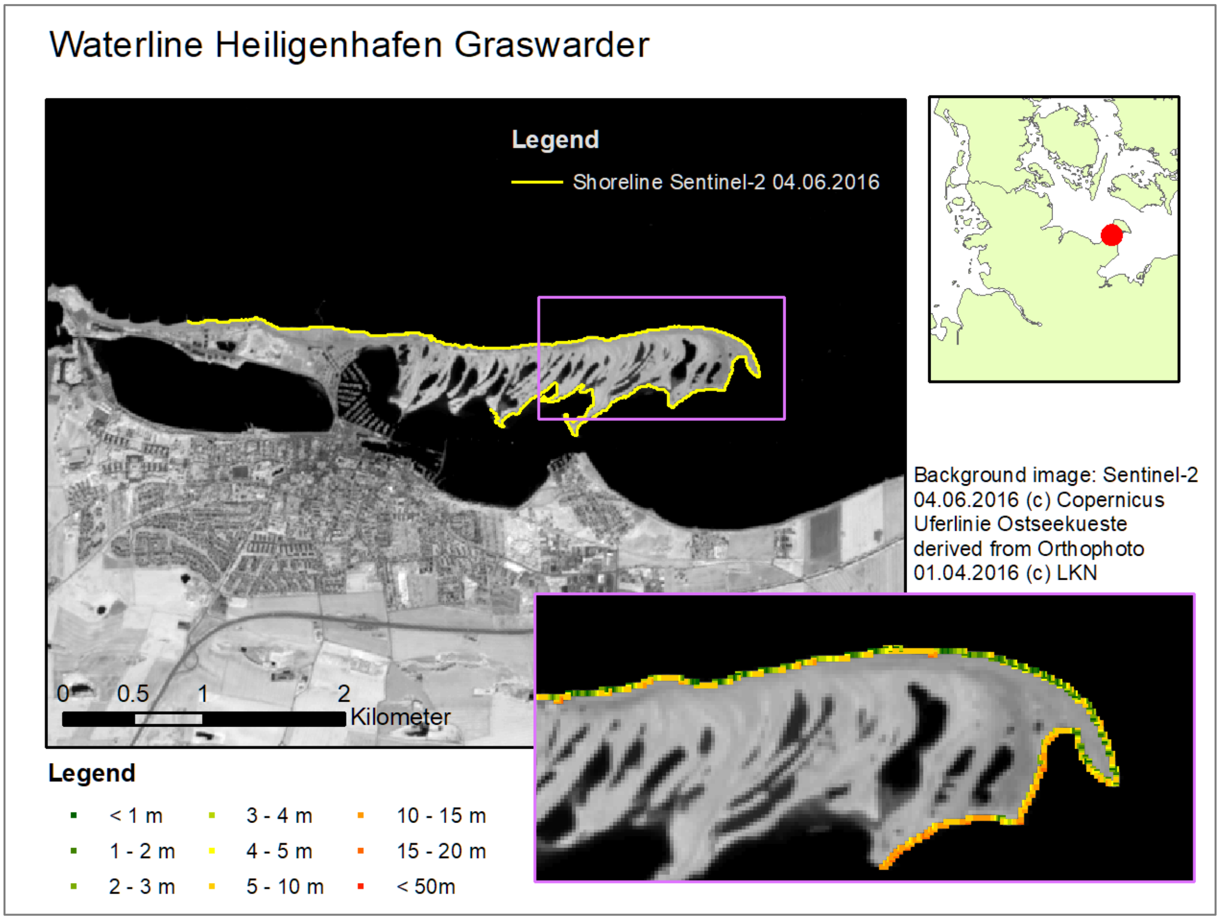

Fig. 7: Distance between Sentinel-2 derived coastline and coastline derived from orthophoto (2016).

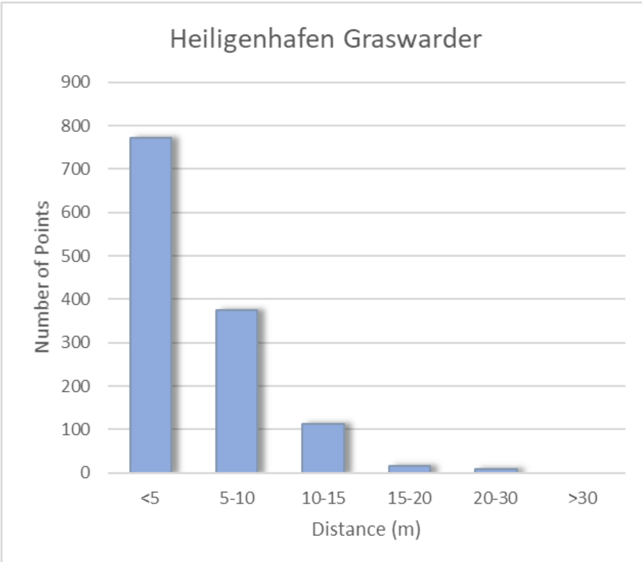

Fig. 8: Distribution of distances in m between coastlines derived from satellite and from airborne ortho photo (2016).

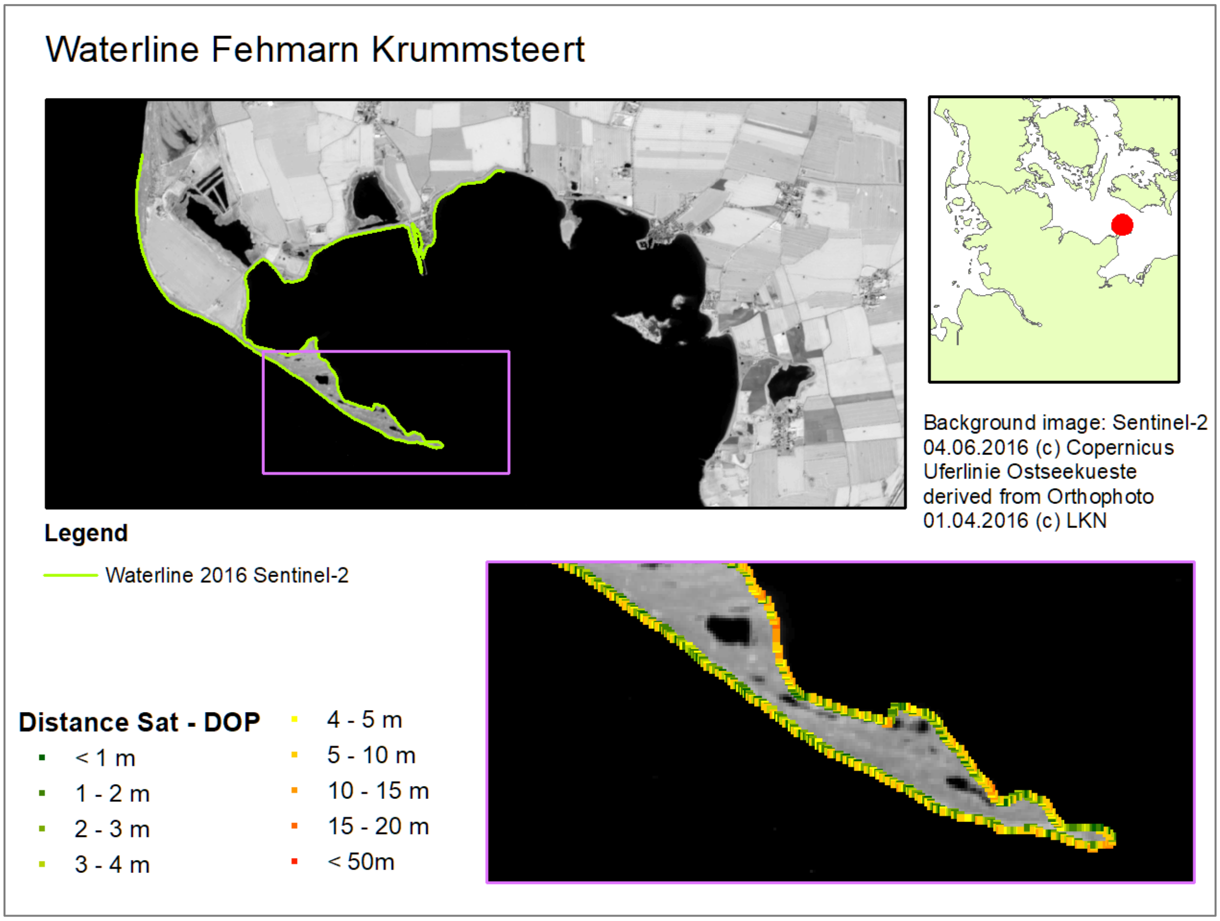

Fig. 9: Distance between Sentinel-2 derived coastline and coastline derived from orthophoto (2016) for parts of Fehmarn coast (Krummsteert).

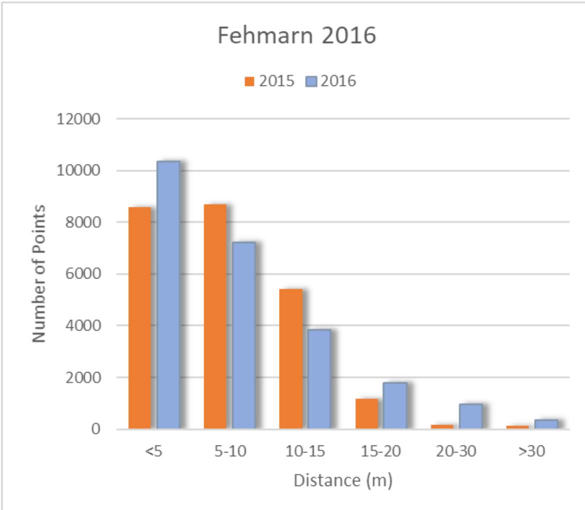

Distance (m)	2015 %	2016 %
<5	35.5	42.3
5-10	36.0	29.5
10-15	22.4	15.6
15-20	4.9	7.3
20-30	0.6	3.9
>30	0.5	1.4

Fig. 10: Baltic Sea region Fehmarn: distribution of distances (in m) between satellite derived coastline and coastline gained from digital orthophotos for the complete Fehmarn cost in 2015 and 2016.

Having a closer look to an area which shows changes in the coastline, we receive a good result of 65% of all points are below 5m difference and 94% of all points are below 10m, which is the resolution of the Sensor.

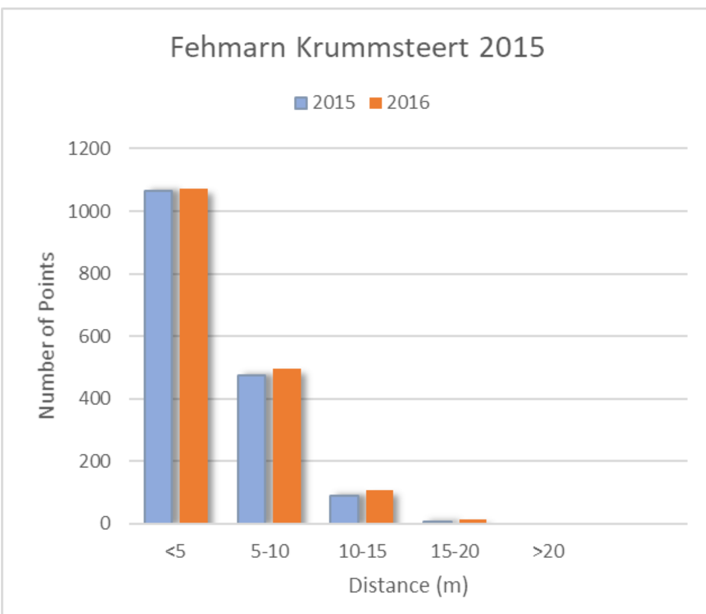

Distance (m)	2015 %	2016 %
<5	65.1	63.5
5-10	29.0	29.4
10-15	5.4	6.3
15-20	0.5	0.7
20-30	0.0	0.0
>30	0.0	0.0

Fig. 11: Baltic Sea region Fehmarn Krummsteert: distribution of distances (in m) between coastlines derived from satellite and from airborne images for 2015 and 2016.

The above investigation only included Sentinel-2 derived coastlines which perform very similar. The final investigation also includes a Landsat-8 product for the Kiel Probstei region (Fig. 12). It clearly shows the differences in accuracy between Sentinel-2 and Landsat. In this case, it is caused by the two reasons mentioned above – a shift in data as (inaccurate geolocation) as well as the spatial resolution. This is demonstrated in Fig. 13 where blueish colors show Sentinel-2 derived coastlines and red/orange colors show Landsat derived coastlines).

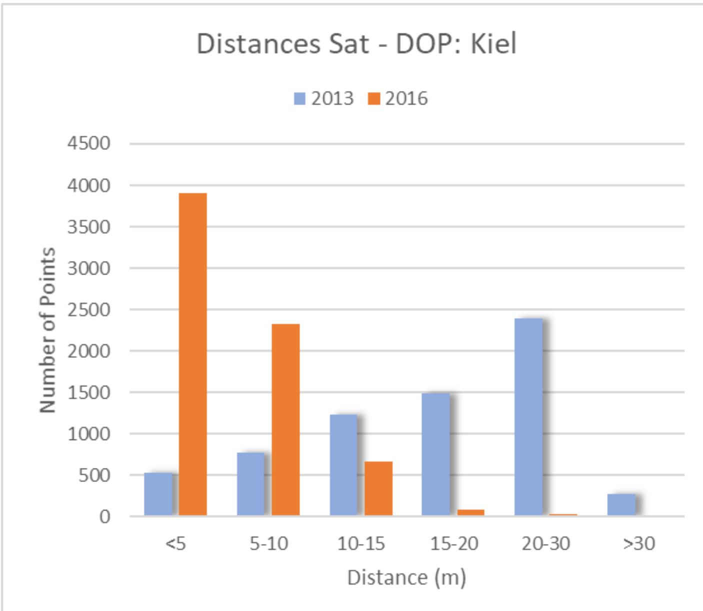

Distance (m)	2013 %	2016 %
<5	8.0	55.5
5-10	11.5	33.1
10-15	18.3	9.5
15-20	22.3	1.3
20-30	35.8	0.4
>30	4.1	0.2

Fig. 12: Baltic Sea region Kiel Probstei: distribution of distances (in m) between coastlines derived from satellite and from airborne images for 2013 (Landsat-8) and 2016 (Sentinel-2).

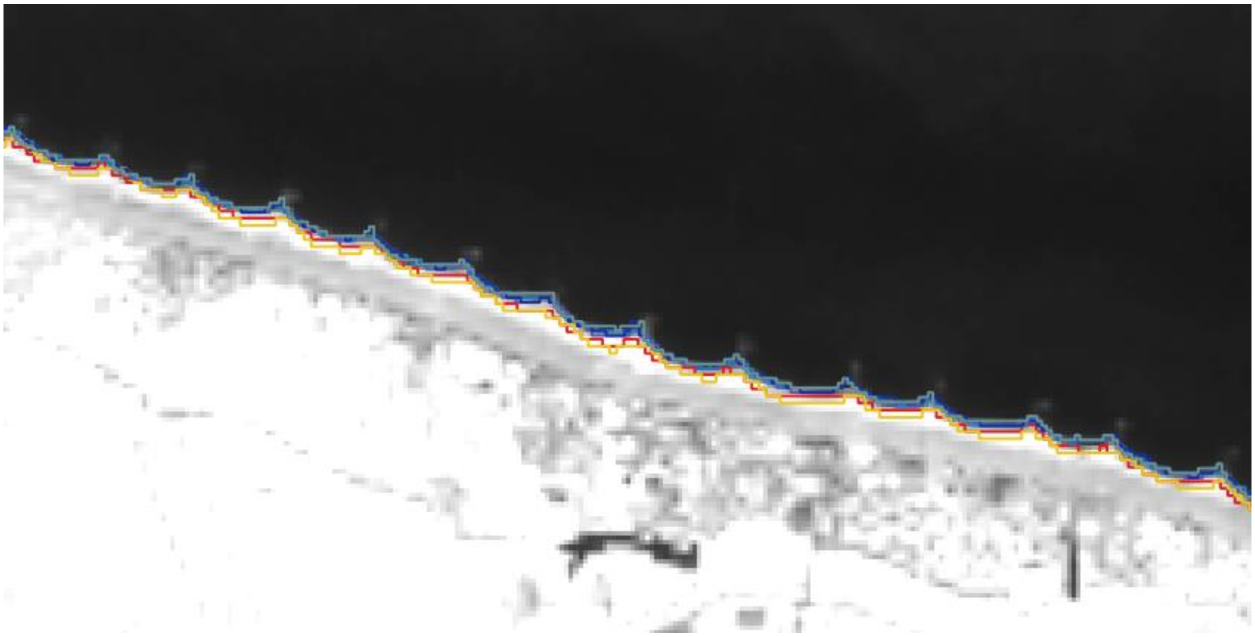

Fig. 13 : comparison of coastlines along the Kiel Probstei shoreline (blue: Sentinel-2, red orange: Landsat).

2.1.4 Discussion

The supervised classification method shows satisfactory accuracy for the products in Black Sea that were analyzed. Higher resolution images led to better results (waterlines extracted from Landsat images show lower precision). However, the supervised classification can be difficult to implement on long time series and can be computational more expensive than the index-based approach.

The results for Sentinel-2 coastlines are very promising and with mainly 5-10m difference to the official coastlines is within the limits of spatial resolution what is possible. The results for Landsat are less good and show drawbacks from coarser spatial resolution and from inaccuracies of geolocation. Each input product would need to be manually georeferenced, which was not possible for the large number of products. The quality is influenced by quality of the input product: clouds along the coastline or very turbid water is causing misinterpretation of the coastline. A quality control of each coastline retrieval is necessary.

Based on the single coastline extraction for multiple years, the changes in coastline position is generated. The results for Sylt Odde and Keil Probstei are shown in Fig. 14 and Fig. 15. While Sylt Odde shows clear changes in the images and derived coastlines, the coastline at Kiel Odde is changing in a much smaller scale. The patterns along the coast follow the constructions for coastal protection (Buhnen) and the coast is much more stable than the coast for Sylt Odde.

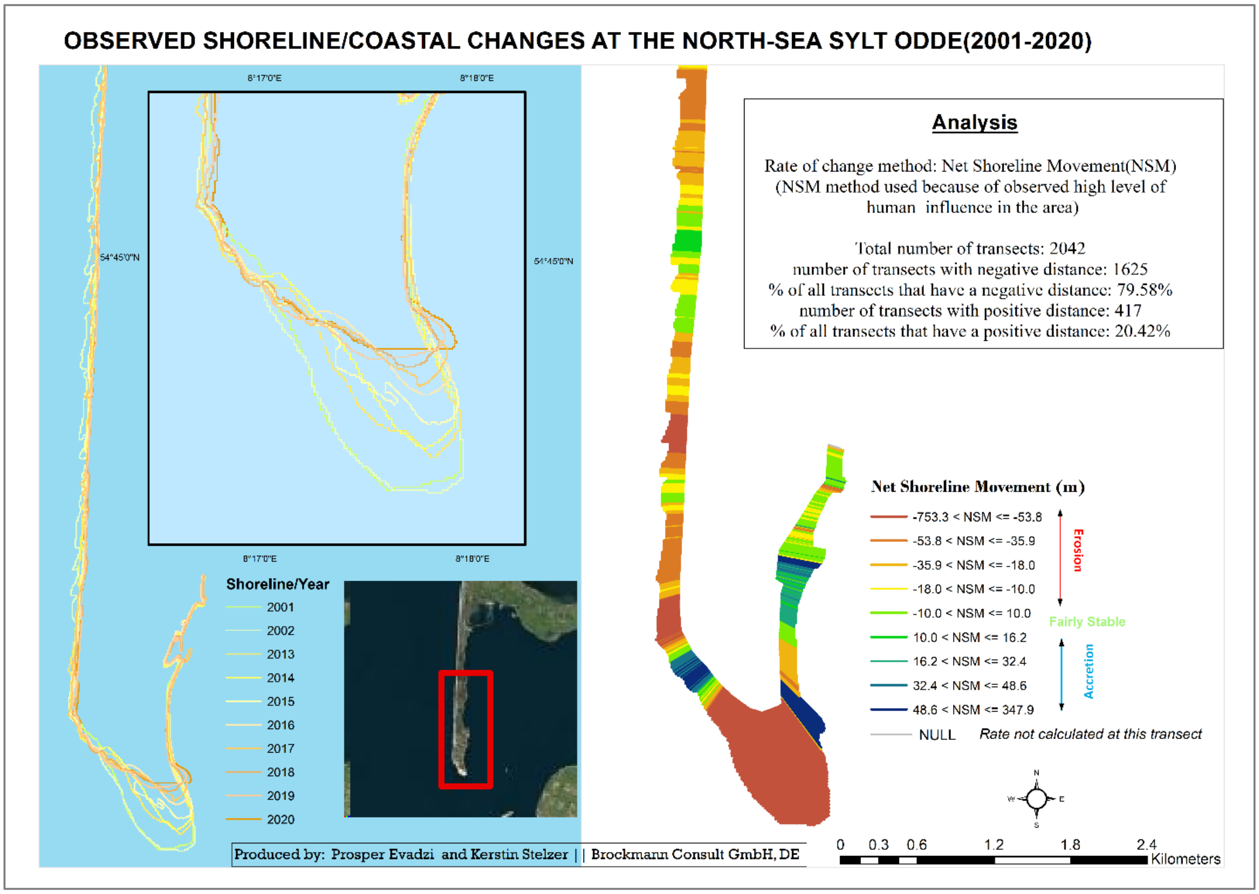

Fig. 14: Coastline changes at test site Sylt Odde between 2001 and 2020.

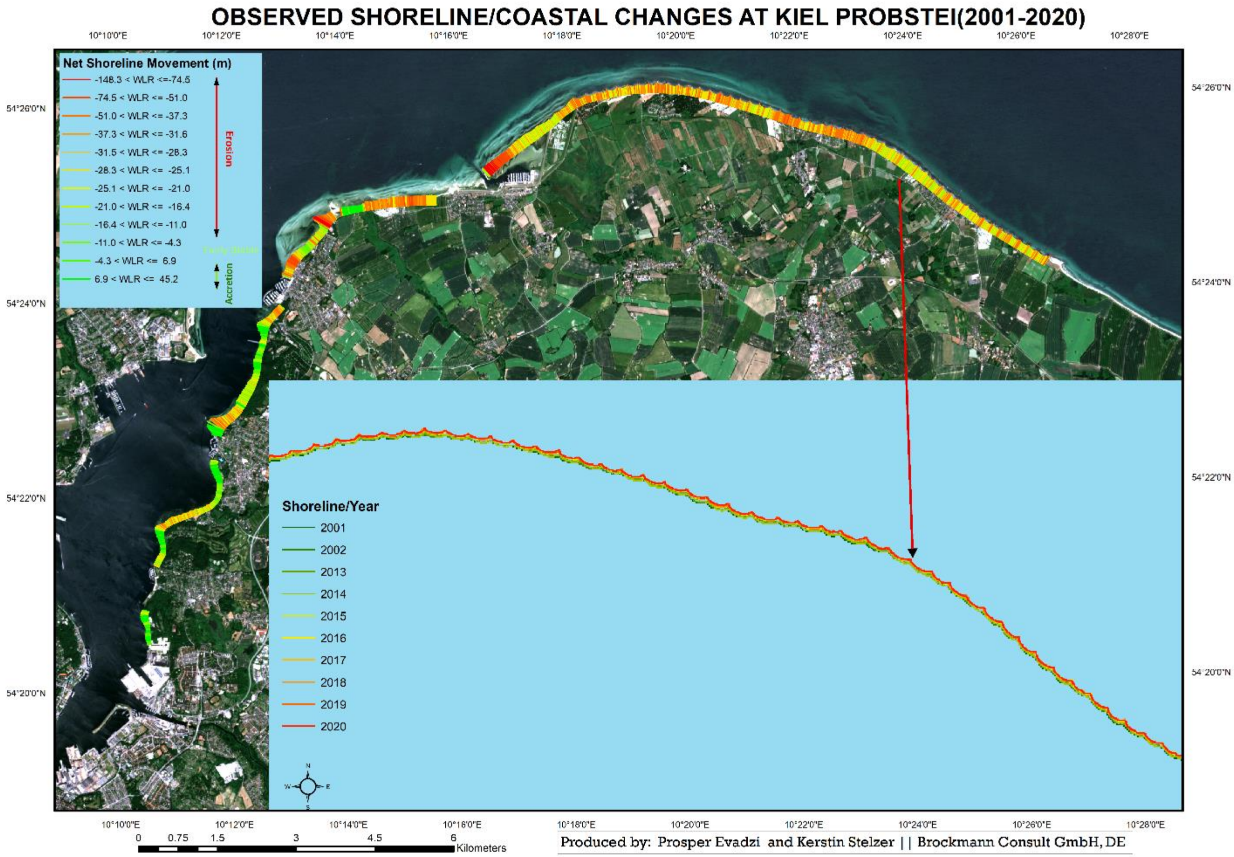

Fig. 15: Coastline changes at test site Kiel Probstei between 2001 and 2020.

2.2 Algorithm 2AII – Waterline detection using NDWI

During the first phase of the project, algorithm 2aii, based on Normalized Difference Water Index (NDWI) was used to derive the waterline indicator from Sentinel-2, Landsat, Pléiades, and SPOT-7 data. For the NDWI approach, a modified version of the index was computed, meaning that the SWIR band was used instead of the NIR one (only for Landsat 8 and Sentinel-2 data). This was chosen as the SWIR region of the electromagnetic spectrum is less prone to be affected by shallow or high turbidity waters. During the first phase of the project, an automated threshold detection algorithm was applied on the MNDWI, to compute the water - land limit.

During the second phase of the project an improved version of the method was tested. The Otsu thresholding method was applied the waterline was derived at sub-pixel level from Sentinel 2 and Landsat 8 Level 2 products at 10, respectively 30 m spatial resolution.

2.2.1 Data and study areas

The waterline indicator was extracted along the Sulina – Sfantu Gheorghe coastline from 4 Sentinel-2 images, 4 Landsat 8 scenes, three Pleaides 1B images and one SPOT 7 product.

Satellite Name	Product Date	Validated in 2019	Validated in 2020	Not validated	Validated 2x
Landsat 8	2016/09/24				X
	2013/08/06		X		
	2016/07/20		X		
	2016/06/10		X		
SPOT 7	2015/09/18			X	
Pléiades	2015/08/03		X		
	2015/07/22			X	
	2013/08/05			X	
Sentinel-2	2015/08/02				X
	2016/02/18				X
	2016/04/28				X
	2016/09/05				X

2.2.2 Method of validation

In order to assess the accuracy of the algorithm, the derived shorelines have been compared with in-situ measurements collected using a GPS and with waterline locations manually derived (digitized) using very high-resolution images (e.g. Pleiades). Cross-shore transects were generated every 25 m. For each product, the distance between the baseline and each of the waterline versions was computed. After that, the difference between reference waterline and the automatic satellite estimated waterline was determined.

During the second phase of the project the thresholding method was improved, and the waterline was derived from MNDWI and AWEI index, at sub-pixel level. The validation results were compared to establish which method (AWEI vs MNDWI, whole pixel vs sub-pixel, etc.) is the most accurate for Sulina – Sfantu Gheorghe area.

2.2.3 Results

The validation coverage varies between 8 km and 17 km along the Sulina – Sfantu Gheorghe coastline. The results for the products derived during the 1st phase of the project show a mean error of 28.68 m for the products derived from Sentinel-2 images, 34.65 m for the product derived from one Landsat 8 scene and almost 30 m for the one derived from one Pleiades image.

When it comes to the results obtained from MNDWI index during the 2nd phase of the project the improved automatic thresholding method together with the sub-pixel extraction of the waterline led to better results for 2aii algorithm. The global mean absolute error decreased to 11.1 m compared to 28.68 m for the products derived from Sentinel-2 images and to 7.65 m compared to 34.65 m for the products derived from Landsat products.

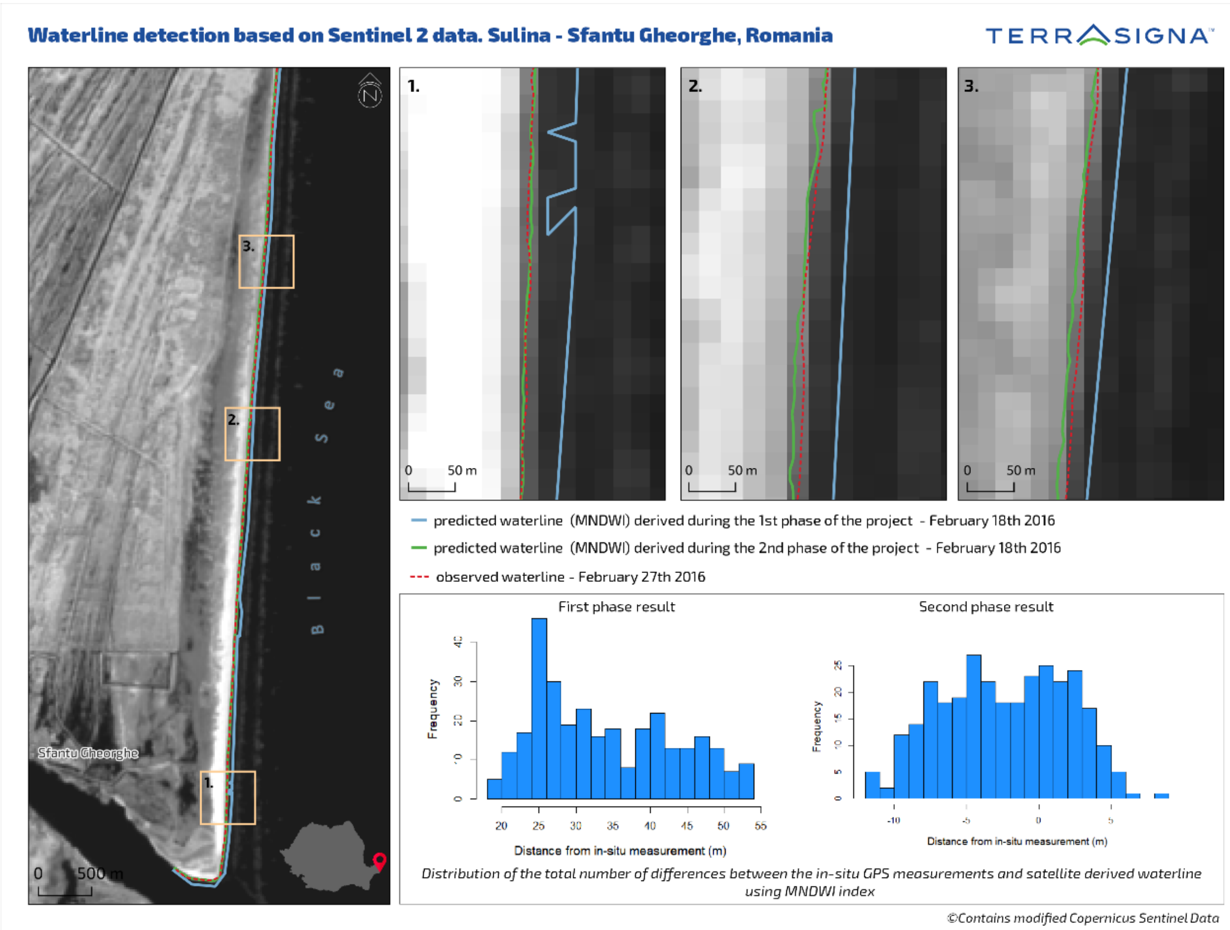

Fig. 16: Comparison between predicted (MNDWI) and observed waterline for Sulina – Sfantu Gheorghe area.

2.2.4 Discussion

According to the results presented above, during the 2nd phase of the project the improved automatic thresholding method together with the sub-pixel extraction of the waterline led to better results for the MNDWI method. The global mean absolute error decreased to 17.58 m from 29.74 m for the method mentioned above.

2.3 Algorithm 2AIII – Waterline detection using AWEI

The algorithm uses the Automated Water Extraction Index (AWEI) to detect the waterline indicator. After computing the index, the Otsu (Otsu, 1979) thresholding method was applied to separate the land from the water pixels. After that, the waterline indicator was derived at subpixel level and then, converted to vector line. The method was applied during the second phase of the project, to achieve better accuracy results.

2.3.1 Data and study areas

The improved method was tested on Sentinel 2 and Landsat 8, both Level 1 and Level 2 products, at 10 m and 30 m spatial resolutions for Sulina – Sfantu Gheorghe area. As observed (reference) waterline, GPS measurements and waterline positions derived from Pleiades images were used. The accuracy of the new method was tested on 4 Sentinel 2 – GPS measurements pairs, 1 Landsat 8 – GPS measurement pair, 3 Landsat 8 – Pleiades pairs.

Satellite Name	Product Date	Validated in 2019	Validated in 2020	Not validated	Validated 2x
Sentinel -2	20150802		X		
	20160218		X		
	20160428		X		
	20160905		X		
Landsat 8	20130805		X		
	20150720		X		
	20160924		X		
	20180610		X		

2.3.2 Method of validation

The derived shorelines have been compared with in-situ measurements collected using a GPS and with waterline locations manually derived (digitized) using very high-resolution images (e.g. Pléiades). Cross-shore transects were generated every 25 m. For each product, the distance between the baseline and each of the waterline versions was computed. After that, the difference between reference waterline (either in-situ measurements or derived from very high-resolution images) and the automatic satellite estimated waterline was determined.

2.3.3 Results

The global mean absolute error for the waterlines extracted from AWEI index at sub-pixel method using Otsu threshold was 7.54 m for the 4 products derived from Sentinel-2, respectively 4.77 m for the 4 products derived from Landsat 8 images. The validation coverage varies between 8 and 30 km according to the validation data available for Sulina – Sfantu Gheorghe site.

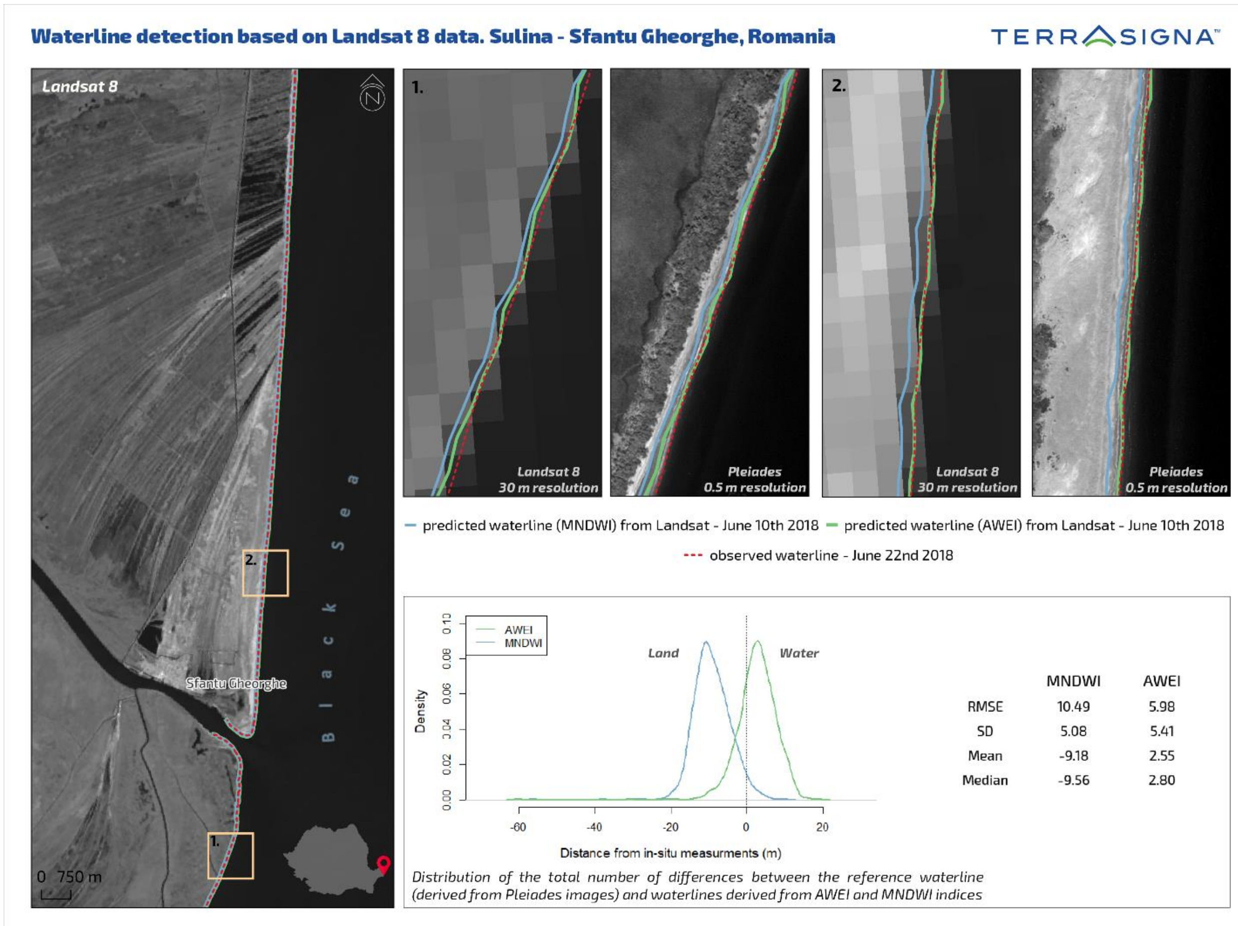

Fig. 17: Comparison between predicted (MNDWI and AWEI index) and observed waterline for Sulina – Sfantu Gheorghe area.

2.3.4 Discussion

All the validation results presented above showed that during the second phase of the project we managed to improve the methodology for the waterline indicator. During the 2nd phase of the project, according to the validation results that were presented above, the waterline indicator will be derived from long time series (Landsat 5, Landsat 8, Sentinel 2) at sub-pixel level using AWEI index and Otsu thresholding method for Sulina – Sfantu Gheorghe site.

2.4 Algorithm 2AIV – Waterline detection using NDWI2

The algorithm uses a supervised classification to calculate the NDWI2 index according to the method of Vos et al. (2019) to detect the waterline indicator. After computing the index, the Otsu (Otsu, 1979) thresholding method was applied to separate the land from the water pixels. After that, the waterline indicator was derived at subpixel level and then, converted to vector line (Marching square). The method was applied during the second phase of the project, to achieve better accuracy results.

2.4.1 Data and study areas

In France, the waterline was extracted from the same satellite images (Pléiades, Sentinel-2, and Landsat-8 satellite images) than those used for bathymetry production. The time series reaches 1995 for the oldest extracted waterlines (Rhône Delta), and ends in the year 2020 (included).

- Sud Region:
  - Saint-Raphaël (2015 – 2020)
  - Baie des Lecques (2015 – 2020)
  - Camargue (2013 – 2020)
  - Rhône river mouth (1995 - 2020)
  - Beauduc (2013 – 2019)
  - Juan les Pins (2015 – 2020)
- Nouvelle-Aquitaine Region:
  - Landes (08/2017 and 08/2018)

Area	Satellite name	Product date	Validated in 2019	Validated in 2020	Not validated	Validated 2x
Camargue	Landsat 8	2013/08/31		X[2]		
Camargue	Landsat 8	2014/09/03		X[2]		
Camargue	Landsat 8	2015/07/20		X[2]		
Camargue	Sentinel-2	2016/09/02		X[2]		
Camargue	Sentinel-2	2017/10/12		X[2]		
Camargue	Sentinel-2	2018/07/29		X[2]		
Camargue	Sentinel-2	2019/08/08		X[2]		
Camargue	Sentinel-2	2020/07/23		X[2]		
Beauduc	Landsat 8	2013/08/15		X[2]		
Beauduc	Landsat 8	2014/09/03		X[2]		
Beauduc	Landsat 8	2015/08/05		X[2]		
Beauduc	Sentinel-2	2016/05/05		X[2]		

Beauduc	Sentinel-2	2016/09/02		X[2]		
Beauduc	Sentinel-2	2017/04/10		X[2]		
Beauduc	Sentinel-2	2017/10/05		X[2]		
Beauduc	Sentinel-2	2018/04/20		X[2]		
Beauduc	Sentinel-2	2018/09/20		X[2]		
Beauduc	Sentinel-2	2019/03/31		X[2]		
Beauduc	Sentinel-2	2019/08/08		X[2]		
Beauduc	Sentinel-2	Apr./May 2020		X[2]		
Embouchure du Rhône	Landsat	Summer 1995		X[2]		
Embouchure du Rhône	Landsat	Summer 1996		X[2]		
Embouchure du Rhône	Landsat	Summer 1997		X[2]		
Embouchure du Rhône	Landsat	Summer 1998		X[2]		
Embouchure du Rhône	Landsat	Summer 1999		X[2]		
Embouchure du Rhône	Landsat	Summer 2000		X[2]		
Embouchure du Rhône	Landsat	Summer 2001		X[2]		
Embouchure du Rhône	Landsat	Summer 2002		X[2]		
Embouchure du Rhône	Landsat	Summer 2003		X[2]		
Embouchure du Rhône	Landsat	Summer 2004		X[2]		
Embouchure du Rhône	Landsat	Summer 2005		X[2]		
Embouchure du Rhône	Landsat	Summer 2006		X[2]		
Embouchure du Rhône	Landsat	Summer 2007		X[2]		
Embouchure du Rhône	Landsat	Summer 2008		X[2]		
Embouchure du Rhône	Landsat	Summer 2009		X[2]		
Embouchure du Rhône	Landsat	Summer 2010		X[2]		
Embouchure du Rhône	Landsat	Summer 2011		X[2]		
Embouchure du Rhône	Landsat	Summer 2012		X[2]		
Embouchure du Rhône	Landsat	Summer 2013		X[2]		
Embouchure du Rhône	Landsat	Summer 2014		X[2]		
Embouchure du Rhône	Landsat	Summer 2015		X[2]		
Embouchure du Rhône	Landsat	Summer 2016		X[2]		
Embouchure du Rhône	Landsat	Summer 2017		X[2]		
Embouchure du Rhône	Landsat	Summer 2018		X[2]		
Embouchure du Rhône	Landsat	Summer 2019		X[2]		
Embouchure du Rhône	Landsat	Summer 2020		X[2]		
Golfe de Fréjus	Pléiades	2017/07/06		X[2]		
Golfe de Fréjus	Sentinel-2	2015/11/17		X[2]		
Golfe de Fréjus	Sentinel-2	2016/04/22		X[2]		
Golfe de Fréjus	Sentinel-2	2016/10/02		X[2]		
Golfe de Fréjus	Sentinel-2	2017/04/07		X[2]		
Golfe de Fréjus	Sentinel-2	2017/10/12		X[2]		

Golfe de Fréjus	Sentinel-2	2018/04/22		X[2]		
Golfe de Fréjus	Sentinel-2	2018/09/29		X[2]		
Golfe de Fréjus	Sentinel-2	2019/03/23		X[2]		
Golfe de Fréjus	Sentinel-2	2019/09/29		X[2]		
Golfe de Fréjus	Sentinel-2	2020/04/09		X[2]		
Golfe de Fréjus	Pléiades	2020/09/04		X[2]		
Juan-les-Pins	Sentinel-2	Oct./Nov. 2015		X[2]		
Juan-les-Pins	Sentinel-2	Apr./May 2016		X[2]		
Juan-les-Pins	Sentinel-2	Oct./Nov. 2016		X[2]		
Juan-les-Pins	Sentinel-2	Apr./May 2017		X[2]		
Juan-les-Pins	Sentinel-2	Oct./Nov. 2017		X[2]		
Juan-les-Pins	Sentinel-2	Apr./May 2018		X[2]		
Juan-les-Pins	Sentinel-2	Oct./Nov. 2018		X[2]		
Juan-les-Pins	Sentinel-2	Apr./May 2019		X[2]		
Juan-les-Pins	Sentinel-2	Oct./Nov. 2019		X[2]		
Juan-les-Pins	Sentinel-2	Apr./May 2020		X[2]		
Baie des Lecques	Sentinel-2	2015/11/27		X[2]		
Baie des Lecques	Sentinel-2	2016/03/26		X[2]		
Baie des Lecques	Sentinel-2	2016/09/22		X[2]		
Baie des Lecques	Sentinel-2	2017/04/10		X[2]		
Baie des Lecques	Sentinel-2	2017/10/17		X[2]		
Baie des Lecques	Sentinel-2	2018/04/20		X[2]		
Baie des Lecques	Sentinel-2	2018/09/27		X[2]		
Baie des Lecques	Sentinel-2	2019/03/31		X[2]		
Baie des Lecques	Sentinel-2	2019/09/17		X[2]		
Baie des Lecques	Sentinel-2	2020/04/09		X[2]		
Landes	Sentinel-2	2017/01/29		X[2]		
Landes	Sentinel-2	2017/02/08		X[2]		
Landes	Sentinel-2	2017/03/30		X[2]		
Landes	Sentinel-2	2017/04/19		X[2]		
Landes	Sentinel-2	2017/05/09		X[2]		
Landes	Sentinel-2	2017/06/18		X[2]		
Landes	Sentinel-2	2017/07/18		X[2]		
Landes	Sentinel-2	2017/08/17		X[2]		
Landes	Sentinel-2	2017/10/11		X[2]		
Landes	Sentinel-2	2017/11/20		X[2]		
Landes	Sentinel-2	2017/12/25		X[2]		
Landes	Sentinel-2	2018/01/19		X[2]		
Landes	Sentinel-2	2018/03/15		X[2]		
Landes	Sentinel-2	2018/04/19		X[2]		

Landes	Sentinel-2	2018/05/04		X²		
Landes	Sentinel-2	2018/06/23		X²		
Landes	Sentinel-2	2018/07/23		X²		
Landes	Sentinel-2	2018/08/22		X²		
Landes	Sentinel-2	2018/08/27		X²		
Landes	Sentinel-2	2018/09/26		X²		
Landes	Sentinel-2	2018/12/10		X²		

² Qualitative validation

2.4.2 Method of validation

The derived shorelines have been compared with in-situ measurements collected using a GPS and with waterline locations manually derived (digitized) using very high-resolution images (e.g. Pléiades). Cross-shore transects were generated every 20 m. For each product, the distance between the baseline and the waterline versions was computed. After that, the difference between reference waterline (either in-situ measurements or derived from very high-resolution images) and the automatic satellite estimated waterline was determined.

2.4.3 Results and Discussion

To validate the position of an instantaneous waterline extracted from a satellite, we need in-situ data acquired on the same date as the satellite acquisition. As a result, only the waterline extracted from the 2020 Pléiades image could be quantitatively validated. The rest of the products were evaluated for validation in a qualitative manner, based on the scientific and field expertise of our consultant (Aix-Marseille University, CEREGE), for the South French Region (PACA). The global mean absolute distance between GPS data and the waterlines extracted using NDWI2 with Pléiades images is about 1.5 m.

2.5 Algorithm 2G – Waterline detection using binary products from SAR amplitude data (Phase 1)

The algorithm was used to derive the waterline indicator using Sentinel -1 data. After processing the images, minimum values between VV and VH polarizations were computed. The minimum computed product, VV and VH were multiplied to augment the differences between water and land. Waterline indicator was extracted after applying an automated threshold on the multiplication result. This algorithm is used to extract the coastline based on the creation of an average coherence between the pairs of SAR images of each year.

2.5.1 Data and study areas

The waterline indicator was extracted along the Sulina – Sfantu Gheorghe (Romania) coastline from 4 Sentinel-1 images.

Satellite Name	Product Date	Validated in 2019	Validated in 2020	Not validated	Validated 2x
Sentinel -1	2015/08/05		X		
	2016/02/25		X		
	2016/04/25	X			
	2016/09/24		X		

The waterline was extracted from 1993 to 2010 along the Evros and Vistonida – Maroneia coastlines (Greece) from 40 different ERS 1/2 images.

Satellite Name	Product date	Validated in 2019	Validated in 2020	Not validated	Validated 2x
ERS 2	1993: 20/06, 29/08			X	
ERS 2	1995: 14/06, 23/08, 01/11			X	
ERS 2	1996: 03/07, 08/07, 16/10			X	
ERS 2	1997: 01/10			X	
ERS 2	1998: 16/09, 25/11, 30/12			X	
ERS 2	1999: 06/10, 10/11, 15/12			X	
ERS 2	2000: 16/08, 20/09, 25/10			X	
ERS 2	2001: 29/11, 03/01, 27/06, 10/10			X	
ERS 2	2002: 21/08			X	
ERS 2	2003: 28/05,15/10, 24/12			X	
ERS 2	2004: 12/05,16/06, 21/07, 25/08, 29/09			X	
ERS 2	2005: 16/02, 23/03			X	
ERS 2	2006: 01/02, 08/03, 21/06, 13/12			X	
ERS 2	2007: 02/05, 15/08, 28/11			X	
ERS 2	2008: 06/02, 21/05, 30/07, 08/10			X	
ERS 2	2009: 15/07, 23/09			X	
ERS 2	2010: 10/02, 17/03, 21/04, 30/06, 08/09, 17/11			X	
ERS 1	1992: 30/12, 22/06, 27/07, 14/12, 31/08			X	
ERS 2	1993: 23/06, 10/11, 03/05, 20/09, 29/11			X	
ERS 2	1995: 28/12, 14/09, 10/08, 06/07, 01/06, 17/06, 22/07, 26/08, 30/09, 04/11			X	
ERS 2	1996: 07/11, 03/10, 20/06, 16/05, 11/04, 13/01, 06/07			X	

ERS 2	1997: 07/11, 03/10, 20/06, 16/05, 11/04, 13/12			X	
ERS 2	1998: 17/12, 03/09 ,15/08, 19/09, 28/11			X	
ERS 2	1999: 28/10, 23/09, 19/08, 15/07, 22/05, 26/06, 31/07, 18/12			X	
ERS 2	2000: 28/10, 23/09, 19/08, 15/07, 10/06, 15/07, 19/08, 23/09, 28/10, 02/12			X	
ERS 2	2001: 21/12, 06/01, 17/03, 04/08			X	
ERS 2	2002: 21/11, 17/10, 12/09, 04/07, 25/04, 24/08			X	
ERS 2	2003: 06/11, 02/10, 28/08, 24/07, 15/05, 10/04, 06/03, 22/03, 26/04, 13/09, 22/11			X	
ERS 2	2004: 30/12, 25/11, 16/09, 12/08, 08/07, 03/06, 29/04, 15/01, 06/03, 19/06, 24/07, 28/08, 02/10			X	
ERS 2	2005: 15/12, 28/07, 23/06, 10/03, 03/02, 15/01, 19/02, 09/07, 31/12			X	
ERS 2	2006: 15/12, 28/07, 23/06, 10/03, 03/02, 02/09			X	
ERS 2	2007: 20/12, 11/10, 06/09, 24/05, 15/03, 08/02, 24/02, 31/03, 05/05, 18/08, 27/10			X	
ERS 2	2008: 21/08, 08/05, 28/02, 05/01, 06/09, 11/10, 20/12			X	
ERS 2	2009: 24/12, 19/11, 15/10, 06/08, 19/03, 24/01, 04/04, 22/08, 26/09			X	
ERS 2	2010: 30/09, 09/12, 04/11, 26/08, 22/07, 17/06, 13/05, 08/04, 04/03, 28/01 , 09/01, 13/02, 20/03, 24/04, 29/05, 03/07, 07/08, 11/09, 16/10			X	

2.5.2 Method of validation

In order to assess the accuracy of the algorithm for the Romanian coastline, the derived shorelines have been compared with in-situ measurements collected using a GPS. Cross-shore transects were generated every 25 m. For each product, the distance between the baseline and each of the waterline versions was computed. After that, the difference between reference waterline and the automatic satellite estimated waterline was determined.

To validate the products of Greek waterline, the extracted values were compared with data from the Land Registry of Greece, more specifically high resolution orthorectified maps (25cm and 50cm), DTM (1m) and DEM (5m and 2m).

2.5.3 Results

Concerning the results of waterline validation in Romania, the mean absolute error varies between 18 – 49 m for the 4 moments presented above. Maximum error reaches 50 to 100 m. The validation coverage varies between 8 and 30 km according to the validation data available for Sulina – Sfantu Gheorghe site.

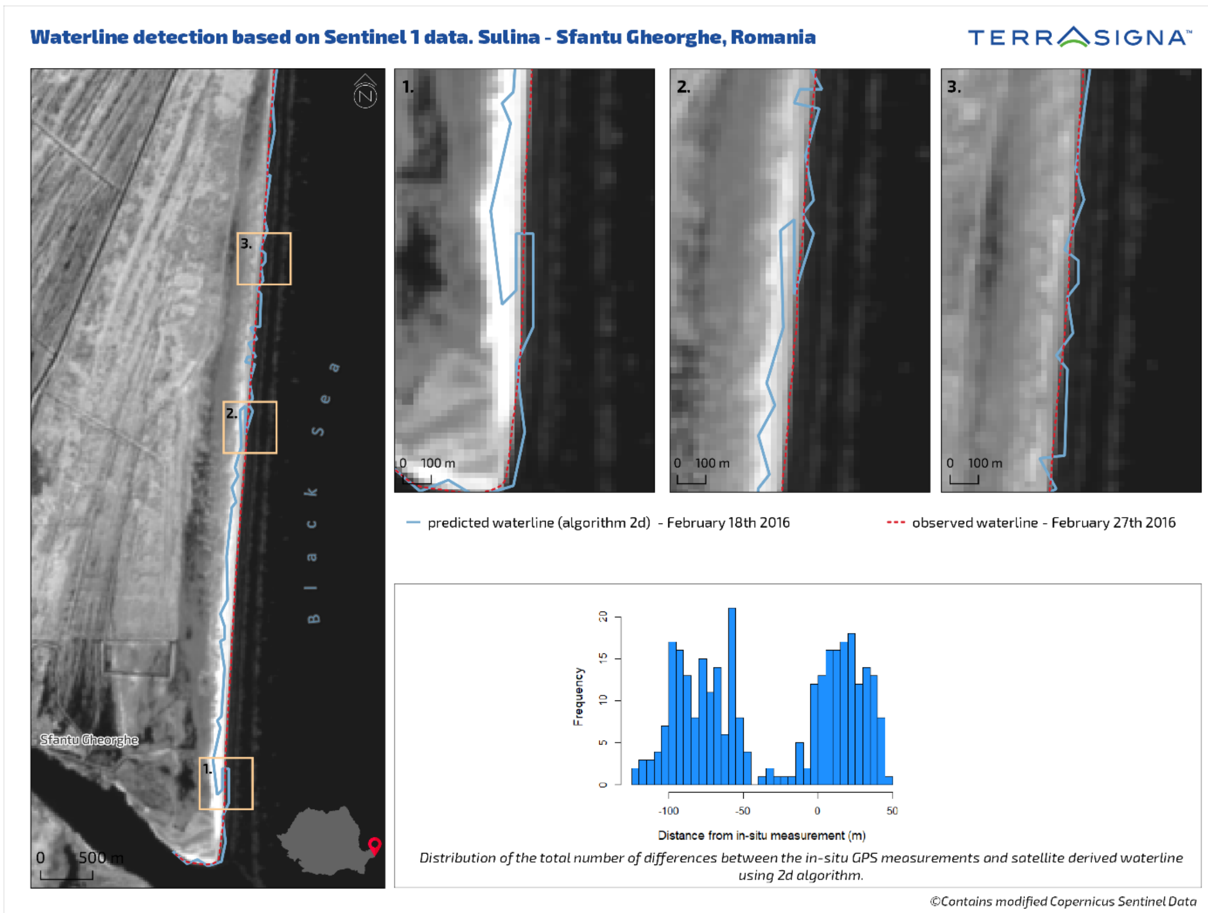

Fig. 18: Waterline detection based on SAR data (Sulina – Sfantu Gheorghe area).

The validation for waterlines extracted from SAR satellite images in Greece is expected to be similar to those produced in Phase 1 (example below).

Fig. 19: Waterline comparison in Greece between validation data from GPS and single waterline method derived from Satellite image Sentinel-1.

2.5.4 Discussion

All the validation results show that an improvement of the methodology is necessary in order to achieve better results.

The validation of the methodology used to derive the waterline based on satellite data (SAR) in Greece will be performed using orthorectified maps, DTM and DEM as reference information. We expect satisfaction accuracy of the algorithm for the ERS1/2 data based on previous research where we have used the same type of method and validation. After all, we expect some errors because of the ERS's spatial resolution and the lack of data.

3 VALIDATION OF INDICATOR 'UPPER SWASH LIMIT'

3.1 Algorithm 2A2F – Upper swash limit using combined NDWI-derived waterlines

Using HR images such as Sentinel-2 (10-m resolution), several waterlines over a short period (2 months max in summer) are combined and the most inland excursion is extracted as the upper swash limit. Using VHR images (Pléiades, 2-m pixel size), the upper swash limit is defined as the wet/dry sand limit. Only one image per date is used.

3.1.1 Data and study areas

The upper swash limit was yearly produced in France for Saint-Raphaël and Camargue coasts, from 2015 to 2020, using Sentinel-2 and Pléiades images.

Satellite Name	Location	Validated in 2019	Validated in 2020	Not validated	Validated 2x
Sentinel-2	Saint-Raphaël		5	1	

	Camargue			5	
Pléiades	Saint-Raphaël		1		1

3.1.2 Discussion

It can be concluded that the detection of the upper swash limit based on HR and VHR imagery satisfies coastal managers monitoring needs in microtidal regions, even if one single image is used (for Pléiades cases), in the case where the limit detected is wet/dry sand.

3.1.3 Method & Data of validation

The validation step consists in measuring the average distance between the GPS waterline and the waterline extracted from satellite data. First, the produced line is converted into point with a fixed distance (every 20m). Then the nearest distance from the point to the reference line is computed. Finally, the error of each point is plotted, and the average error is computed.

The validation data used for upper swash limit validation in France are GPS readings provided by CAVEM (Communauté d'agglomération Var Estérel Méditerranée) for the Gulf of Fréjus (Saint-Raphaël). The available dates are in June 2015, 2016, 2017, 2018, 2019 and September 2020.

3.1.4 Results

The shoreline position validation tests show values smaller than the pixel size of the images used, with the algorithm 2a2f. On the Pléiades images, the upper swash limits get an overall average error of 1.4 m, for a satellite resolution of 2 m. For the upper swash limits derived from Sentinel-2 images (10 m resolution), the absolute average precision obtained is 5.7 m.

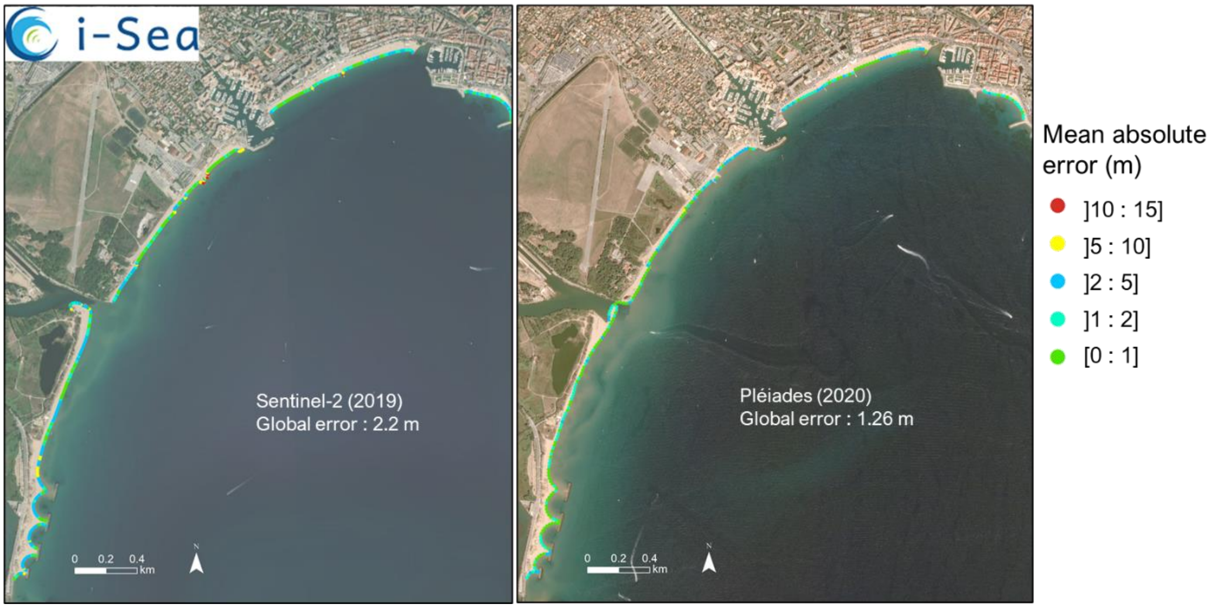

Fig. 20: Mean absolute error every 10-m alongshore. Distance between Sentinel-2-derived upper swash limit and GPS data (left) and between Pléiades-derived upper swash limit and GPS data (right).

4 VALIDATION OF INDICATOR 'DUNE FOOT'

The dune foot position is defined by a break in the slope on the sea-side basal part of the dune.

4.1 Algorithm 3H – Dune foot extraction using supervised classification

Supervised classification method is applied to distinguish the beach area made of sand from the dune area which is usually covered by vegetation or if not by sand ridge casting shadows around.

4.1.1 Data and study areas

In France, the dune foot is extracted from optical satellite images along the New Aquitaine region from SPOT2-4-5 and Sentinel-2 data, yearly from 1987 to 2015 and seasonally from 2015 to 2020 (Autumn and Spring). The dune foot was also extracted from Sentinel-2 images in Normandy (Cotentin) to frame the episode of storm Eleanor during the winter of 2017/2018.

Area	Satellite name	Product date	Validated in 2019	Validated in 2020	Not validated	Validated 2x
Nord Médoc	Sentinel-2	2020/03/19, 2020/03/24, 2020/04/18			X	
Nord Médoc	Sentinel-2	2019/09/26, 2019/10/11, 2019/10/21			X	
Nord Médoc	Sentinel-2	2019/04/09, 2019/04/24			X	
Nord Médoc	Sentinel-2	2018/09/26, 2018/10/21		X		

Nord Médoc	Sentinel-2	2018/04/19, 2018/04/24		X		
Nord Médoc	Sentinel-2	2017/10/11, 2017/10/16, 2017/10/26, 2017/10/31		X		
Nord Médoc	Sentinel-2	2017/03/10, 2017/04/09, 2017/04/19			X	
Nord Médoc	Sentinel-2	2016/09/21, 2016/10/21			X	
Nord Médoc	Sentinel-2	2016/03/15, 2016/05/04			X	
Nord Médoc	SPOT5	2014/06/12		X		
Nord Médoc	SPOT4	2012/09/30		X		
Nord Médoc	SPOT5	2011/08/01			X	
Nord Médoc	SPOT5	2009/10/04		X		
Nord Médoc	SPOT4	2008/09/21			X	
Nord Médoc	SPOT5	2006/07/08			X	
Nord Médoc	SPOT2	2004/07/28		X		
Nord Médoc	SPOT2	2002/09/15			X	
Nord Médoc	SPOT4	2000/09/10			X	
Nord Médoc	SPOT2	1998/02/13			X	
Nord Médoc	SPOT2	1996/07/16		X		
Nord Médoc	SPOT3	1994/07/27			X	
Nord Médoc	SPOT2	1992/09/06, 1992/09/17			X	
Nord Médoc	SPOT2	1990/03/17, 1990/07/04			X	
Nord Médoc	SPOT1	1988/07/08			X	
Nord Médoc	SPOT1	1987/04/23			X	
Cotentin	Sentinel-2	2017/06/01			X	
Cotentin	Sentinel-2	2020/05/26			X	
Cotentin	Sentinel-2	2017/11/13			X	
Cotentin	Sentinel-2	2018/05/07			X	

4.1.2 Method of validation

The validation data are GPS readings from 1998, 2016, 2017, 2018, and 2019, provided by the Côte Aquitaine Observatory and the BRGM, available in the PIGMA catalog. We chose to use these data to estimate the error of the dune foot position for the years 1996, 2004, 2009 2012, 2014, 2017 and 2018, although some years are far from the dates of the in-situ data. This information is important to consider regarding the validation results. We consider them to be overestimated compared to the real precision of the dune foot positions derived from satellite images as natural changes in the dune foot position between the in-situ data and the data retrieved from the satellite are included in the error, in cases where the dates are far apart.

The dune foot changes were also evaluated using results from field surveys during the same period as a part of satellite-derived results in France. These in-situ data were retrieved from the Communauté des Communes Medoc-Atlantique, for the winter 2019-2020. We compared the dune foot changes in m along 3 sites (La Négade, L'Amélie and Le Signal Sud). We also evaluated the dune foot change over the period 2012-2020 with validation data covering the period 2013-2020.

On the ArcGIS GIS platform, points are generated every 20 m along the line of the dune foot extracted from satellite images for these four dates. With the "Near" tool, the distance is measured for each date between each point and the nearest in-situ dune foot position. According to Vos et al. 2019 subpixel accuracy can be reached for waterline extraction along sandy beaches based on supervised classification. Here, an accuracy of the order of the pixel size is expected as the transition between the dune system and the beach is less clear than for the transition between the water and the beach.

4.1.3 Results

The validation results show a global average error of 9.7 m over the 88 km of coastline analysed along the New Aquitaine Region.

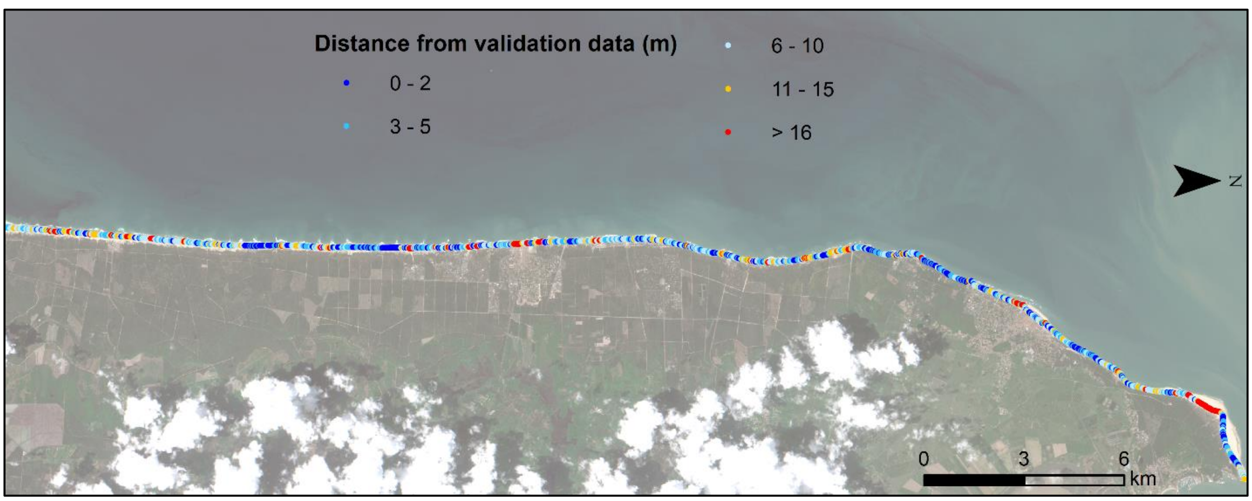

Fig. 21: Distance measured between the dune foot position extracted from the 10/2018 satellite image and the dune foot position measured on field with GPS for the same month.

Concerning the dune foot change rates framing a winter, the validation results show mean distances from the validation data between 0.2 m and 5.78 m, depending on each site, with a global mean distance of 2.3 m (Fig. 22).

In terms of annual change rates over a longer period (2012/13 – 2020), the results for the same sites show a global distance to the in-situ data at about 0.9 m/yr, and values varying from 0.66 and 1.12 m/yr.

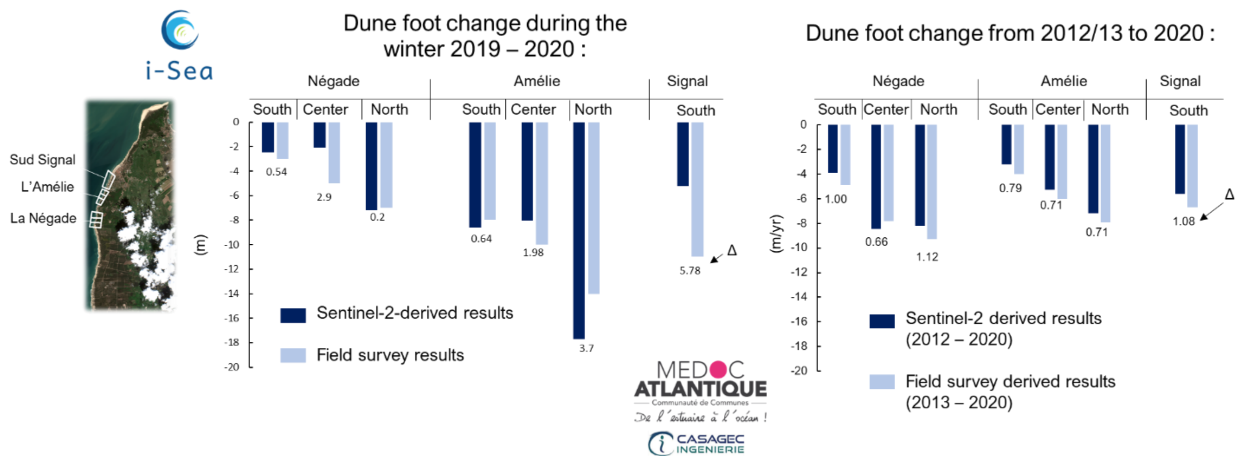

Fig. 22: Comparison of dune foot changes calculated using satellite data and changes measured on field during the winter 2019-2020 (left) and over the period 2012/2013 - 2020.

4.1.4 Discussion

The dune foot is mainly relief information. The planimetric extraction of the dune foot is difficult because of a break in slope generally located on a sedimentary facade with a homogeneous texture (sand). Some observations can contribute to its location (vegetation, shade) but they are all indirect, which explains an overall error close to the pixel size of the satellite image used. We believe that the error can be greatly reduced using VHR images. The results obtained with an overall accuracy of around ten meters are nevertheless of interest for end users (coastal managers) to identify long-term trends (1987 - 2020) and record significant seasonal changes for the period 2015 - 2020.

The validation results present several important points to consider understanding the spatial heterogeneity of the measured errors (Fig. 21), which is not totally related only to the method used and the resolution of the satellite image:

- The date of the in-situ data does not correspond exactly to that of the satellite images which were used to extract the dune foot position. The distance measured between the validation data and that obtained from the algorithm 3h can therefore be linked to a natural coastal morphological evolution between the two dates.
- The definition of the dune foot position in the in situ measurement can locally vary from one operator to another, in particular on accreting sectors where the dune front can be colonized by pioneer vegetation, considered by some experts as the new dune foot, rather than the break in the basal slope of the dune (e.g. North of the sector shown in Fig. 21).

- The error of the in-situ data is itself not zero. This error it is not distinguished in the calculation of the margin of error.

The most important point is the proximity of the results from the analysis of the coastline evolution characterized by the dune foot with those recorded in the field. They present much finer precisions than what the evaluation on the dune foot delimitation suggests. The validation and assessment of expert end-users confirm the interest of using this indicator for hazard for cases with significant episodic or seasonal dynamics, but also for the study of major multi-decade trends, even with high resolution satellite images (of the order of 10 m).

5 VALIDATION OF INDICATOR 'CLIFF LINES'

5.1 Algorithm 3I – Cliff extraction using supervised classification

Regardless of the type of cliff line to be detected, a supervised classification method is applied to discriminate the different classes of ground cover.

Usually the cliff top line will be located by the boundary between the classes: terrestrial vegetation; urbanization; mix of vegetation, and the other classes located seaward the cliff top (water, wet/dry sand/shingle, rock).

For cliff suffering erosion mainly from wave attacks, it can be reasonably assumed that during highest tide level the water domain will be in direct contact with cliff, without presence of beach or low-slopping rocky platforms in between.

5.1.1 Data and study areas

In France, the cliff apex was extracted in Normandy and in the Basque coast:

- Houlgate: 1995 - 2020 (12 SPOT 1-2-3-4-5, and Sentinel-2 satellite images)
- Quiberville: 1995 - 2020 (20 SPOT 2-34-5, Landsat-8, and Sentinel-2 satellite images)
- Corniche: 2017 (1 Pléiades image)

In France, the cliff foot was also retrieved in the same regions:

- Houlgate: 1995 - 2020 (12 SPOT 1-2-3-4-5, and Sentinel-2 satellite images)
- Corniche: 1995 – 2020 (14 SPOT 3-4-5, Sentinel-2, and Pléiades satellite images)
- Erretegia: 1995 – 2020 (11 SPOT 2-4-5, and Sentinel-2 satellite images)

In Portugal, the cliff foot was extracted in 2018 and 2020 from Sentinel-2 images.

Indicator	Area	Satellite name	Product date	Validated in 2019	Validated in 2020	Not validated
Cliff apex	Corniche	Pléiades	2017/07/27	X		
Cliff apex	Quiberville	Sentinel-2	2020/04/23		X	
Cliff apex	Quiberville	Sentinel-2	2018/09/26		X	
Cliff apex	Quiberville	Sentinel-2	2018/06/13		X	
Cliff apex	Quiberville	Sentinel-2	2018/06/03		X	
Cliff apex	Quiberville	Sentinel-2	2018/04/19		X	
Cliff apex	Quiberville	Sentinel-2	2015/08/28		X	
Cliff apex	Quiberville	SPOT5	2012/09/09			X
Cliff apex	Quiberville	SPOT2	1995/06/28			X
Cliff apex	Quiberville	SPOT2	1996/06/05			X
Cliff apex	Quiberville	SPOT4	1998/09/25			X
Cliff apex	Quiberville	SPOT4	2001/05/23			X
Cliff apex	Quiberville	SPOT4	2001/07/24			X
Cliff apex	Quiberville	SPOT5	2003/04/08			X
Cliff apex	Quiberville	SPOT4	2006/09/10			X
Cliff apex	Quiberville	SPOT5	2008/09/27			X
Cliff apex	Quiberville	Landsat 8	2013/07/10		X	
Cliff apex	Quiberville	Sentinel-2	2015/07/16		X	
Cliff apex	Quiberville	Sentinel-2	2017/05/09		X	
Cliff apex	Quiberville	Sentinel-2	2019/05/09			X
Cliff apex	Quiberville	SPOT4	2008/09/27			X

Cliff apex	Houlgate	Sentinel-2	2020/03/24		X	
Cliff apex	Houlgate	Sentinel-2	2017/05/09		X	
Cliff apex	Houlgate	Sentinel-2	2015/09/30		X	
Cliff apex	Houlgate	SPOT5	2012/09/09		X	
Cliff apex	Houlgate	SPOT5	2012/05/25		X	
Cliff apex	Houlgate	SPOT5	2009/06/27		X	
Cliff apex	Houlgate	SPOT4	2006/06/17		X	
Cliff apex	Houlgate	SPOT2	2003/04/16		X	
Cliff apex	Houlgate	SPOT4	2000/09/10		X	
Cliff apex	Houlgate	SPOT2	2000/08/01		X	
Cliff apex	Houlgate	SPOT1	1997/09/22		X	
Cliff apex	Houlgate	SPOT3	1995/04/19		X	
Cliff apex	Leiria	Sentinel-2	2020/05/29			X
Cliff foot	Corniche	Sentinel-2	2020/03/24		X	
Cliff foot	Corniche	Sentinel-2	2017/09/26		X	
Cliff foot	Corniche	SPOT5	2014/06/12		X	
Cliff foot	Corniche	SPOT5	2011/08/01		X	
Cliff foot	Corniche	SPOT5	2008/08/05		X	
Cliff foot	Corniche	SPOT5	2006/07/24		X	
Cliff foot	Corniche	SPOT5	2003/05/15		X	
Cliff foot	Corniche	SPOT5	2002/07/27		X	
Cliff foot	Corniche	SPOT2	2001/10/18		X	
Cliff foot	Corniche	SPOT4	1998/07/23		X	
Cliff foot	Corniche	SPOT3	1995/03/19		X	
Cliff foot	Corniche	Pléiades	2017/07/27		X	
Cliff foot	Corniche	Sentinel-2	2020/05/28		X	
Cliff foot	Erretegia	Sentinel-2	2020/03/24, 2020/04/08, 2020/05/28		X	

Cliff foot	Erretegia	Sentinel-2	2018/06/23, 2018/07/23, 2018/08/22		X	
Cliff foot	Erretegia	Sentinel-2	2017/06/18, 2017/07/18, 2017/08/17		X	
Cliff foot	Erretegia	SPOT5	2014/06/12		X	
Cliff foot	Erretegia	SPOT5	2011/08/01		X	
Cliff foot	Erretegia	SPOT5	2008/08/05		X	
Cliff foot	Erretegia	SPOT4	2005/10/27		X	
Cliff foot	Erretegia	SPOT5	2002/07/27		X	
Cliff foot	Erretegia	SPOT4	1999/09/29		X	
Cliff foot	Erretegia	SPOT2	1997/10/27		X	
Cliff foot	Erretegia	SPOT2	1995/04/11		X	
Cliff foot	Houlgate	Sentinel-2	2020/03/24		X	
Cliff foot	Houlgate	Sentinel-2	2017/05/09		X	
Cliff foot	Houlgate	Sentinel-2	2015/09/30		X	
Cliff foot	Houlgate	SPOT5	2012/05/25		X	
Cliff foot	Houlgate	SPOT5	2009/06/27		X	
Cliff foot	Houlgate	SPOT4	2007/04/05		X	
Cliff foot	Houlgate	SPOT2	2003/06/28		X	
Cliff foot	Houlgate	SPOT5	2003/03/23		X	
Cliff foot	Houlgate	SPOT2	2000/08/01		X	
Cliff foot	Houlgate	SPOT2	1997/07/20		X	
Cliff foot	Houlgate	SPOT3	1995/04/19		X	
Cliff foot	Leiria	Sentinel-2	2018/08/26			X
Cliff foot	Leiria	Sentinel-2	2020/05/29		X	

5.1.2 Method of validation

The cliff lines are validated from cliff lines extracted from very high-resolution DEM (LiDAR), with centimeter precision, in 2016 (for Houlgate, provided by the ROL), 2017 (for Corniche area, provided by the OCA – BRGM), and 2019 (for Quiberville, provided by the Littoral Observatory). The Portuguese cliff data for validation belongs to COSMO Program (APA), obtained by aerial photogrammetry. The lines of equal slopes are extracted every 10°. The isolines are also extracted each 1 m. The combination of these two information makes it possible to precisely identify the slope discontinuity at high altitude (cliff apex) and the equivalent at low altitude (cliff foot). On the ArcGIS GIS platform, points are generated every 20 m along the cliff apex extracted from satellite images. With the "Near" tool, the distance is measured for each date between each point and the nearest in-situ cliff apex for the same date. This process is also performed for the cliff foot.

We chose to use these Lidar data to estimate the error of the cliff line position, although some years are far from the dates of the in-situ data. This information is important to consider regarding the validation results. We consider them to be overestimated compared to the real precision of the cliff line positions derived from satellite images as natural changes in the cliff line position between the in-situ data and the data retrieved from the satellite are included in the error, in cases where the dates are far apart. However, this overestimate is less important than for the dune foot error estimation due to much less dynamics of rocky sea-cliffs.

5.1.3 Results

The validation results show an average error of 9.6 m in the cliff apex positioning (values between 5.1 and 16.6 m), and 10.5 m for the cliff foot one, with results varying between 2.3 m and 17.5 m (Fig. 23, Fig. 24, Fig. 25, Fig. 26).

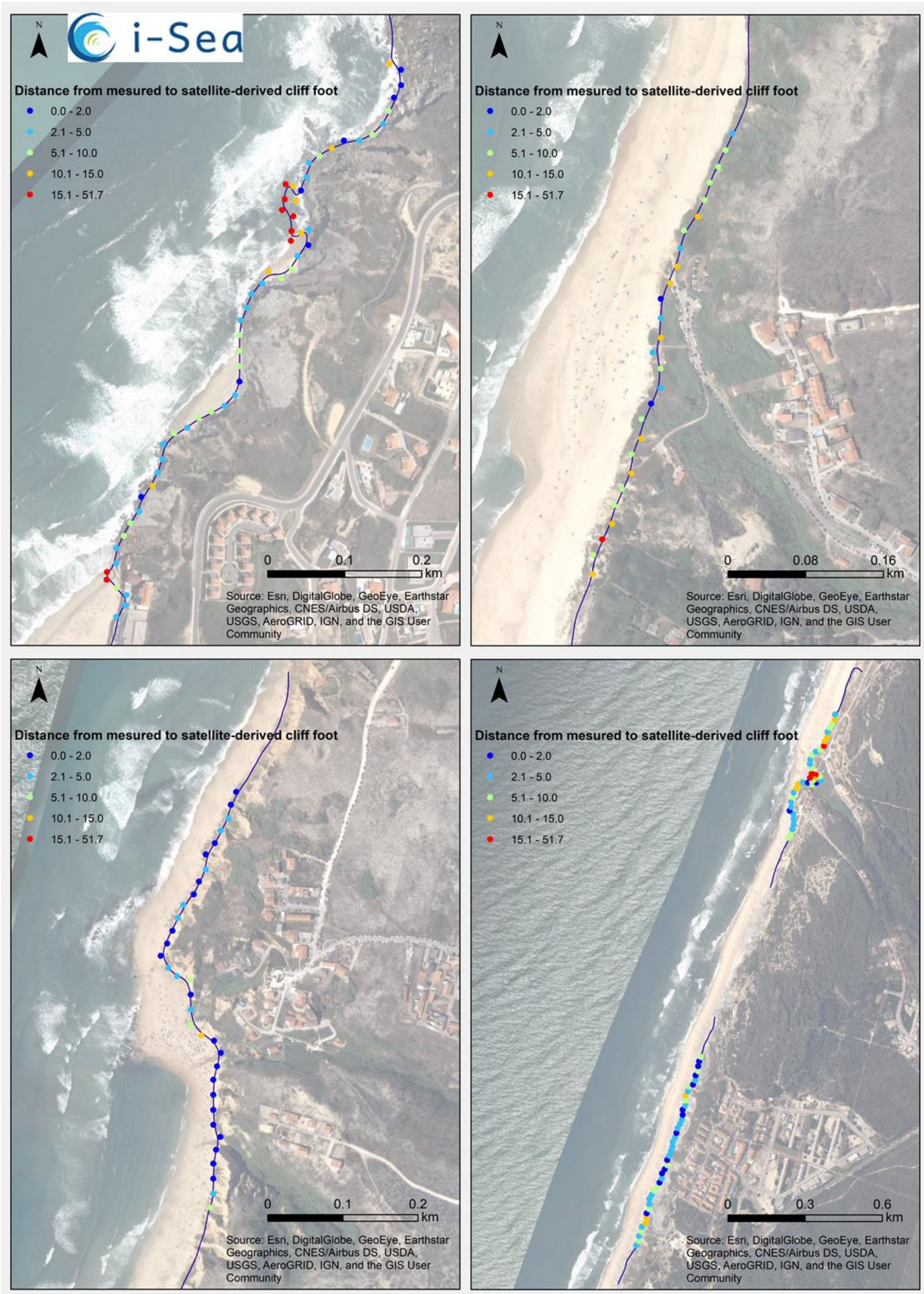

Fig. 23: Cliff foot position validated along the Portugal coast. Comparison between Sentinel-2-derived cliff foot position and Lidar-derived one.

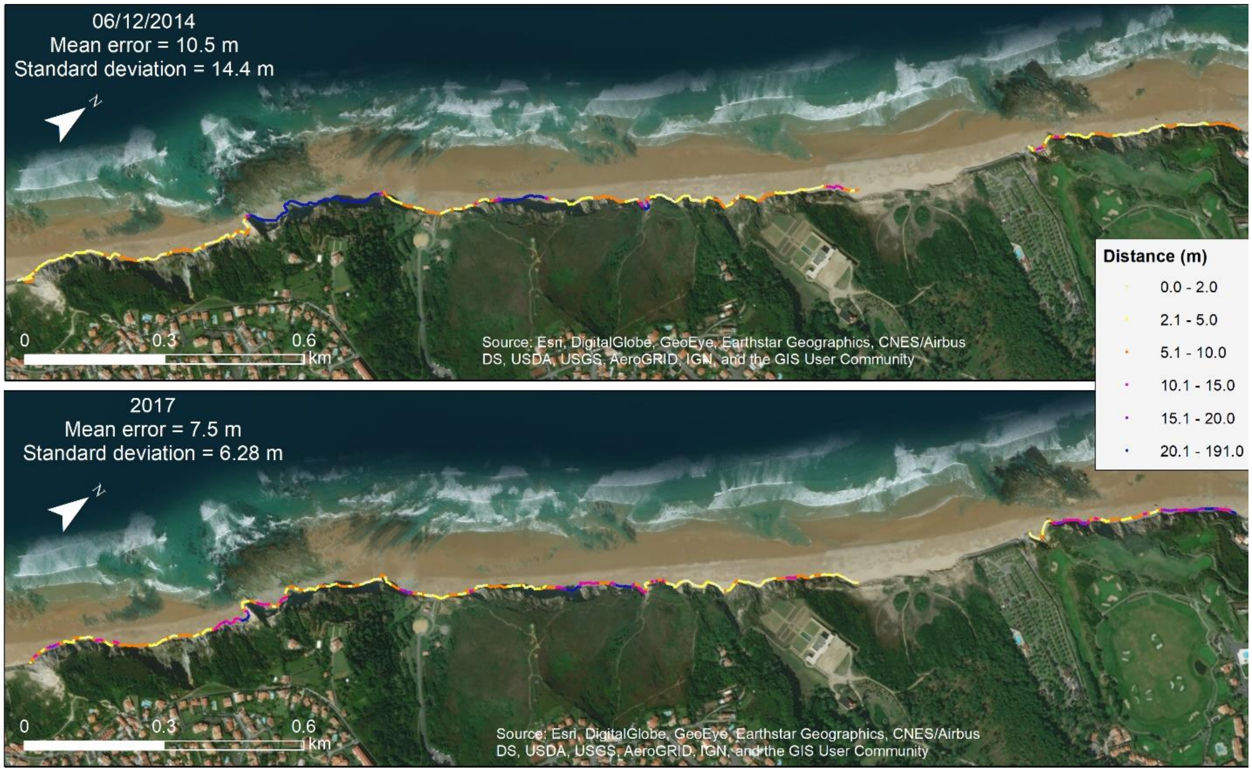

Fig. 24: Distance between satellite-derived (Sentinel-2) and Lidar-derived cliff foot position in 2014 (top) and 2017 (bottom) along the Erretegia coast.

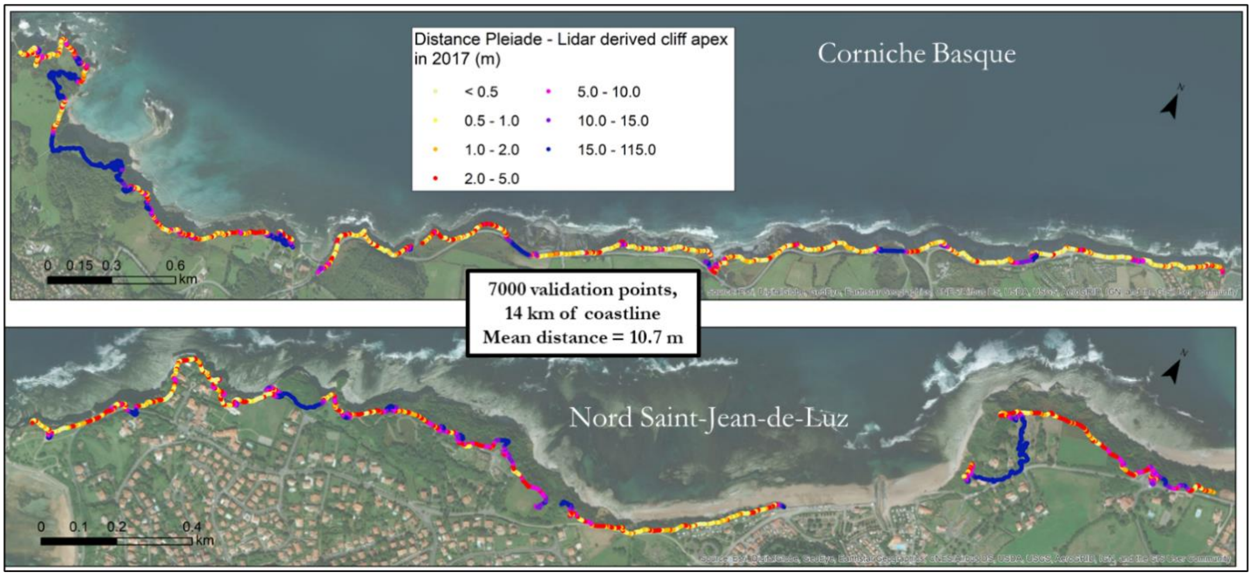

Fig. 25: Distance between satellite-derived (Pléiades) and Lidar-derived cliff apex position in 2017 along the Corniche Basque (top) and Nord Saint-Jean-de-Luz (bottom figure).

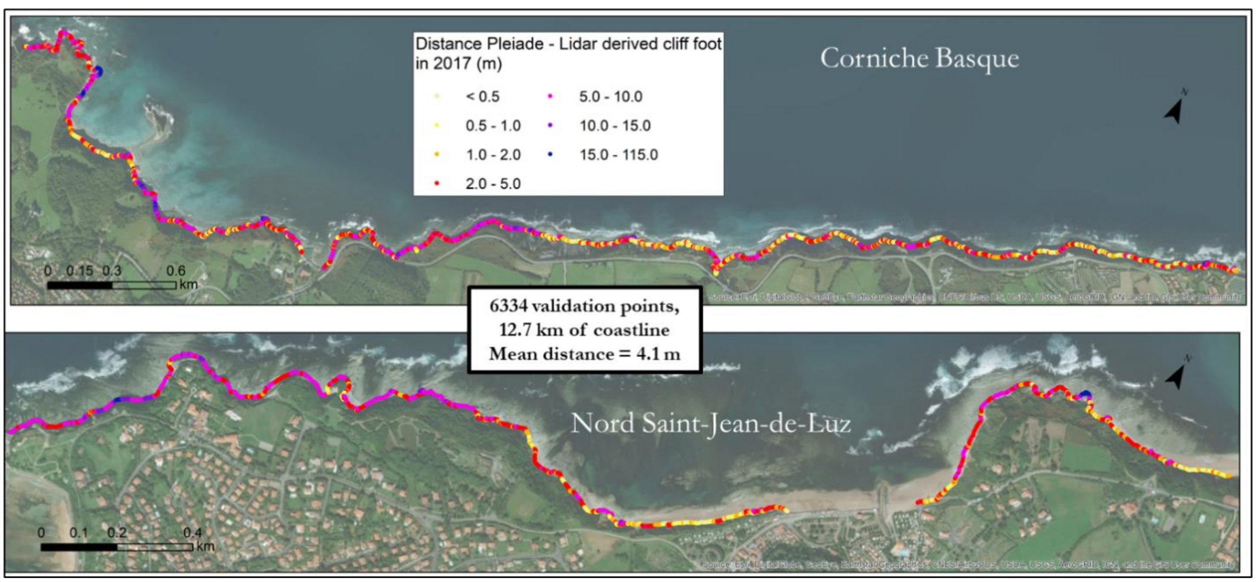

Fig. 26: Distance between satellite-derived (Pléiades) and Lidar-derived cliff foot position in 2017 along the Corniche Basque (top) and Nord Saint-Jean-de-Luz (bottom figure).

5.1.4 Discussion

The results show that the algorithm 3I cannot be applied on any sites. The cliff foot detection requires a sub-vertical wall to distinguish the top from the bottom of cliff on a satellite image.

The analysis of cliff line evolution can be relevant if the real morphological change is larger than the satellite image resolution (brutal landslides), or if the temporal period of analysis is large enough.

The results cannot be used to quantitatively estimate the evolution of the cliff line position because positive values of change, even in the range of the image resolution (here 10m), are not suitable for the consulted end users, as a cliff cannot prograde. Negative change values greater than 10 m precision using Sentinel-2 images (= significant erosion) may however indicate the period, the location, and the magnitude of a gravity movement (e.g. landslide).

5.2 Algorithm 3c – Cliff extraction using the cross-shore variation of the beach/cliff slope

This algorithm relies on the availability of a digital elevation model (DEM) that includes the cliff face and part of the subaerial domains seaward and landward the cliff face so as to have the cliff foot and apex within the DEM. The DEM was computed from photogrammetry using VHR optical images. The proposed algorithm for cliff foot extraction relies on a DEMs provided over a regular mesh.

5.2.1 Data and study areas

In France, the cliff apex was extracted in Normandy and in the Basque coast:

- Houlgate: 1995 - 2020 (12 SPOT 1-2-3-4-5, and Sentinel-2 satellite images)
- Quiberville: 1995 - 2020 (20 SPOT 2-34-5, Landsat-8, and Sentinel-2 satellite images)
- Corniche: 2017 (1 Pléiades image)

In France, the cliff foot was also retrieved in the same regions:

- Houlgate: 1995 - 2020 (12 SPOT 1-2-3-4-5, and Sentinel-2 satellite images)
- Corniche: 1995 – 2020 (14 SPOT 3-4-5, Sentinel-2, and Pléiades satellite images)
- Erretegia: 1995 – 2020 (11 SPOT 2-4-5, and Sentinel-2 satellite images)

In Portugal, the cliff foot was extracted in 2018 and 2020 from Sentinel-2 images.

Indicator	Area	Satellite name	Product date	Validated in 2019	Validated in 2020	Not validated
Cliff apex	Corniche	Pléiades	2017/07/27	X		
Cliff lines	Corniche	Pléiades	2017/07/27		X	

5.2.2 Method of validation

The cliff lines are validated from cliff lines extracted from very high-resolution DEM (LiDAR), with centimeter precision, in 2017 along the Corniche Basque coast (Nouvelle-Aquitaine, France). The lines of equal slopes are extracted every 10°. The isolines are also extracted each 1 m. The combination of these two information makes it possible to precisely identify the slope discontinuity at high altitude (cliff apex) and the equivalent at low altitude (cliff foot). On the ArcGIS GIS platform, points are generated every 20 m along the cliff apex extracted from satellite images. With the "Near" tool, the distance is measured for each date between each point and the nearest in-situ cliff apex for the same date. This process is also performed for the cliff foot.

We chose to use these Lidar data to estimate the error of the cliff line position, although some years are far from the dates of the in-situ data. This information is important to consider regarding the validation results. We consider them to be overestimated compared to the real precision of the cliff line positions derived from satellite images as natural changes in the cliff line position between the in-situ data and the data retrieved from the satellite are included in the error, in cases where the dates are far apart. However, this overestimate is less important than for the dune foot error estimation due to much less dynamics of rocky sea-cliffs.

5.2.3 Results

The validation results show an average error of 2.3 m in the cliff apex positioning, and 1.6 m for the cliff foot one (Fig. 27 and Fig. 28).

Fig. 27: Cliff lines (cliff foot in green, cliff apex in red) extracted from Pléiades-derived DEM in 2017.

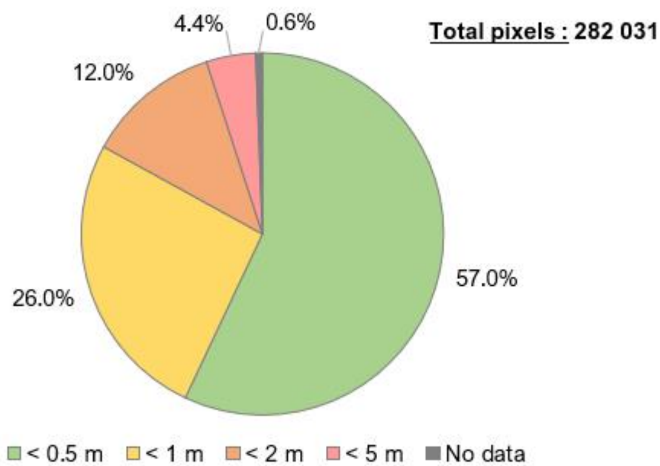

Fig. 28: Vertical coverage of validated DEM extracted from Pléiades-derived photogrammetry and statistics from comparison between vertical elevation of the produced DEM and the LIDAR-derived one.

5.2.4 Discussion

The results show that the algorithm 3c is robust using VHR spatial data to extract accurate the cliff apex position as well as the cliff foot one.

6 VALIDATION OF INDICATOR 'TOP OF THE CLIFF MOVEMENT'

6.1 Algorithm 3J – Top of the cliff movement monitoring using PS

The PS-In SAR technique allowed to perform a pre- and a post-event displacement analysis on the general rock massif stability, evaluating the state of activity of long-term ground displacements.

6.1.1 Data and study areas

The French sites analysed cover heterogeneous coastal areas in New Aquitaine and in Normandy:

- Cap d'Ailly (Quiberville, Varangéville) in Normandy,
- Saint-Jean-de-Luz, Bidart, Corniche, and Erretegia over the Pays Basque.

The algorithm 3j was used to extract the ground movements (vertical velocity movements) from Sentinel-1, ERS and ENVISAT satellite data for the periods 1995-2000 (ERS 1-2), 2003-2007 (Envisat), and 2014-2020 (Sentinel-1).

The validation for the ground deformation products needs robust knowledge of the study areas and the use of different types of data.

In Normandy, various validation data exist to validate interferometric measurement of the cliff vertical movements:

- Airborne Lidar surveys: 2012, 2009, 2016
- Terrestrial Laser Scanning survey of the cliff front: every 3 months since 2010 (Cap d'Ailly)
- GPS since 1992
- Ortho-photos: 2000-2002 and 2011-2014.

6.1.2 Method of validation

For the validation of ground motion, many scientists use a monitoring system based on remote sensing techniques, such as radar interferometry ground-based and terrestrial laser scanning, in order to monitor the ground deformation of the investigated area and to evaluate the residual risk (Frodella et al., 2016). More specific for the top of the cliff movement validation (Martino et al., 2014) use field-based geomechanical investigations and remote geostructural investigations via a terrestrial laser scanner (TLS). Moreover, Crosetto et al., 2011 using as a validation method for the PSI 2D displacement information (in range and azimuth) using images from a single radar instrument.

At this stage, validation data are not yet available to evaluate the satellite-derived results. We then decided to compare the final products extracted using the algorithm PS-DS with the algorithm SBAS (Neokosmidis et al., 2016) for the same areas with the same data.

6.1.3 Results

Results of PS processing obtained by Harris & University of Harokopio are displayed for visual comparison. For the processing were used similar data (Sentinel-1 images with descending orbit) and slightly different options as it is shown below.

	Harris	University of Harukopio
N. of Sentinel-1 images	171 (Oct 2014-Sep 2020)	104 (Oct 2014-Sep 2019)
Software	SARScape (PS)	Gamma (PS+DS)
Coherence Threshold	0.75	0.6
N. of PS detected	2973	4442

Harokopio results show bigger displacement velocity and this is due to threshold. Moreover, results are displayed with a different color scale to allow visual comparison of displacement tendencies. For example, below presented the results for Corniche Basque (Fig. 29, Fig. 30).

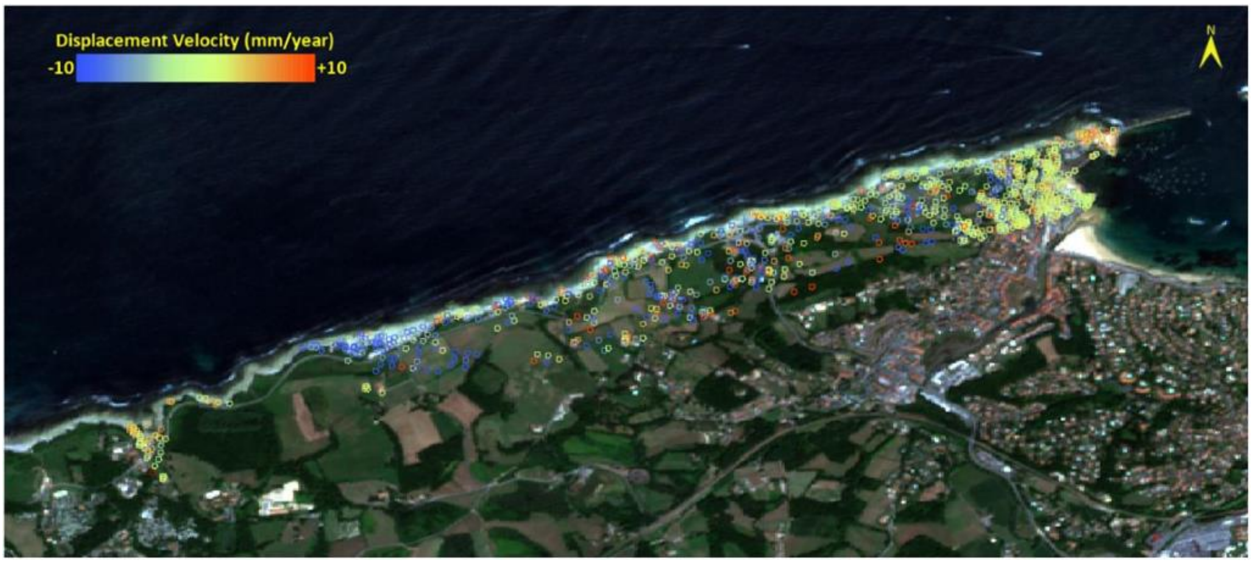

Fig. 29: Displacement map for Corniche Basque with Sentinel 1 data (2014-2019) from Harokopio University.

Fig. 30: Displacement map for Corniche Basque with Sentinel 1 data (2016-2020) from Harris.

To deepen the top of cliff movement evaluation using PSI method, we compared the results with those obtained using another method but the data dataset. The SBAS analysis has been performed using SARscape software on the two study areas (New Aquitaine and Normandy). The input data for this analysis have been a temporal series of Sentinel-1 products covering the period 2016-2020, which provides us a continuity in the observations.

A qualitative comparison on New Aquitaine between PS and SBAS results shows coherent tendencies in the global scale, but significant differences appear when we look more precisely. By example, in some areas, PS might show a locally decreasing displacement velocity while SBAS might show an increase in the same zone. Comparison between PS and SBAS is an interesting approach to confirm tendencies when both point in the same direction, but there is a limitation when found displacements are apposite. In this case, only a validation with ground truth data could allow us to improve our understanding of the phenomena (Fig. 31, Fig. 32).

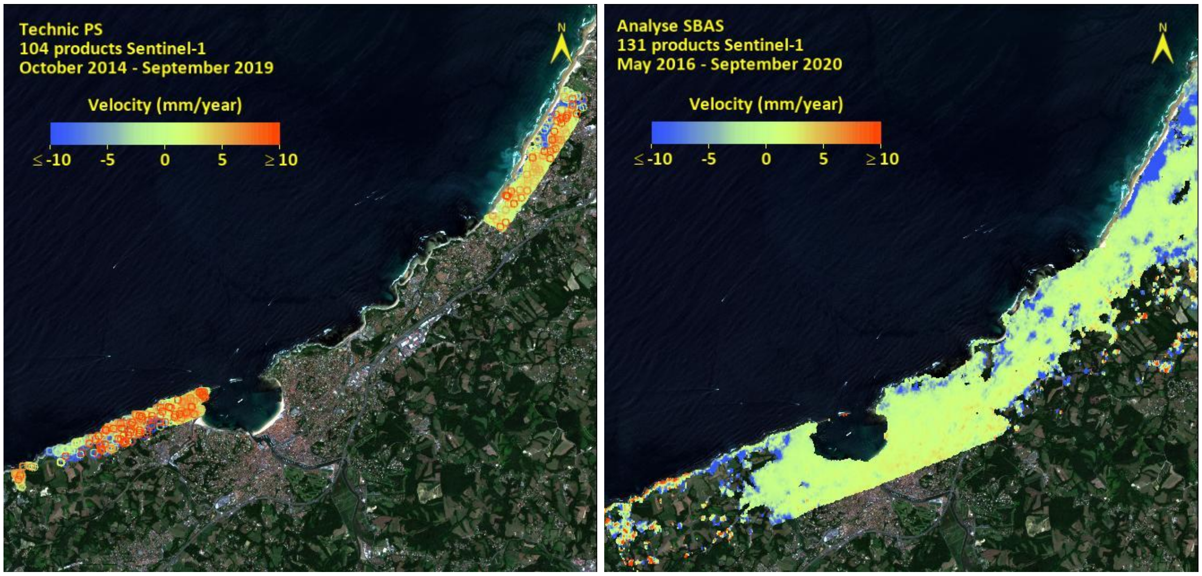

Fig. 31: Visual comparison of the ground velocity deformation derived from PSI (left) and SBAS (right) methods, at Saint-Jean-de-Luz.

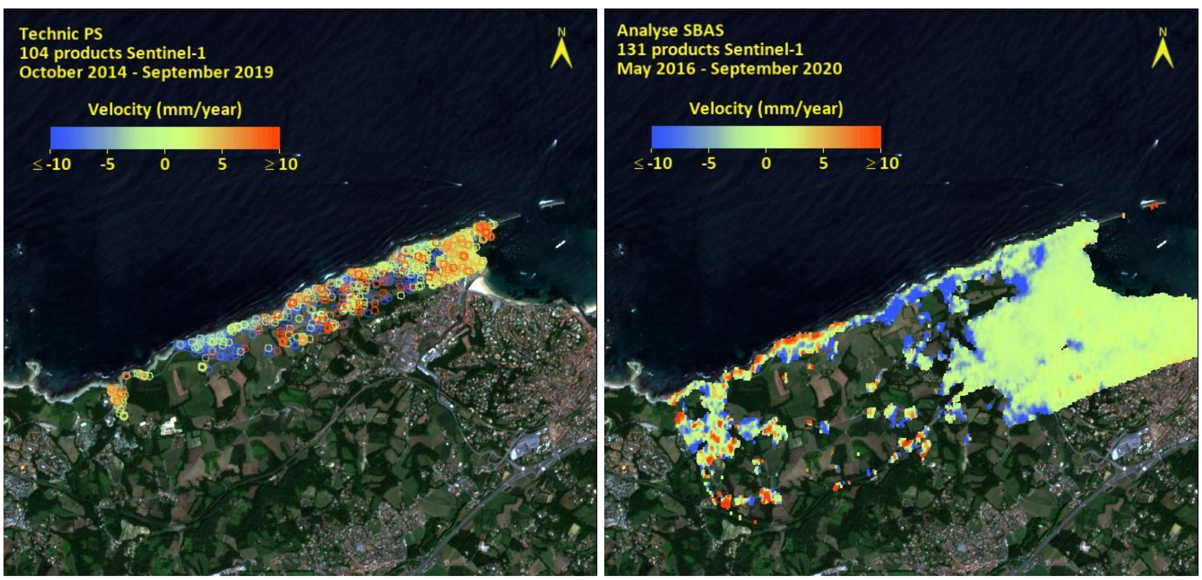

Fig. 32: Visual comparison of the ground velocity deformation derived from PSI (left) and SBAS (right) methods. Zoom over the Corniche cliff sector.

6.1.4 Discussion

The obtained results highlight a satisfactory accuracy of the algorithm for Sar data. The results show relevant values based on the slightly different options that each team used. Moreover, each team used different software's with different principles.

In this case, only a validation with ground truth data could allow us to improve our understanding of the phenomena. In order to achieve this validation several GPS data collect campaigns over the study time period should be performed on the study area.

7 VALIDATION OF INDICATOR 'BATHYMETRY'

7.1 Algorithm 4B – Quasi-analytical model to retrieve bathymetry from HR/VHR optical data

The algorithm 4B extracts the water depth from the estimation of total absorption and backscattering using the attenuation coefficient Kd in accordance with the equations of the QAA (Lee et al., 2002; Capo et al. 2014).

7.1.1 Data and study areas

The bathymetry was extracted from eight coastal areas in France, in Greece, and in Romania using 1 Pléiades, 38 Sentinel-2, and 9 Landsat-8 satellite images. The time series reaches 1995 for the oldest extracted bathymetries (Rhône Delta), and ends in the year 2020 (included).

In France:

- Sud Region:
    - Saint-Raphaël (2015 – 2020)
    - Baie-des-Lecques (2015 – 2020)
    - Camargue (2013 – 2020)
    - Rhône river mouth (1995 - 2020)
    - Beauduc (2013 – 2019)
    - Juan-les-Pins (2015 - 2020)
- Normandie Region :
    - Houlgate (2018)
- Nouvelle-Aquitaine Region :
    - Landes (08/2017 and 08/2018)

In Greece:

- Laganas (2020)

In Romania:

- Sulina-Sfantu-Gheorghe (2016 - 2020)

The validation data were provided by Aix-Marseille University – CEREGE for the Saint-Raphaël coast in July 2017, and by SYMADREM for the Camargue area in July 2018.

Area	Satellite name	Product date	Validated in 2019	Validated in 2020	Not validated	Validated 2x
Camargue	Landsat 8	2013/08/31			X	
Camargue	Landsat 8	2014/09/03			X	
Camargue	Landsat 8	2015/07/20			X	
Camargue	Sentinel-2	2016/09/02			X	
Camargue	Sentinel-2	2017/10/12			X	
Camargue	Sentinel-2	2018/07/29	X			
Camargue	Sentinel-2	2019/08/08			X	
Camargue	Sentinel-2	2020/07/23			X	
Beauduc	Landsat 8	2013/08/15			X	
Beauduc	Landsat 8	2014/09/03			X	
Beauduc	Landsat 8	2015/07/20, 2015/08/05, 2015/08/21			X	
Beauduc	Sentinel-2	2016/05/05			X	
Beauduc	Sentinel-2	2016/09/02			X	
Beauduc	Sentinel-2	2017/04/10			X	
Beauduc	Sentinel-2	2017/10/05			X	
Beauduc	Sentinel-2	2018/04/20			X	
Beauduc	Sentinel-2	2018/09/20			X	
Beauduc	Sentinel-2	2019/03/31			X	
Beauduc	Sentinel-2	2019/08/08			X	
Beauduc	Sentinel-2	Apr./May 2020			X	
Embouchure du Rhône	Landsat 5 6 7 8	Summer 1995			X	
Embouchure du Rhône	Landsat 5 6 7 8	Summer 1996			X	
Embouchure du Rhône	Landsat 5 6 7 8	Summer 1997			X	
Embouchure du Rhône	Landsat 5 6 7 8	Summer 1998			X	
Embouchure du Rhône	Landsat 5 6 7 8	Summer 1999			X	
Embouchure du Rhône	Landsat 5 6 7 8	Summer 2000			X	

Embouchure du Rhône	Landsat 5 6 7 8	Summer 2001			X	
Embouchure du Rhône	Landsat 5 6 7 8	Summer 2002			X	
Embouchure du Rhône	Landsat 5 6 7 8	Summer 2003			X	
Embouchure du Rhône	Landsat 5 6 7 8	Summer 2004			X	
Embouchure du Rhône	Landsat 5 6 7 8	Summer 2005			X	
Embouchure du Rhône	Landsat 5 6 7 8	Summer 2006			X	
Embouchure du Rhône	Landsat 5 6 7 8	Summer 2007			X	
Embouchure du Rhône	Landsat 5 6 7 8	Summer 2008			X	
Embouchure du Rhône	Landsat 5 6 7 8	Summer 2009			X	
Embouchure du Rhône	Landsat 5 6 7 8	Summer 2010			X	
Embouchure du Rhône	Landsat 5 6 7 8	Summer 2011			X	
Embouchure du Rhône	Landsat 5 6 7 8	Summer 2012			X	
Embouchure du Rhône	Landsat 5 6 7 8	Summer 2013			X	
Embouchure du Rhône	Landsat 5 6 7 8	Summer 2014			X	
Embouchure du Rhône	Landsat 5 6 7 8	Summer 2015			X	
Embouchure du Rhône	Landsat 5 6 7 8	Summer 2016			X	
Embouchure du Rhône	Landsat 5 6 7 8	Summer 2017			X	
Embouchure du Rhône	Landsat 5 6 7 8	Summer 2018			X	
Embouchure du Rhône	Landsat 5 6 7 8	Summer 2019			X	
Embouchure du Rhône	Landsat 5 6 7 8	Summer 2020			X	
Golfe de Fréjus	Pléiades	2017/07/06		X		
Golfe de Fréjus	Sentinel-2	2019			X	

Golfe de Fréjus	Sentinel-2	2019			X	
Golfe de Fréjus	Landsat	2017	X			
Golfe de Fréjus	Sentinel-2	2017		X		
Golfe de Fréjus	Sentinel-2	2015/11/17			X	
Golfe de Fréjus	Sentinel-2	2016/04/22			X	
Golfe de Fréjus	Sentinel-2	2016/10/02			X	
Golfe de Fréjus	Sentinel-2	2017/04/07			X	
Golfe de Fréjus	Sentinel-2	2017/10/12			X	
Golfe de Fréjus	Sentinel-2	2018/04/22			X	
Golfe de Fréjus	Sentinel-2	2018/09/29			X	
Golfe de Fréjus	Sentinel-2	2019/03/23			X	
Golfe de Fréjus	Sentinel-2	2019/09/29			X	
Golfe de Fréjus	Sentinel-2	2020/04/09			X	
Juan-les-Pins	Sentinel-2	Oct./Nov. 2015			X	
Juan-les-Pins	Sentinel-2	Apr./May 2016			X	
Juan-les-Pins	Sentinel-2	Oct./Nov. 2016			X	
Juan-les-Pins	Sentinel-2	Apr./May 2017			X	
Juan-les-Pins	Sentinel-2	Oct./Nov. 2017			X	
Juan-les-Pins	Sentinel-2	Apr./May 2018			X	
Juan-les-Pins	Sentinel-2	Oct./Nov. 2018			X	
Juan-les-Pins	Sentinel-2	Apr./May 2019			X	
Juan-les-Pins	Sentinel-2	Oct./Nov. 2019			X	
Juan-les-Pins	Sentinel-2	Apr./May 2020			X	
Baie des Lecques	Sentinel-2	2015/11/27			X	
Baie des Lecques	Sentinel-2	2016/03/26			X	
Baie des Lecques	Sentinel-2	2016/09/22			X	

Baie des Lecques	Sentinel-2	2017/04/10			X	
Baie des Lecques	Sentinel-2	2017/10/17			X	
Baie des Lecques	Sentinel-2	2018/04/20			X	
Baie des Lecques	Sentinel-2	2018/09/27			X	
Baie des Lecques	Sentinel-2	2019/03/31			X	
Baie des Lecques	Sentinel-2	2019/09/17			X	
Baie des Lecques	Sentinel-2	2020/04/09			X	
Houlgate	Sentinel-2	2018/07/23, 2018/07/26, 2018/08/05, 2018/10/21			X	
Sulina-Sfantu-Gheorghe	Sentinel-2	2016/08/16			X	
Sulina-Sfantu-Gheorghe	Sentinel-2	2017/08/06			X	
Sulina-Sfantu-Gheorghe	Sentinel-2	2018/08/31			X	
Sulina-Sfantu-Gheorghe	Sentinel-2	2019/08/06			X	
Sulina-Sfantu-Gheorghe	Sentinel-2	2020/03/13			X	
Laganas	Sentinel-2	2020/02/23			X	
Landes	Sentinel-2	2017/08/12, 2017/08/17			X	
Landes	Sentinel-2	2018/08/12, 2018/08/22, 2018/08/27, 2018/09/01			X	
Landes	Sentinel-2	2017/12/08			X	
Landes	Sentinel-2	2017/17/08			X	
Landes	Sentinel-2	2018/12/08			X	
Landes	Sentinel-2	2017/22/08			X	
Landes	Sentinel-2	2018/27/08			X	
Landes	Sentinel-2	2018/01/09			X	

7.1.2 Method and results of validation

Prior to the validation, available field bathymetric data are resampled at the spatial resolution of the satellite image. If multiple data are available within a same pixel, a criterion based on the standard deviation is used to discard data located over steep gradients. Besides, the satellite derived bathymetry is also corrected to take the tide level into account and bring the result to the same tidal reference as field data. If a calibration step is necessary, the pre-processed dataset is split in half, one set is used for the calibration and the other for the validation.

Several validation outputs are produced. First, a scatterplot between field data and the estimated depth is computed to represent how both data depending on the depth (Fig. 33).

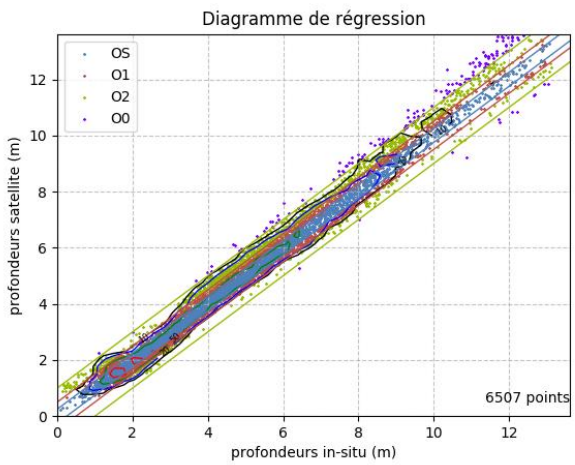

Fig. 33: Regression diagram between field data and satellite derived bathymetry with isolines and dots corresponding to OHI orders (blue line and dots: +/- 0.25 m – Special Order, red line and dots – Order 1: +/- 0.5 m, green line and dots – Order 2: +/- 1 m, purple dots – Order 0: > +/- 1 m).

Second, an absolute difference map (Satellite derived depth – Observed depth) is computed in order to identify more or lesser accurate areas (Fig. 34). Finally, statistics, such as bias, RMSE, absolute mean error and relative mean error are computed and stored.

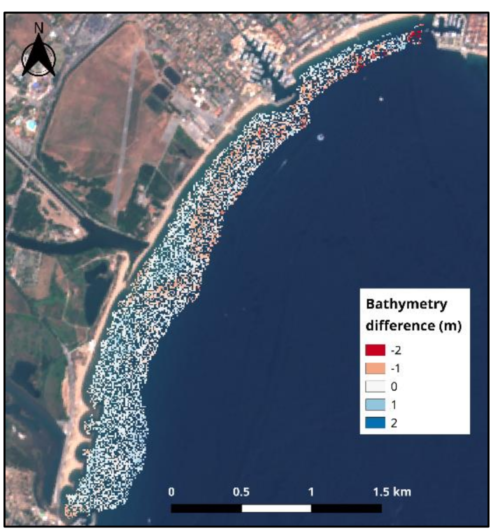

Fig. 34: Example of a difference map between satellite derived bathymetry and observed bathymetry.

The validation tests show mean absolute vertical errors between 0.28 (RMSE 0.43 m) and 0.49 m (RMSE 0.79 m). The validations were carried out on two separate sites, one covering 7 km of anthropized coastline (Saint-Raphaël), the other extended over approximately 100 km (Camargue) and covering a turbid river mouth area.

Comparative tests were also carried out between the results obtained from the LYZENGA model and those from the QAB model (Refer to the Technical Specification deliverable for more details). The validation shows that the bathymetry obtained from the LYZENGA model (which has in-situ control data) is more robust (0.28 m of vertical error) than the second (0.32 m of error for the same area at the same date) (Fig. 35).

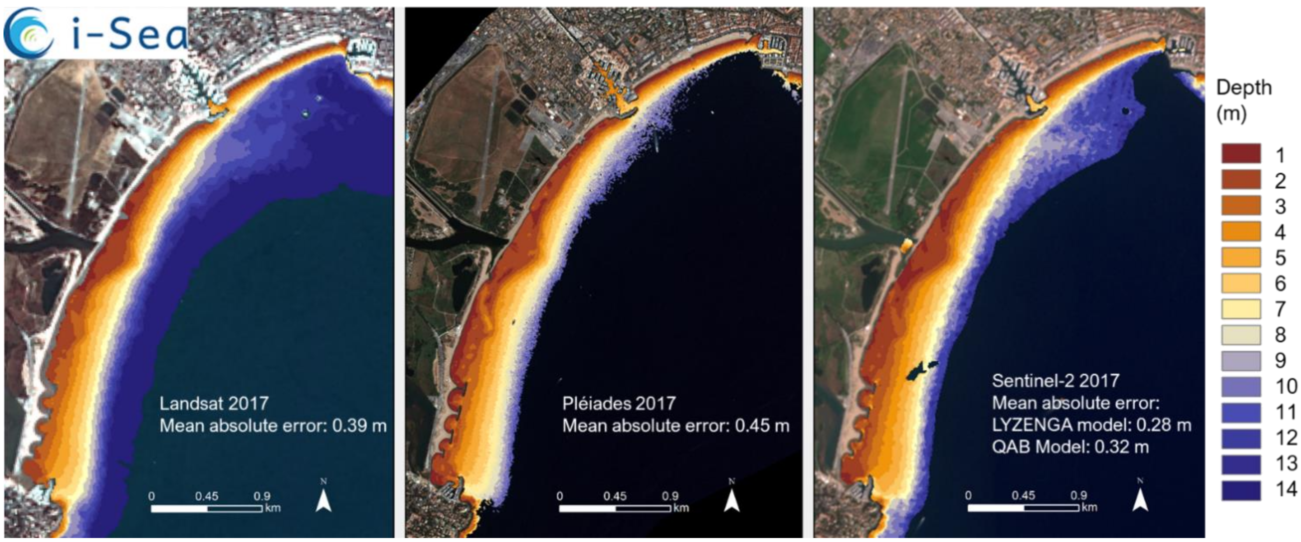

Fig. 35: Comparison between global average errors obtained using Landsat (left), Pléiades (center), and Sentinel-2 (right) satellite images to product bathymetry.

7.1.3 Discussion

The obtained results highlight a satisfactory accuracy of the algorithm for optical images. The results show relevant values from 1 to ~12 m-depth allowing to deduce bathymetry changes between 2 dates and changes in sedimentary volumes/budget. The main limits encountered for the extraction of the bathymetry are an excess of turbidity and a textural heterogeneity of the bottom (presence of seagrass beds, rocks).

7.2 Algorithm 4C – Bathymetry swell inversion

The algorithm is used to obtain the bathymetry through the application of: (i) the Fast Fourier Transform (FFT) or (ii) Wavelet Transform (WT) over Synthetic-Aperture Radar (SAR) image to obtain a directional spectrum and then, to calculate the wavelength and wave direction. After that, the water depth is estimated from linear wave theory (Abreu et al., 2019; Pereira et al., 2019).

7.2.1 Data and study areas

The bathymetries were derived in 2011 and from 2015 to 2020 along the West Portuguese coast from one ERS-2 and eleven different Sentinel-1 images, and in 2018 along the Southwest French coast from one Sentinel-1 image (Table below).

Satellite Name	Product Date	Validated in 2019	Validated in 2020	Not validated (no data for validation)	Validation 2x
ERS-2	16/02/2011[a]	X[C]	-	X	-
Sentinel 1	30/01/2015[b]	X[C]	X	-	-
	31/01/2016[b]	-	X	-	-
	31/01/2017[b]	-	X	-	-
	02/01/2018[b]	-	X	-	-
	20/01/2018[b]	-	X	-	-
	25/03/2018[a]	X[D]	-	-	-
	02/02/2019[a&b]	-	X	-	-
	28/01/2020[b]	-	X	-	-

[a] Satellite Derived Bathymetry during 1st Phase using algorithm 4c-i- FFT.

[b] Satellite Derived Bathymetry during 2nd Phase using both algorithms 4c-i-FFT and 4c-ii-WT.

[c] Satellite Derived Bathymetry during 1st Phase was compared with available Observed Bathymetry from 2013 provided by the Oceanographic Observatory of the Iberian Margin (RAIA Observatory) in the framework of MarRISK project (0262_MarRISK_1_E).

[d] Validation was uncompleted because of FFT is not suitable to shallower depths (*i.e.* $z<15$ m). Satellite Derived Bathymetry using algorithm 4c-ii-WT is still under investigation.

7.2.2 Method of validation

The validation method consists in the comparison between a set of nearshore observed and satellite derived depth contour lines (i.e. isobaths). The values of depth at the location of observed isobaths are extracted from the satellite derived bathymetry. Then, the depth differences are computed from satellite and observed bathymetry (Eq.1):

Depth difference= Depth observed – Depth satellite derived (Eq.1)

A total of 144 isobaths of satellite – in-situ match-up pairs where used in order to quantify the accuracy of the algorithm 4c-ii-WT and the capabilities offered by Earth Observation data sources to derive the nearshore bathymetry in coasts exposed to high wave energy.

Furthermore, the accuracy between different kind of spectrum analysis in the algorithm 4c (i.e. WT and FFT) was assessed. Firstly, the isobaths extracted from WT and FFT satellite derived bathymetry from 2015 were compared with the bathymetry provided by the Oceanographic Observatory of the Iberian Margin (RAIA Observatory) from 2013 that covers shallow and deep water. Secondly, more than 50 isobaths of WT– FFT derived bathymetry match-up pairs were also analyzed.

7.2.3 Results

Over the 68 Km of coastline validated with WT, the global results show that Mean Absolute Error (MAE) ranges from 0.23 to 5.83 m with a mean value of 2.33 m and the Root Mean Square Error (RMSE) varies between 0.31 and 6.09 with a mean value of 2.57 (Fig. 36).

Over the 90km of coastline compared with RAIA Observatory bathymetry for depths between 15 and 35 m, the results disclose a MAE from 1.97 to 4.12 m for WT and from 7.29 to 13.13 m for FFT, and a RMSE from 2.45 to 4.93 m for WT and from 7.61 to 13.83 m for FFT.

Over the 140 km of coastline compared with FFT, the results an average MAE of 6.45 m and an average RMSE of 7.46 m.

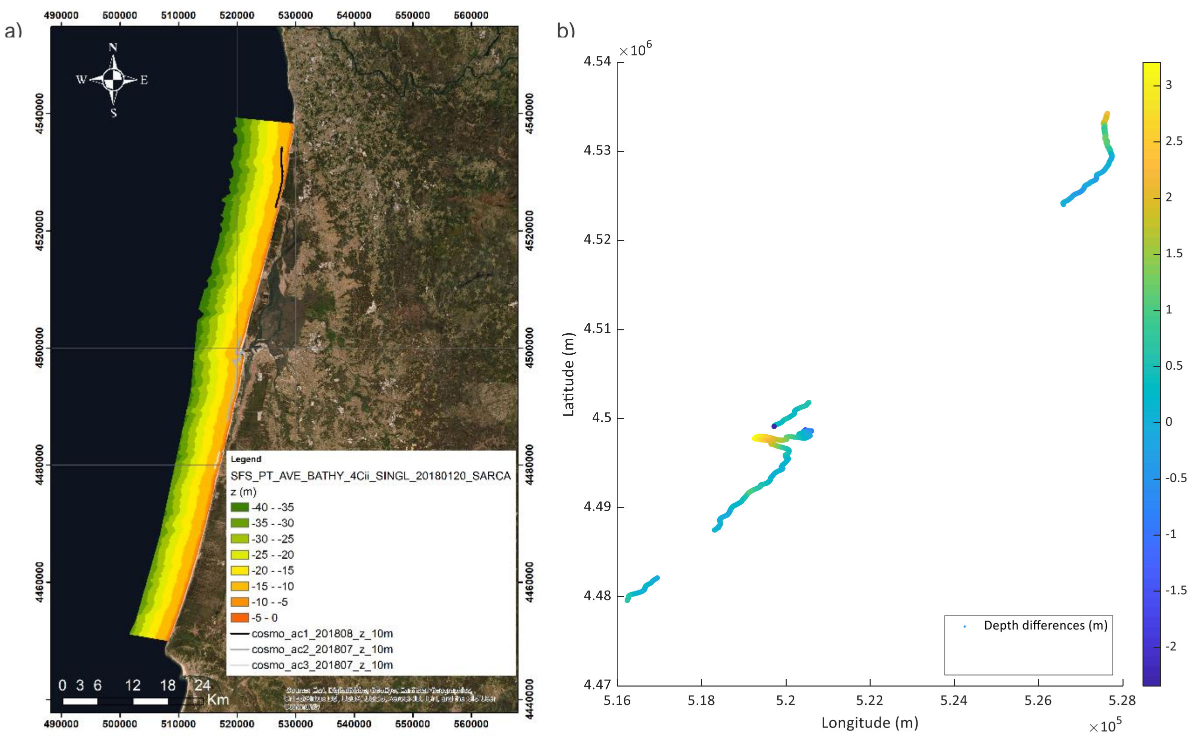

Fig. 36: a) Satellite Derived Bathymetry using WT from Sentinel-1A image (Date: 20/01/2018) at Aveiro Region Coast (NW Portugal) with the observed 10m-isobath from COSMO Program (Dates: 07/2018 and 08/2018) (black, dark and light grey lines). b) Depth differences in meters between observed 10m- isobath and satellite derived depths at isobath location.

7.2.4 Discussion

The obtained results highlight a satisfactory accuracy of the algorithm for Sentinel-1 imagery. The utilization of Wavelet Transform improves the obtained results with Fourier Fast Transform (decrease of MAE in a quarter). Furthermore, the Wavelet Transform allows to derive suitable bathymetry even in shallow water (e.g., z=2 m average MAE is of 1.38 m).

8 VALIDATION OF INDICATOR ‘SUBMERGED SANDBAR POSITION’

The sandbar location is defined as the position of the external sandbar crest punctually extracted from optical satellite imagery.

8.1 Algorithm 6A – Submerged sand banks

Algorithm 6a was used to compute the submerged sandbars. The algorithm is used to extract each submerged sandbar position using perpendicular profiles along the shoreline, based on multispectral satellite imagery (Tatui and Constantin, 2020). For each profile, reflectance values are extracted, thus taking advantage of all information in the visible part of the electromagnetic spectrum. Sandbars crests positions are computed based on iterative statistical method. The algorithm can be applied automatically on long time series of satellite imagery.

8.1.1 Data and study areas

The indicator was derived from 4 Sentinel-2 images, one Landsat 5 product and two higher resolution inputs - one Spot 7 and one Pleiades 1B image for Sulina – Sfantu Gheorghe area.

Satellite Name	Product Date	Validated in 2019	Validated in 2020	Not validated	Validated 2x
Sentinel -2	2016/04/28	X			
	2017/04/03	X			
	2017/11/14	X			
	2018/07/17	X			
Landsat 5	2011/05/22		X		
Spot-7	2017/10/18	X			
Pléiades 1B	2018/06/22	X			

In France, algorithm 6a was used to extract the sandbar location and movements along the New Aquitaine coast, monthly, over 4 years, using Sentinel-2 images.

Area	Satellite name	Product date	Validated in 2019	Validated in 2020	Not validated	Validated 2x
Landes	Sentinel-2	2017/01/29			X	
Landes	Sentinel-2	2017/02/08			X	
Landes	Sentinel-2	2017/03/30			X	
Landes	Sentinel-2	2017/04/19			X	
Landes	Sentinel-2	2017/05/09			X	
Landes	Sentinel-2	2017/06/18			X	
Landes	Sentinel-2	2017/07/18			X	
Landes	Sentinel-2	2017/08/17			X	
Landes	Sentinel-2	2017/10/11			X	
Landes	Sentinel-2	2017/11/20			X	
Landes	Sentinel-2	2017/12/25			X	
Landes	Sentinel-2	2018/01/19			X	
Landes	Sentinel-2	2018/03/15			X	
Landes	Sentinel-2	2018/04/19			X	
Landes	Sentinel-2	2018/05/04			X	
Landes	Sentinel-2	2018/06/23			X	
Landes	Sentinel-2	2018/07/23			X	
Landes	Sentinel-2	2018/08/22			X	
Landes	Sentinel-2	2018/08/27			X	
Landes	Sentinel-2	2018/09/26			X	
Landes	Sentinel-2	2018/12/10			X	
Landes	Sentinel-2	2015/08/28			X	
Landes	Sentinel-2	2015/12/26			X	
Landes	Sentinel-2	2016/04/24			X	
Landes	Sentinel-2	2016/06/23			X	
Landes	Sentinel-2	2016/08/02			X	
Landes	Sentinel-2	2016/10/31			X	
Landes	Sentinel-2	2016/11/30			X	
Landes	Sentinel-2	2019/01/24			X	
Landes	Sentinel-2	2019/02/13			X	

Landes	Sentinel-2	2019/04/19			X	
Landes	Sentinel-2	2019/06/13			X	
Landes	Sentinel-2	2019/08/17			X	
Landes	Sentinel-2	2019/10/11			X	
Landes	Sentinel-2	2020/01/05			X	
Landes	Sentinel-2	2020/02/18			X	
Landes	Sentinel-2	2020/04/08			X	
Landes	Sentinel-2	2020/06/22			X	
Landes	Sentinel-2	2020/06/27			X	
Landes	Sentinel-2	2020/08/06			X	
Landes	Sentinel-2	2020/10/05			X	

8.1.2 Method of validation

For validation purposes, the sandbars positions were extracted from four different Sentinel-2 images, one Landsat 5 scene and two higher resolution inputs - one Spot 7 and one Pleiades 1B image. The extracted values were then compared with in-situ measurements, consisting of sandbars crest positions determined based on bathymetric measurements performed by the Sfantu Gheorghe Marine and Fluvial Research Station (SCMF). More than 170 individual pairs of satellite – in-situ match-up pairs where used to quantify the accuracy of the algorithm and the capabilities offered by different Earth Observation data sources to extract the sandbars.

8.1.3 Results

The validation results for sandbars along the Sulina – Sfantu Gheorghe area show a mean error of 6.72 m for products extracted from Sentinel-2 images, 9.37 m for those from Landsat-5 image, 3.87 for the Pléiades-derived product and 3.35 for the SPOT-7 one. The validation was over 15 km of coastline between Sulina and Sfantu Gheorghe (Fig. 37).

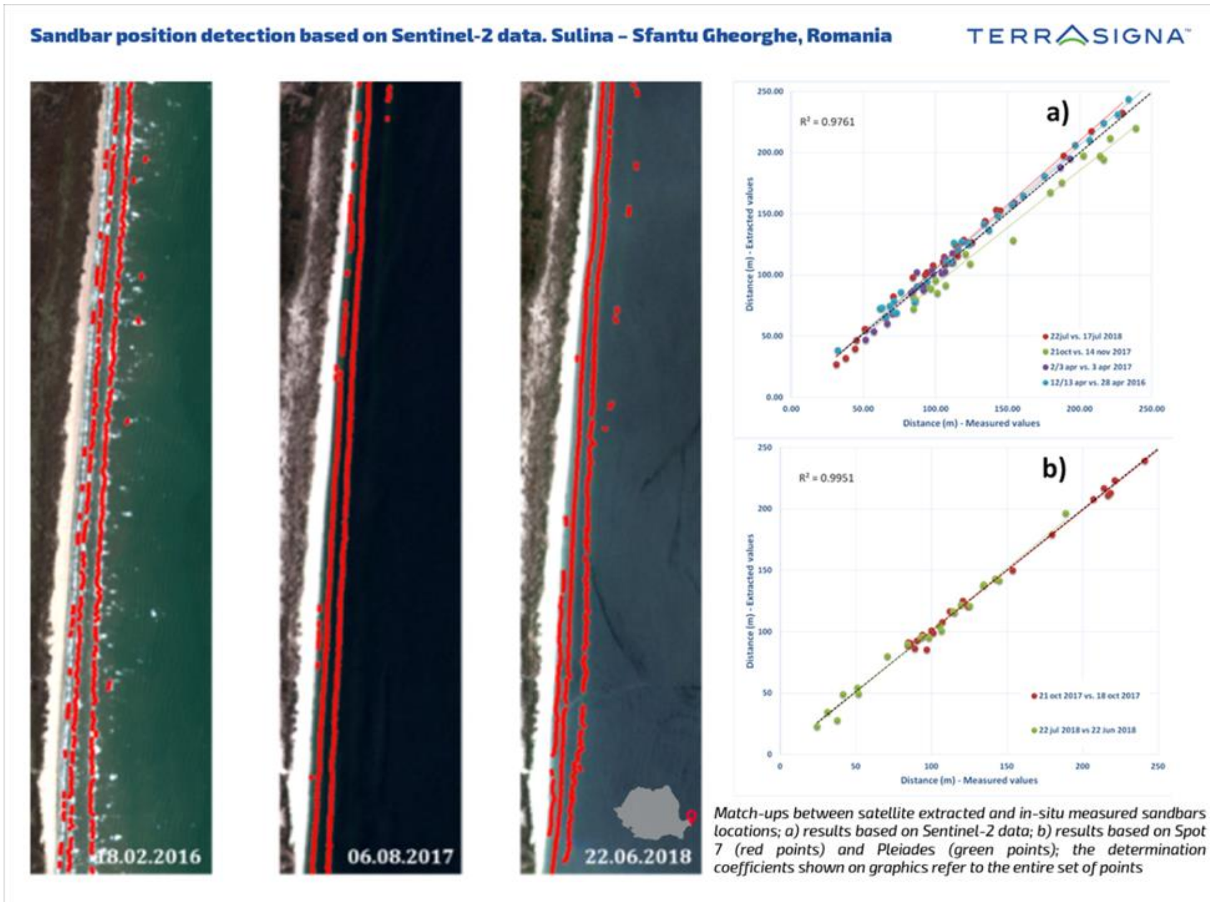

Fig. 37: Submerged sandbars position for Sulina – Sfantu Gheorghe area.

8.1.4 **Discussion**

The validation of the methodology used to derive submerged sandbars based on satellite data was performed using in-situ bathymetric measurements as reference information. The results show a satisfactory accuracy of the algorithm for Sentinel-2 and Landsat imagery (overall MAE of 7.25 m), with increased capabilities when high resolution data, such as SPOT 7 or Pleiades, is used (MAE of 3.35 m and 3.87).

8.2 Algorithm 6B – Mapping change of submerged sandbars/sand ridges

This algorithm to identify submerged sandbars or ridges in remote sensing images is based on the spatial analysis of the spectral reflectance values in an optical band. A submerged sandbar or ridge are characterized by local maxima in the reflectance value field. A ridge detector has been developed using the Hessian matrix (Mikolajczyk *et al.,* 2005). Yearly and seasonal averages have been generated from single acquisition sand ridges for the detection of stable and instable areas.

8.2.1 Data and study areas

Four study areas have been selected for retrieving submerged sandbars: Sylt Odde (North Sea), Kiel Probstei (Baltic Sea), Heiligenhafen (Baltic Sea) and Fehmarn (Baltic Sea). Only Sentinel-2 data are used for the extraction of submerged sandbars. The following products are processed and validated according to specification.

Area	Satellite name	Product date[1]	Validated in 2019	Validated in 2020	Not validated
Baltic Sea: Fehmarn (BFN)	Sentinel 2	2015		X	
Baltic Sea: Fehmarn (BFN)		2016		X[2]	
Baltic Sea: Fehmarn (BFN)		2017		X[2]	
Baltic Sea: Fehmarn (BFN)		2018		X[2]	
Baltic Sea: Fehmarn (BFN)		2019		X[2]	
Baltic Sea: Fehmarn (BFN)		2020		X[2]	
Baltic Sea: Heiligenhafen (BHH)	Sentinel 2	2015		X[2]	
Baltic Sea: Heiligenhafen (BHH)		2016		X[2]	
Baltic Sea: Heiligenhafen (BHH)		2017		X[2]	
Baltic Sea: Heiligenhafen (BHH)		2018		X[2]	
Baltic Sea: Heiligenhafen (BHH)		2019		X[2]	
Baltic Sea: Heiligenhafen (BHH)		2020		X[2]	
Baltic Sea: Kiel Probstei (BSP)	Sentinel 2	2015		X[2]	
Baltic Sea: Kiel Probstei (BSP)		2016		X	
Baltic Sea: Kiel Probstei (BSP)		2017		X[2]	
Baltic Sea: Kiel Probstei (BSP)		2018		X[2]	
Baltic Sea: Kiel Probstei (BSP)		2019		X[2]	
Baltic Sea: Kiel Probstei (BSP)		2020		X[2]	
North Sea: Sylt Odde (NSO)	Sentinel 2	2015		X[2]	
North Sea: Sylt Odde (NSO)		2016		X[2]	
North Sea: Sylt Odde (NSO)		2017		X[2]	
North Sea: Sylt Odde (NSO)		2018		X[2]	
North Sea: Sylt Odde (NSO)		2019		X[2]	
North Sea: Sylt Odde (NSO)		2020		X[2]	

[1] *all suitable products in the respective year*

[2] *Consistency tests between single acquisitions and quality control of sand ridges compared to input product*

The results were compared against airborne laser scan data, provided by LKN Schleswig-Holstein.

8.2.2 Method of validation

For validation of the extracted sand ridges from satellite, visual comparisons have been performed with bathymetry patterns from airborne laser scan data. The sand ridges are overlayed to the laser scan bathymetry data. In a first step, a daily sand ridge product is overlayed to the laser scan data (closest date), in a second step, the average of a period (seasonal or yearly) is overlaid. No quantitative validation has been performed for submerged sandbars.

8.2.3 Results

The results of different areas are shown by overlays of bathymetry maps and submerged sandbars. The first example is shown for Heiligenhafen Graswarder, which is south of Island of Fehmarn (rectangle in Fig. 38).

Fig. 38: RGB image Sentinel-2 (06.08.2015) showing Island of Fehmarn (Baltic Sea) and Heiligenhafen Graswarder south of the Island.

Fig. 39 shows the results from the submerged sandbar validation for the area Heiligenhafen Graswarder. It shows the bathymetry derived from laser scan data (left) and derived sand ridges of the submerged sandbars derived from Sentinel-2 (brown overlay in the right map). The laser scan data were acquired from an airborne-based survey, while the sand ridge is derived from Sentinel acquisition form 06.08.2015. The derived sandbar ridges follow well the structures of the bathymetry map.

In a next step, the yearly average of sandbar ridges is calculated and compared to the bathymetry map. It is shown in Fig. 40. pink colored pixels show the occurrence of sandbar ridges; a value of 1 indicates that a sandbar ridge was identified in 100% of images in 2016. This shows a high consistency and stability of the sandbar ridges north of Heiligenhafen Graswarder.

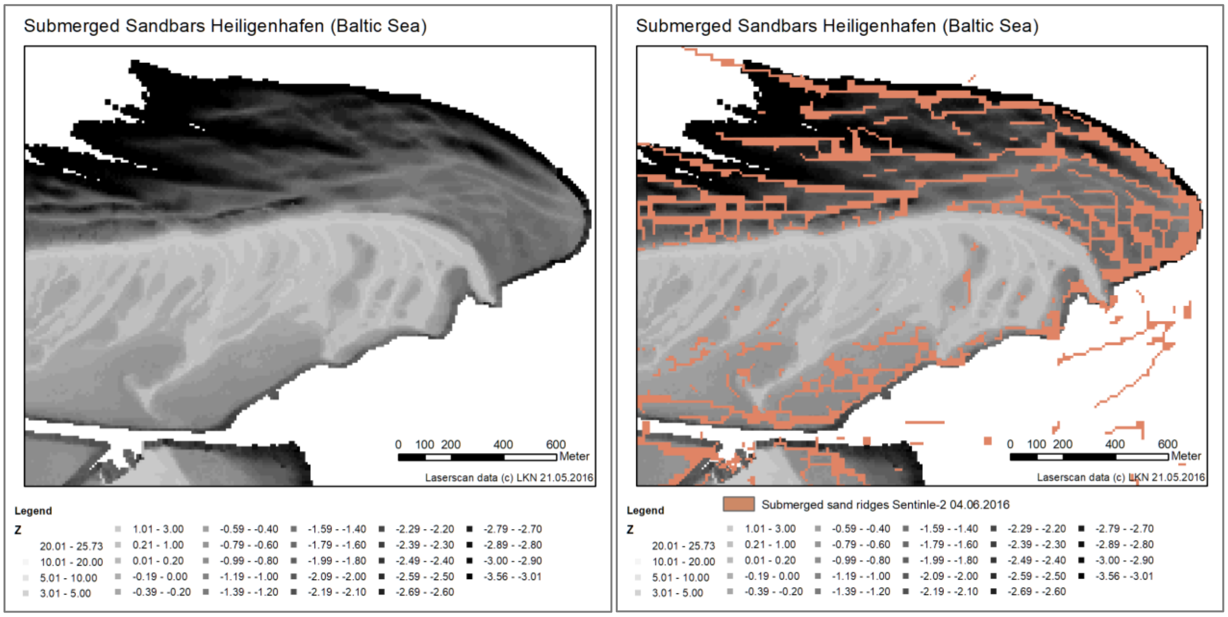

Fig. 39: Laserscan data showing land and submerged structures (left) overlayed with extracted submerged sandbar ridges from Sentinel-2 (right) for Heiligenhafen Graswarder.

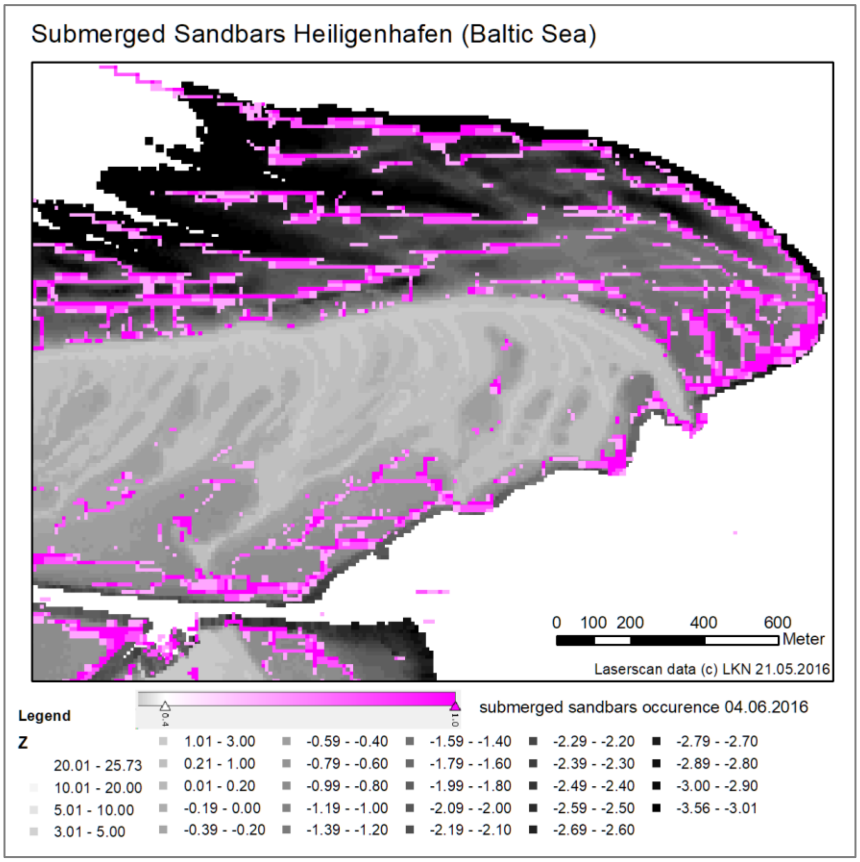

Fig. 40: Occurrence of submerged sandbar ridges in 2016 overlaying airborne laser scan bathymetry for Heiligenhafen Graswarder. Value of 1: sandbar ridge has been identified in all input images (Sentinel-2).

The same constellation of maps is shown for the area Fehmarn, and here at the northern coast (rectangle in Fig. 41).

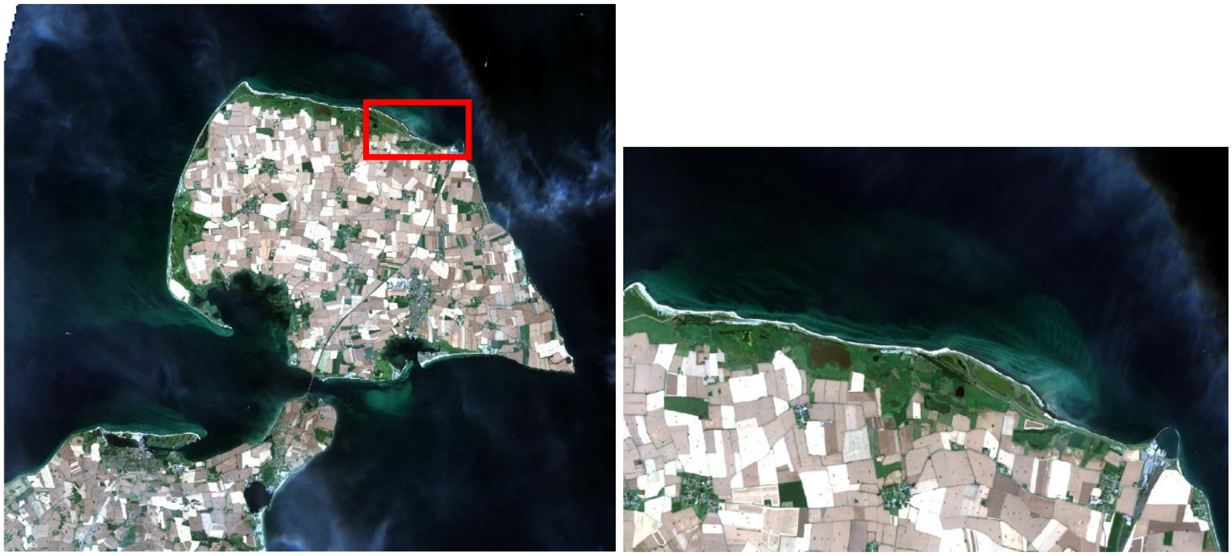

Fig. 41: RGB image Sentinel-2 (06.08.2015) showing Island Fehmarn in the Baltic Sea and subset Fehmarn North (right).

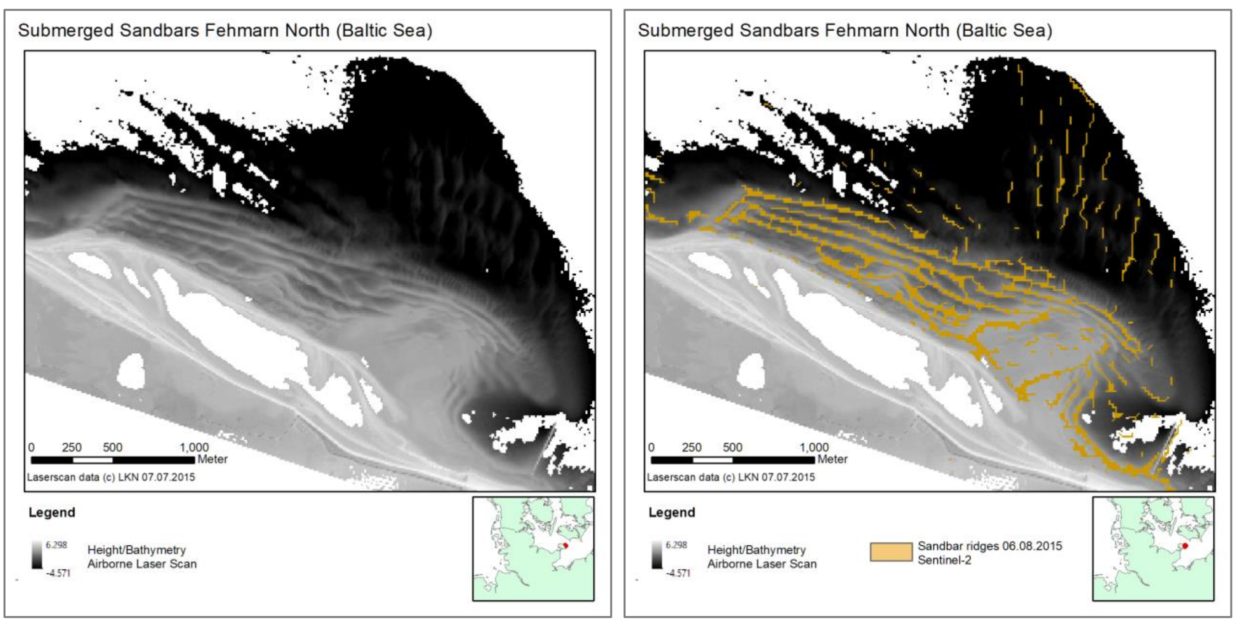

Fig. 42: Laserscan data (07.07.2015) showing land and submerged structures (left) overlayed with extracted submerged sandbar ridges from Sentinel-2 (06.08.2015, right) for Fehmarn North.

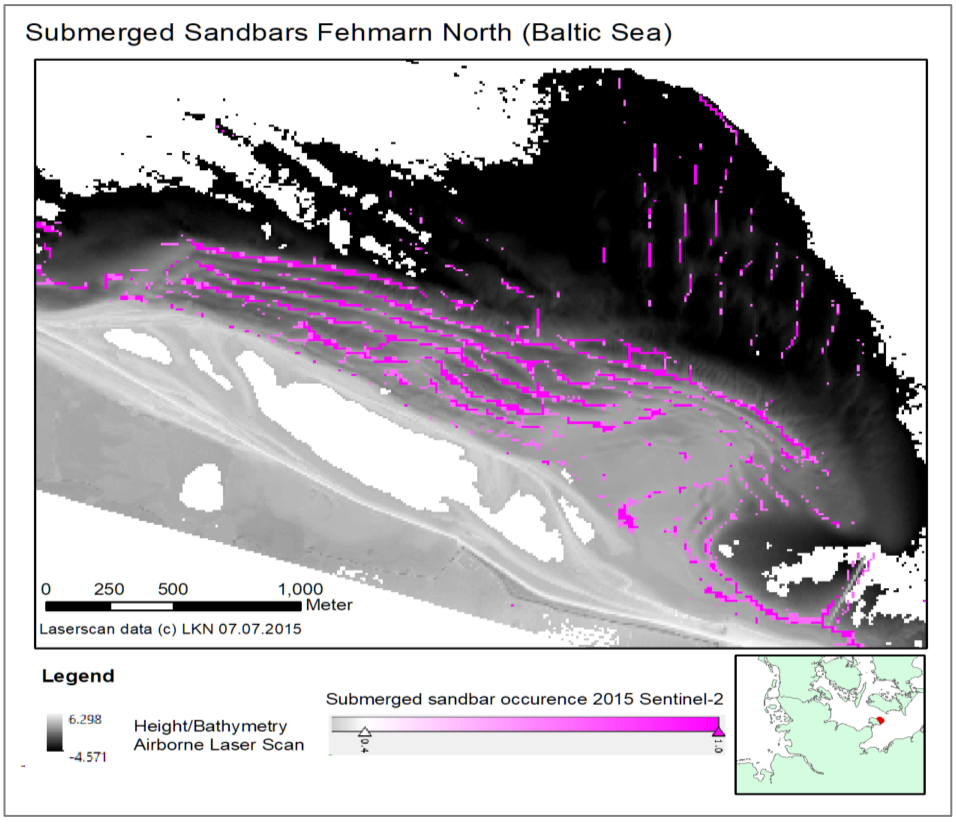

Fig. 43: Occurrence of submerged sandbar ridges in 2015 overlaying airborne laser scan bathymetry for Fehmarn (north). Value of 1: sandbar ridge has been identified in all input images (Sentinel-2).

The third area that was investigated is Kiel Probstei, a sandy beach with submerged sandbars close to the waterline.

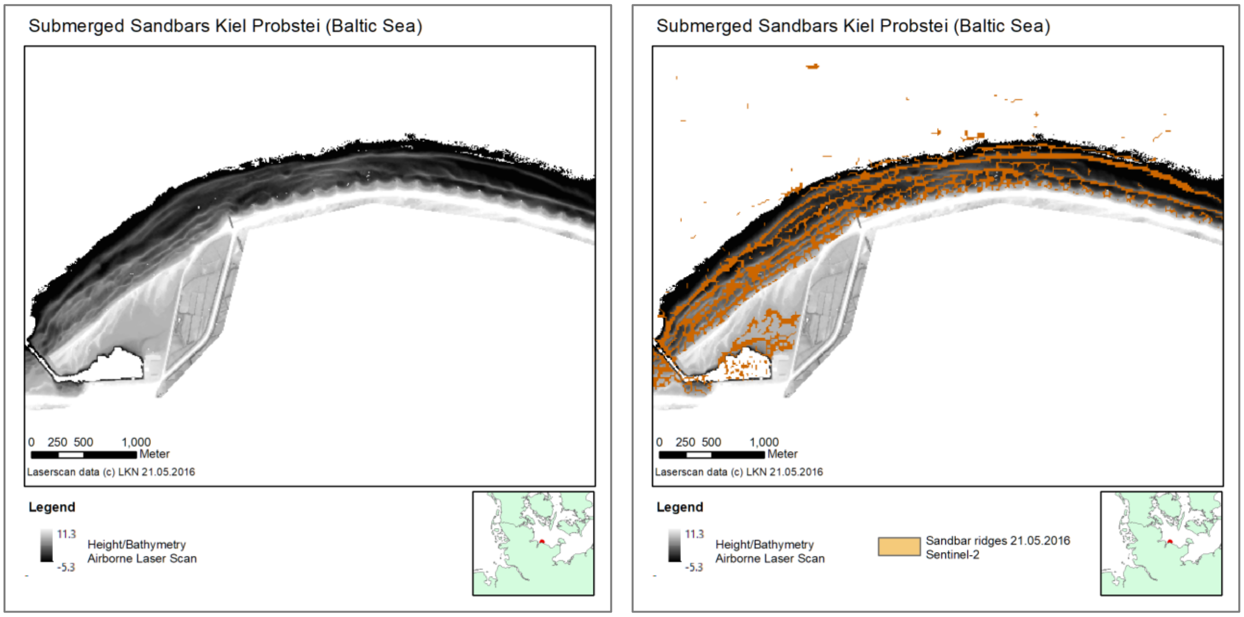

Fig. 44: Laserscan data (21.05.2016) showing land and submerged structures (left) overlayed with extracted submerged sandbar ridges from Sentinel-2 (21.05.2016, right) for Kiel Probstei.

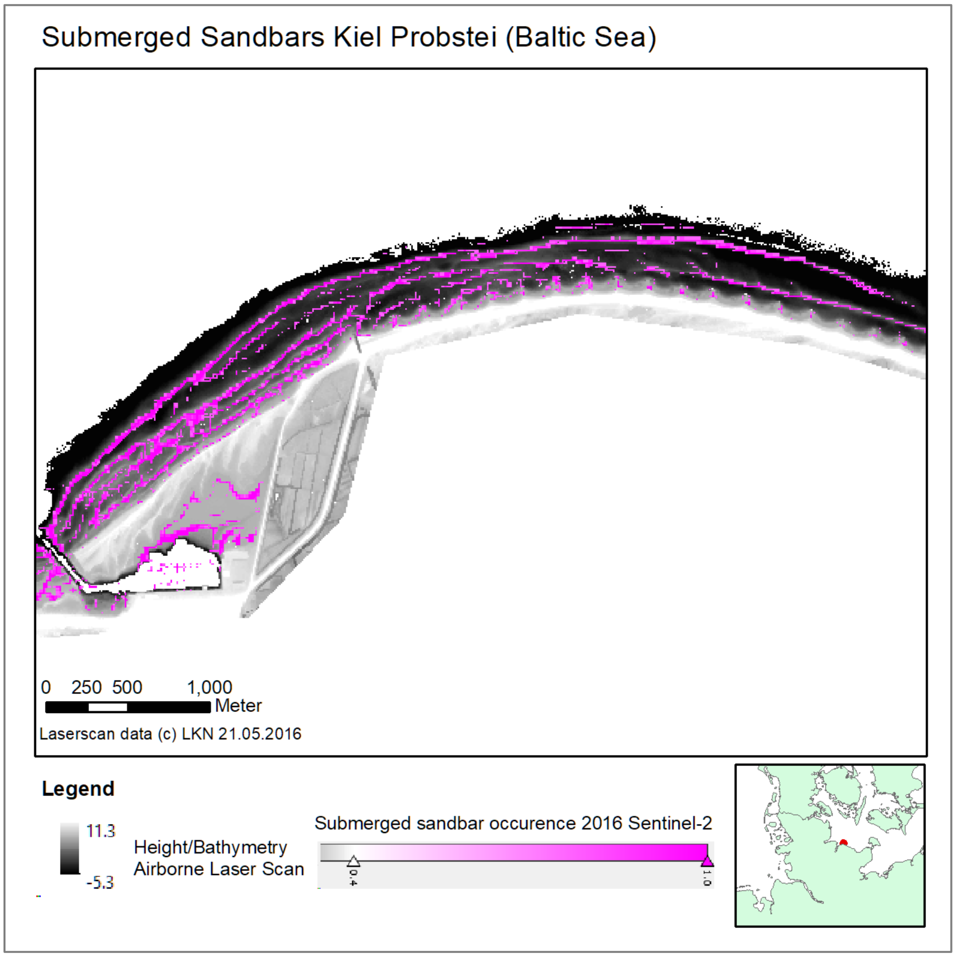

Fig. 45: Occurrence of submerged sandbar ridges in 2016 overlaying airborne laser scan bathymetry for Kiel Probstei. Value of 1: sandbar ridge has been identified in all input images (Sentinel-2).

For Sylt, no laser scan data were available for the areas which are further offshore. Therefore, visual assessment has only been performed by comparing the derived sandbar ridges with the input product (Fig. 45, Fig. 46).

Fig. 46: Submerged sandbars south of Island of Sylt - left: RGB showing submerged sandbars south of Island of Sylt, right: overlayed with derived submerged sandbar ridges from the same Sentinel-2 image (05.09.2018).

Problems with this method occur when other objects exist that show strong gradients. This is the case for cloud borders, cloud shadow, ships, waves, or sediment plumes. These influences are discussed in the following section.

8.2.4 Discussion

The detection of submerged sandbars works very well with Sentinel-2 data if the acquisitions fulfil the following requirements: the submerged sandbars need to be visible, thus the Secchi disk depth has to be larger than the depth of the water. Fig. 47 shows an example of an image with high sediment load which is not suitable to detect submerged sandbars.

Fig. 47: High sediment load in the coastal water is hindering the extraction of submerged sandbar ridges (example Fehmarn, Sentinel-2 from 21.04.2019).

The extraction of submerged sandbars is further influenced by clouds, cloud borders, thin clouds, or cloud shadows. They all show strong gradients which is interpreted as underwater structure by the algorithm. The same is true for waves and ships / ship wakes.

Fig. 48 shows an example of wrongly identified sandbar ridges caused by thin clouds and a ship.

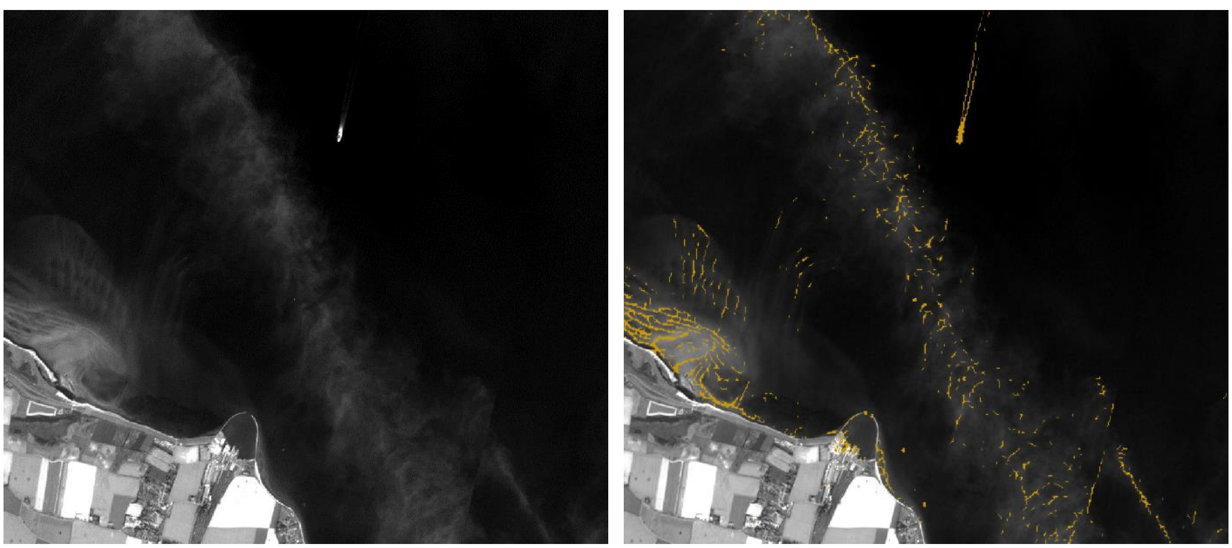

Fig. 48: Influence of clouds and ships on sandbar ridge detection - left: Sentinel-2 B3 showing thin clouds and a ship coming from North; right: due to strong gradients, clouds and ship are detected as sandbar ridges (orange overlay); area: Fehmarn North.

In the presented approach, we performed a pre-selection of suitable images by inspecting RGB images of all available Sentinel-2 images. Cloudy images and images with high sediment loads or very strong wave patterns have been erased from the data set. Furthermore, the averaging of all derived sandbar ridges for seasons and/or years erases temporary objects because they occur only in one of the images at the same position. This post-processing step enables us to detect stable and instable submerged structures, which is shown in Fig. 49. It shows an overlay of averaged sandbars 2016. Red areas indicate stable sandbars (occur in each image) while yellow sandbars might move and occur in only 50% of the cases.

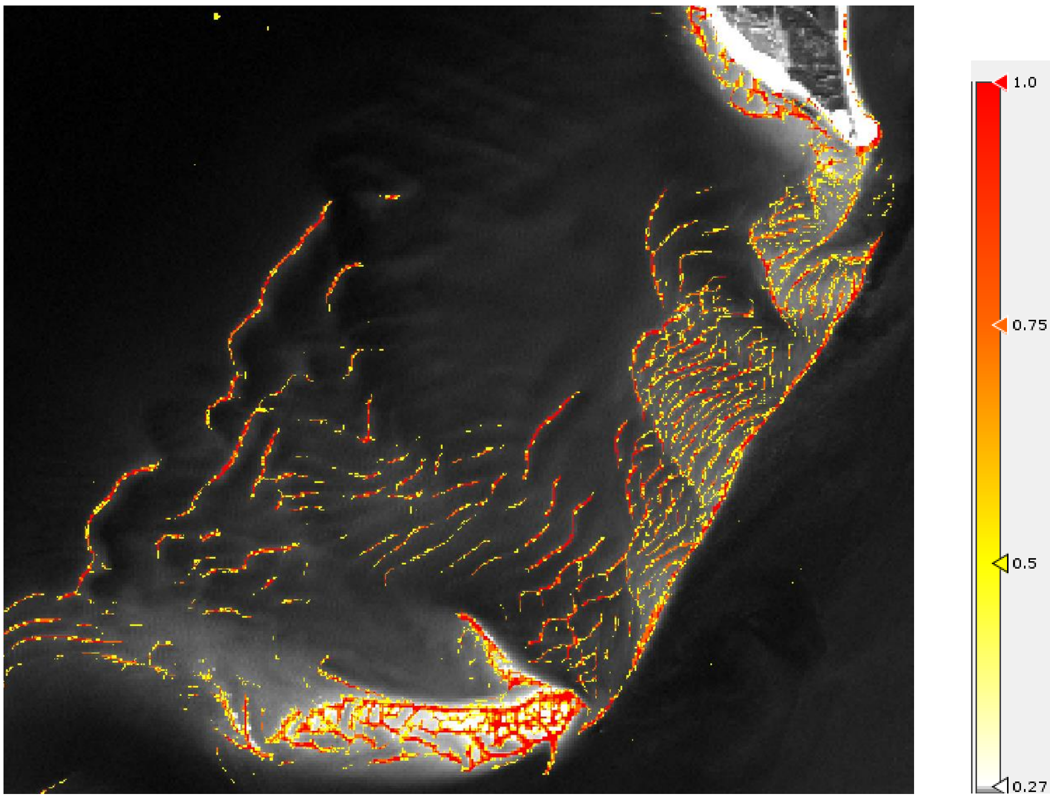

Fig. 49: Stability of submerged sandbars derived from occurrence maps (here: Sylt, 2016). Red areas indicate stable sandbars (occur in each image) while yellow sandbars might move and occur in only 50% of the cases.

The accuracy and clear detection of submerged sandbars was only possible with Sentinel-2 data, not with coarser resolution data such as Landsat. Therefore, products are only provided for 2015 – 2020.

9 VALIDATION OF INDICATOR ‘CREEK EDGE’

9.1 Algorithm 2J – Decision tree classification based on band ratios and LSU

9.1.1 Data and study areas

Landsat-7, Landsat-8 and Sentinel-2 data have been processed for the detection of intertidal creeks. For validation, in-situ measurements of creek positions were available for the Ossengot creek for 4 different years.

Area	Satellite name	Product date	Validated in 2019	Validated in 2020	Not validated	Validated 2*x
North Sea: Blauort	Sentinel 2	22.08.2015			X[1]	
North Sea: Blauort		05.09.2016			X[1]	
North Sea: Blauort		02.06.2017			X[1]	
North Sea: Blauort		10.09.2017			X[1]	
North Sea: Blauort		03.08.2018			X[1]	
North Sea: Blauort		22.09.2019		X		
North Sea: Blauort	Landsat-7	15.07.2002			X[1]	
North Sea: Blauort	Landsta-5	18.07.2006			X[1]	
North Sea: Blauort	Landsat-8	15.08.2013			X[1]	
North Sea: Blauort		21.08.2015		X		
North Sea: Blauort		08.09.2016		X		
North Sea: Blauort		29.08.2018		X		

[1] Validated against input product and plausibility check

9.1.2 Method of validation

Not many in-situ measurements are available for the validation of intertidal creek positions. A visual inspection is performed with in-situ measurements of creek position of the Ossengot creek. The outer tidal creek and tidal flat positions were checked visually against the original RGB images. As a third step, a comparison between creek positions derived from SAR and optical data is performed.

9.1.3 Results

Fig. 50 shows the results of the comparison between satellite derived creek positions (blue areas) and in-situ measurements (red lines) for the Ossengot creek for four different years. While 2015 – 2018 is derived from Landsat-8 images, the 2019 creeks are derived from Sentinlel-2 data. The positions agree very well, but the detection of the full creek is not possible with satellite data, especially with coarser resolution of Landsat data.

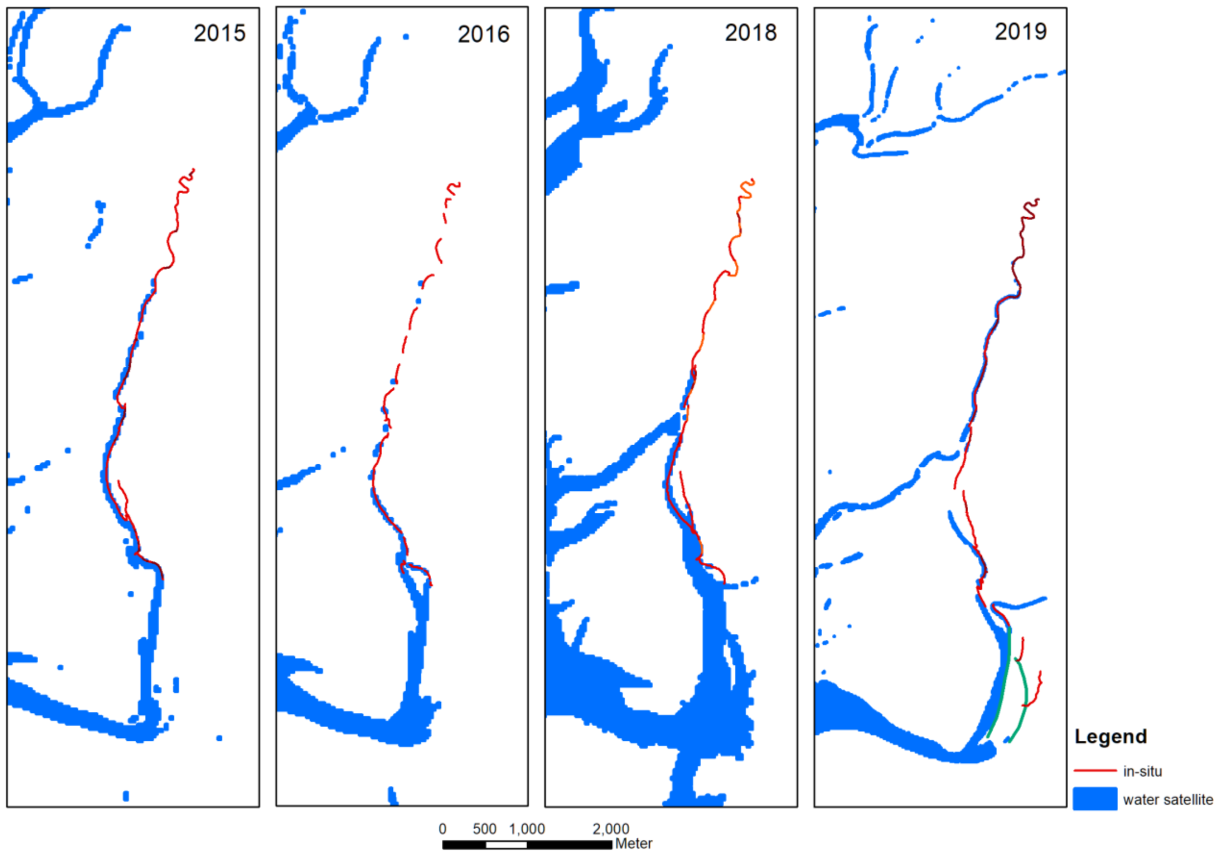

Fig. 50: Comparison of in-situ and satellite derived position of Ossengot creek from 2015 – 2019.

Consistency test has been performed with SAR derived tidal creek edges, the overlay of both techniques is shown in Fig. 51. The blue line shows the creek lines derived from Sentinel-2 (08.09.2016), the base images is a compilation of all SAR suitable acquisition in 2016.

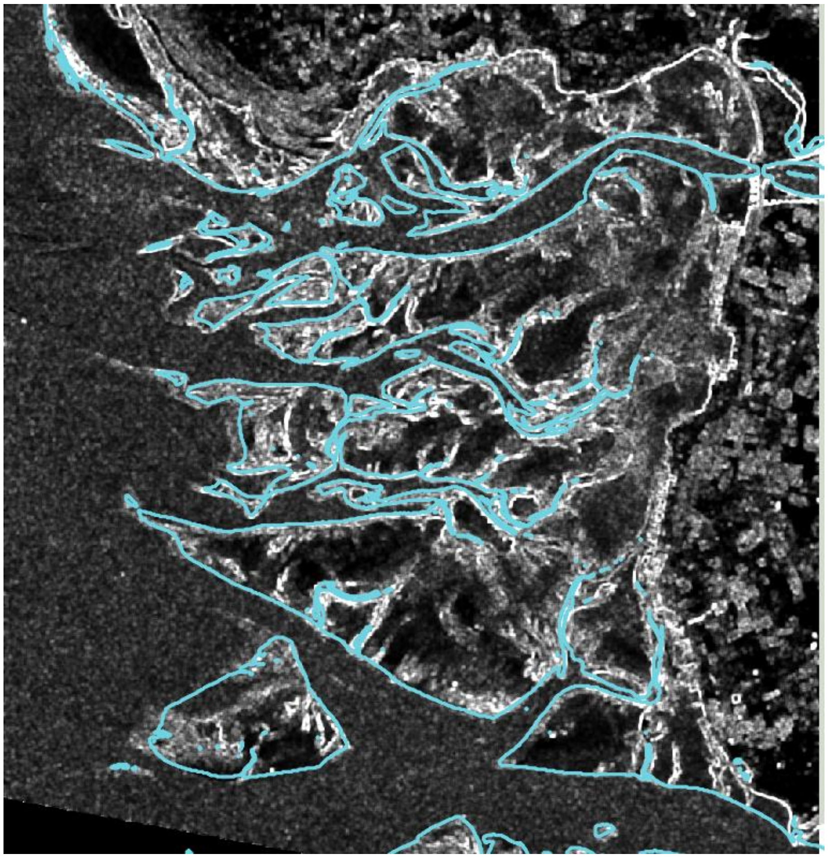

Fig. 51: SAR derived tidal flats (merged from products in 2016) overlayed with optically derived tidal flat edges (2016/09/08).

9.1.4 Discussion

Using optical data for tidal creek detection and their changes requires cloud free low tide acquisitions. A good comparison is only possible if the water level is similar between the images. The classification method based on band ratios is very well suited for larger creeks and the monitoring of creek changes and best results could be obtained with Sentinel-2 data due to the spatial resolution of 10m. Especially with Landsat, smaller creeks are not well detected, because the water signal is too much mixed with sediment in 30m resolution.

As the classification method itself has drawbacks for smaller creeks, we also investigated the possibility to use gradients for edge detection. This enables us to detect changes in reflectance (strong gradients), though the creeks themselves are not detectable. This approach will be further investigated (Fig. 52, Fig. 53).

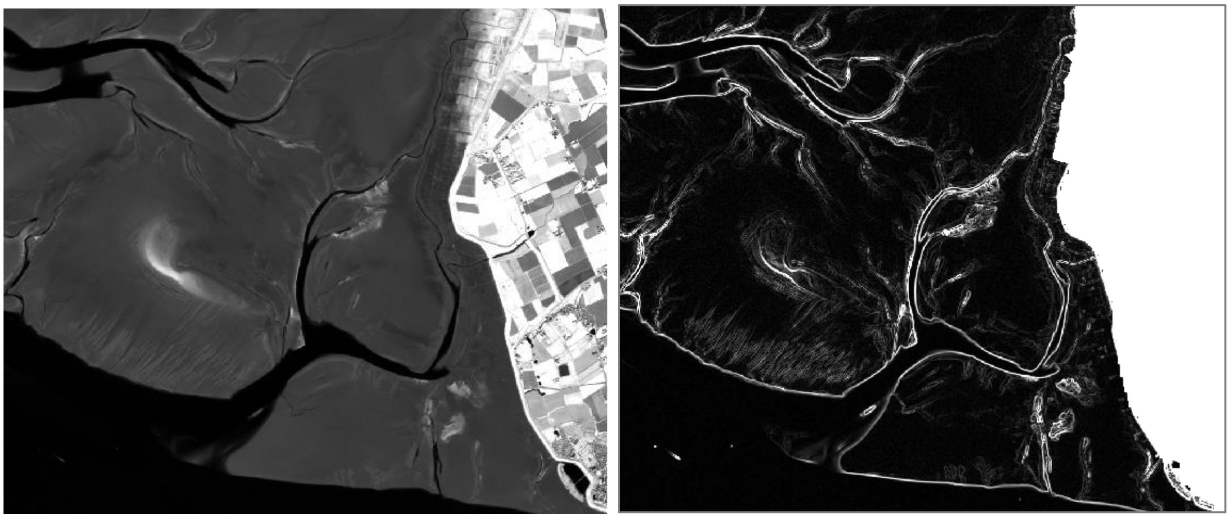

Fig. 52: Intertidal flat area Blauort in B8 (left) of Sentinel-2 and tidal creek edges derived from gradient of B8 (right).

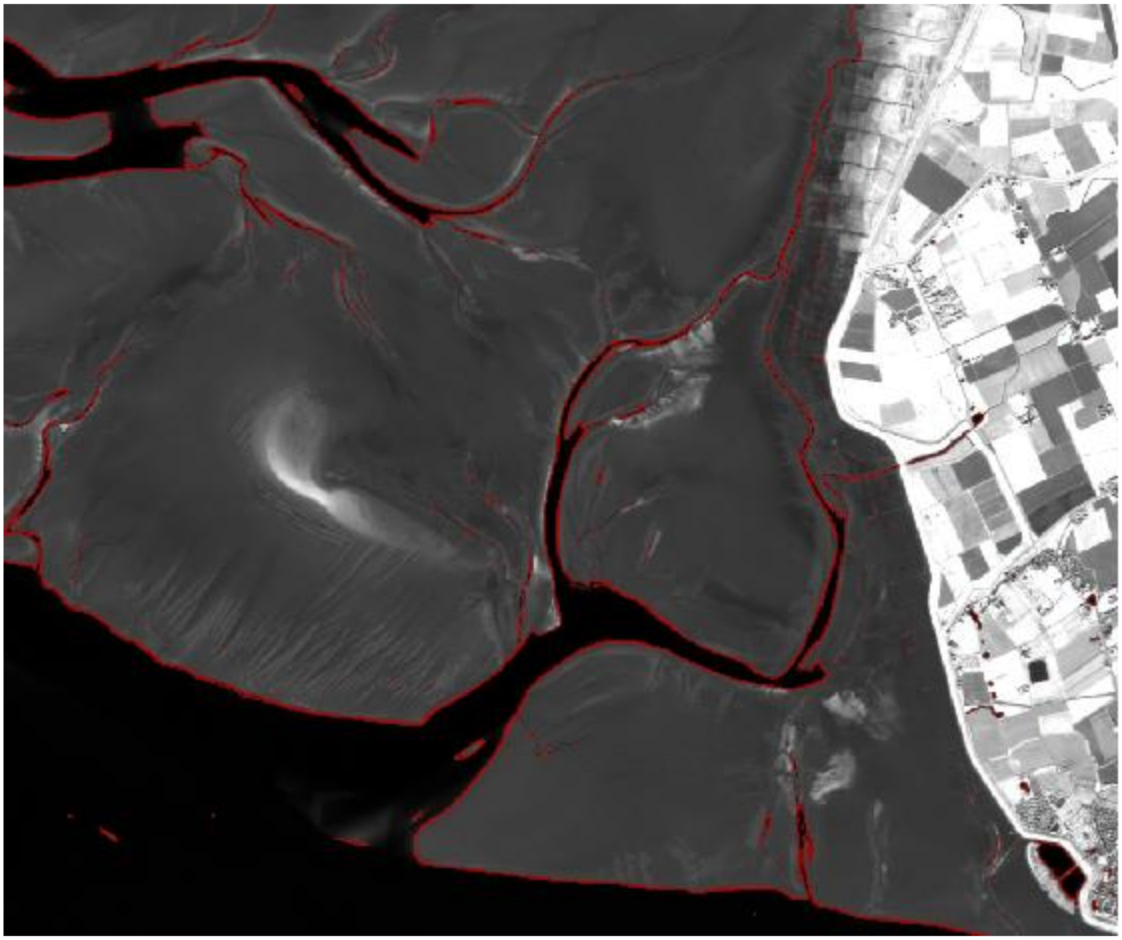

Fig. 53: Sentinel-2 B8 overlayed with tidal creek edges derived from gradient (red).

SYNTHESIS OF THE VALIDATION ACTION

	Bathymetry	Cliff lines	Dune foot	Submerged sandbars	Tidal flat / tidal creek morph.	Top of the cliff movement	Waterline and Upper swash limit (replace Middle of swash Zone)
FR - Fréjus-St Raphaël	Landsat-8, Sentinel-2, Pléiades						Sentinel-2, Landsat, Pléiades (2a2f)

FR - Camargue	Sentinel-2 (4b)						
FR - Corniche Basque		Sentinel-2, Pléiades, SPOT (3i)					
FR - Erretegia							
FR- Nord Médoc			Sentinel-2, SPOT (3h)				
FR - Vaches Noires		Sentinel-2, SPOT (3i)					
FR - Quiberville							
GE - Kiel Probstei				Sentinel-2			Sentinel-2, Landsat (2ai)
GE - NS Blauort					Sentinel-2, Landsat (2j)		
GE - NS Sylt Odde				Sentinel-2			Sentinel-2, SPOT, Landsat (2ai)
GE - Fehmarn				Sentinel-2			Sentinel-2, Landsat (2ai)
RO - Sulina-Sf. Gheorghe				Sentinel-2, Landsat, SPOT, Pléiades (6a)			Sentinel-2, SPOT, Pléiades, Landsat (2ai, 2aii, 2aiii), Sentinel-1, ERS (2g)
PT - Leiria		Sentinel-2					
PT - Aveiro	Sentinel-1 (4c)						
PT - Mondego	Sentinel-1 (4c)						
PT - Figueira Foz	Sentinel-1 (4c)						

CHANGES IN ALGORITHM NOMENCLATURE SINCE THE VALIDATION PLAN

Algorithm name and ID in the Validation plan		Algorithm name and ID in the Validation Report	
Water line detection using band rati os	2a	2AI	Waterline detection using band ratios
Waterline detection based on optical imagery	2b	2AII	Waterline detection using NDWI
		2AIII	Waterline detection using AWEI
		2AIV	Waterline detection using NDWI2
Middle of swash zone based on optical imagery	2b adapte d	2A2 F	Upper swash limit using combined NDWI-derived waterlines
Middle of swash zone based on SAR imagery	2d adapte d	-	
Waterline detection based on SAR imagery	2d	2G	Waterline detection using binary products from SAR amplitude data (Phase 1)
Dune foot based on textural analysis of VHR optical data	3a	-	
Dune foot extraction based on VHR imagery-derived DEM	1a - 3b	-	
Cliff lines extraction based on VHR imagery-derived DEM	1a - 3c	3c	Cliff line extraction using the cross-shore variation of the beach/cliff slope
Cliff lines extraction based on VHR/HR imagery-derived DEM	1b - 3c	-	
Cliff lines extraction - Manual linear feature extraction from DEMs	3d	-	
Beach width	3e	-	
Top-of-the cliff vertical movements	3f	3J	Top of the cliff movement monitoring using PS
Intertidal creek morphological characteristics	2e - 3g - 5c	2J	Decision tree classification based on band ratios and LSU

Dune foot extraction using supervised classification	3h	3H	Dune foot extraction using supervised classification
Cliff line extraction using supervised classification	3i	3I	Cliff extraction using supervised classification
Detection based on optical data	4b	4B	Quasi-analytical model to retrieve bathymetry from HR/VHR optical data
Detection based on SAR data	4c	4C	Bathymetry swell inversion
Submerged sand banks	6a	6A	Submerged sand banks
Mapping change of sandbars	6b	6B	Mapping change of submerged sandbars/sand ridges
Dune foot extraction using SAR data	3j	-	
Maximum swash zone excursion	run-up	-	

REFERENCES

Abreu, T., Fernández-Fernández, S., Baptista, P., Silva. P.A. 2019. Capítulo 37 - Utilização de wavelets para inferir a batimetria a partir de imagens de satélite SAR. Saindo da zona de conforto: a interdisciplinaridade das zonas costeiras. Ana Cristina Roque [et.al.]. Rio de Janeiro: FGEL-UERJ, pp.537-547. ISBN: 978-85-87245-03-8

Crosetto, M., Montserrat, O., Cuevas-Gonzalez, M., Devanthery, N., Crippa, B. 2011. Persistent Scatterer Interferometry: A review. ISPRS Journal of Photogrammetry and Remote Sensing Volume 115, May 2016, Pages 78-89. https://doi.org/10.1016/j.isprsjprs.2015.10.011.

Frodella, W., Ciampalini, A., Gigli, G., Lombardi, L., Raspini, F., Nocentini, M., Scardigli, C., Casagli, N. 2016. Synergic use of satellite and ground based remote sensing methods for monitoring the San Leo rock cliff (northern Italy). Geomorphology, 264, pp. 80-94, https://doi.org/10.1016/j.geomorph.2016.04.008.

Mikolajczyk, K., Schmid, C. 2005. A performance evaluation of local descriptors. IEEE Transactions on Pattern Analysis and Machine Intelligence 27(10):1615–1630. DOI: 10.1109/TPAMI.2005.188.

Neokosmidis, I., Avaritsiotis, N., Ventoura, Z., Varoutas, D. 2016. Assessment of the gap and (non-)Internet users evolution based on population biology dynamics. Telecommunications Policy Volume 39, Issue 1, February 2015, Pages 14-37. https://doi.org/10.1016/j.telpol.2014.10.006.

Otsu, N. 1979. A Treshold Selection Method from Gray-Level Histograms. IEEE Transactions on Systems, Man, and Cybernetics Vol. SMC-9, No. 1, https://doi.org/10.1109/TSMC.1979.4310076.

Pereira, P., Baptista, P., Cunha, T., Silva, P.A., Romão, S., Lafon, V., 2019. Estimation of the nearshore bathymetry from high temporal resolution Sentinel-1A C-band SAR data – A case study. Remote Sensing of Environment, 223, 199-178. doi: 10.1016/j.rse.2019.01.003.

Tatui, F., Constantin, S. 2020. Nearshore sandbars crest position dynamics analysed based on Earth Observation data. Remote Sensing of Environment Volume 237, February 2020, 111555. https://doi.org/10.1016/j.rse.2019.111555.

Vos K., Splinter K.D., Harley M.D., Simmons J.A., Turner I.L., 2019. CoastSat: a Google Earth Engine-enabled Python toolkit to extract shorelines from publicly available satellite imagery. Environmental Modelling and Software. 122, 104528